

Behaviour and Design of Unstiffened Wide-Flange Members Subjected to Torsional  
Moment through One Flange

by

Muhammad Ahmad

A thesis submitted in partial fulfillment of the requirements for the degree of

Master of Science  
in  
Structural Engineering

Department of Civil and Environmental Engineering  
University of Alberta

© Muhammad Ahmad, 2016

**Abstract:**

Behaviour of the unstiffened wide flanged member is not characterized by the available literature or current design standards. Torsional moment applied on the one flange unstiffened member causes the member to undergo local distortions. Conventionally, to avoid these local distortions stiffeners are provided in the joint. However, these stiffeners may add unnecessary costs to the joint and elimination of these stiffeners will lead to more economical solution. Behaviour of the unstiffened member subjected to the torsional loading has been explored in this report. Parametric numerical analysis studies have been performed to distinguish the effect of cross sectional dimension on the response of the member. Nine full-scale laboratory tests were conducted to further the existing knowledge. The response of the member has been assessed under the combined axial load and torsional moment. Studies have been conducted to provide the basis to calculate the behaviour of the unstiffened member for design.

## **Acknowledgements:**

Continuous support and efforts made towards the completion of this project by my supervisor, Dr. Robert Driver, are greatly appreciated. His comments were always positive and helpful.

Technical input provided by the Bo Dowswell and Logan Callele is also acknowledged. Special thanks go to Logan Callele of Waiward Steel Fabricators for providing the test specimens for this research project. I am thankful to Pouya Salem and Amir Jamshidi for their assistance in the numerical analysis.

I am grateful for the help provided by my father, Chaudhry Muhammad Akram, and my mother, Safia Bibi.

Financial support for this research project was provided by the Natural Sciences and Engineering Research Council through Dr. Driver.

## **Table of Contents**

1.	Introduction .....	1
1.1.	Background and need for the research.....	1
1.2.	Objectives and scope .....	3
1.3.	Thesis anatomy.....	8
2.	Literature Review .....	9
2.1.	Milner and Rao (1977-78).....	9
2.2.	Yura (2001).....	12
2.3.	Dowswell (2003).....	13
2.4.	Kristensen (2010).....	14
2.5.	Torsion of the flange .....	15
2.6.	Elastic torsional theory .....	16
3.	Numerical Analysis .....	18
3.1.	Whole cross-section torsion.....	18
3.1.1.	Shell element model .....	18
3.1.2.	Solid element model .....	19
3.1.3.	Results for torsion on entire cross-section .....	22
3.2.	Numerical analysis with stiffeners.....	26
3.2.1.	Full member and joint assembly.....	26
3.2.2.	Results for torsion with stiffeners.....	30
3.3.	Torsion without stiffeners.....	31
3.3.1.	Effect of depth of stiffener.....	32
3.3.2.	Simplified loading .....	34
3.3.3.	Boundary conditions effect.....	36
3.3.4.	Mesh refinement.....	37
3.3.5.	Parametric study .....	38
3.4.	Numerical analysis of selected W-sections.....	43
3.4.1.	Strength and stiffness .....	43
3.4.2.	Parametric comparisons.....	45
4.	Experimental Program.....	48
4.1.	Test matrix .....	48
4.2.	Test setup .....	51
4.3.	Test Specimens.....	54
4.4.	Instrumentation.....	57
4.5.	Ancillary tests.....	60

4.6.	Test results .....	62
4.7.	Numerical analysis comparisons .....	69
5.	Moment and Stiffness Prediction.....	76
5.1.	Maximum elastic moment capacity .....	76
5.2.	Stiffness prediction comparisons .....	80
5.3.	Axial load effect.....	88
5.4.	Combined axial load effect prediction.....	93
6.	Summary and Recommendations .....	97
6.1.	Summary .....	97
6.2.	Recommendations for further research.....	98
	References.....	99
	Appendix A.....	101
	Appendix B .....	113

### **List of Tables**

Table 4.1.	Test matrix .....	50
Table 4.2.	Coupon test results .....	62
Table 4.3.	Initial yield moment comparison .....	75
Table 5.1.	Comparison of initial yield moment .....	79
Table 5.2.	Maximum flange rotations from test .....	79
Table 5.3.	Effect of member length on $K_w$ .....	82
Table 5.4.	Effect of warping restraint on $K_w$ .....	82
Table 5.5.	Axial load effect on parametric study models .....	90
Table B.1.	Coupon measured dimensions .....	119

## List of Figures

Figure 1.1. Common examples of structures with twisting of flange.....	2
Figure 1.2. Deformed shape under torsion for stiffened and unstiffened members .....	3
Figure 1.3. Structural details of reference structure .....	4
Figure 1.4. Common loadings on members.....	5
Figure 1.5. Deformed shape of frame under weak-axis moment (exaggerated) .....	6
Figure 1.6. Beam line diagram with typical connection classifications .....	7
Figure 2.1. Test setup assembly, elevation view (after Milner and Rao 1978).....	10
Figure 2.2. Web stiffness computation setup (Milner 1977).....	11
Figure 2.3. W-section member loaded on one flange (Yura 2001) .....	13
Figure 2.4. W-section member loaded on one flange (after Dowswell 2003).....	13
Figure 2.5. Model for determining the effective web width, $b_{eff}$ (Kristensen 2010).....	14
Figure 2.6. Elastic torsion of flange.....	15
Figure 2.7. Theoretical torsion problem .....	16
Figure 2.8. Warping restrained boundary conditions .....	17
Figure 2.9. Warping allowed boundary condition .....	17
Figure 3.1. Shell model loading.....	19
Figure 3.2. Solid model rigid plate and assembly .....	20
Figure 3.3. Solid model pressure couple loading .....	21
Figure 3.4. Rotation calculation .....	22
Figure 3.5. Torsion results of 2 m long member .....	23
Figure 3.6. Torsion results of 4 m long member .....	23
Figure 3.7. Torsion results of 8 m long member .....	24
Figure 3.8. Torsion results of 18 m long member .....	25
Figure 3.9. Modified cross-sectional dimensions .....	25
Figure 3.10. Modified cross-section torsion results (8 m long).....	26
Figure 3.11. Column part with attributed mesh.....	27
Figure 3.12. Beam part with corresponding mesh.....	27
Figure 3.13. End plate with corresponding mesh .....	28
Figure 3.14. Bolt part with assigned mesh .....	28
Figure 3.15. Stiffener with corresponding mesh .....	29
Figure 3.16. Entire assembly with mesh.....	30

Figure 3.17. Torsion with stiffeners .....	31
Figure 3.18. Schematic of torsion with stiffeners.....	31
Figure 3.19. Stiffened vs. unstiffened torsion .....	32
Figure 3.20. Stresses and deformed shapes of cross-section with various stiffener geometries.....	33
Figure 3.21. Effect of stiffener geometries on moment–rotation response .....	34
Figure 3.22. Simplified loading model.....	35
Figure 3.23. Notation used in parametric study.....	35
Figure 3.24. Full-assembly vs. simplified loading model results.....	36
Figure 3.25. Effect of warping boundary conditions on unstiffened member.....	37
Figure 3.26. Effect of number of elements through web thickness and integration technique.....	38
Figure 3.27. Parameters with combination values.....	39
Figure 3.28. Typical moment-rotation response.....	40
Figure 3.29. Stress plot for web surface at various moments.....	41
Figure 3.30. Stress plot for cross-section of web at various moments .....	41
Figure 3.31. Parameter comparisons .....	43
Figure 3.32. Maximum elastic moment predicted by numerical analysis .....	44
Figure 3.33. Elastic stiffness predicted by numerical analysis.....	44
Figure 3.34. Beam analogy for web bending.....	46
Figure 3.35. Parametric comparison with numerical analysis.....	47
Figure 4.1. Normalized ratio of flange-to-web stiffness.....	49
Figure 4.2. Nominal dimensions of tested sections .....	50
Figure 4.3. Schematic loading diagram .....	51
Figure 4.4. Test setup—3D view .....	52
Figure 4.5. Top view of test setup .....	53
Figure 4.6. Side view of test setup.....	54
Figure 4.7. Fabrication drawing of test specimen SP8.....	56
Figure 4.8. Diagram showing the breakdown of forces.....	57
Figure 4.9. Primary instrumentation to measure displacements and rotations.....	58
Figure 4.10. Instrumentation profile.....	59
Figure 4.11. Test specimen in place with instrumentation before the test .....	60
Figure 4.12. Tension coupon cut-out locations .....	61

Figure 4.13. Test result SP1-W360×162 .....	63
Figure 4.14. Test result SP2-W310×86 .....	64
Figure 4.15. Test result SP3-W410×100 .....	64
Figure 4.16. Test result SP4-W250×80 .....	65
Figure 4.17. Test result SP5-W360×72 .....	65
Figure 4.18. Test result SP6-W310×67 .....	66
Figure 4.19. Test result SP7-W410×67 .....	66
Figure 4.20. Test result SP8-W310×129 .....	67
Figure 4.21. Test result SP9-W310×129 .....	67
Figure 4.22. Post-test gap between end plate and strong column (SP9) .....	68
Figure 4.23. Test result SP1-W360×162 compared with numerical results.....	70
Figure 4.24. Test result SP2-W310×86 compared with numerical results.....	71
Figure 4.25. Test result SP3-W410×100 compared with numerical results.....	71
Figure 4.26. Test result SP4-W250×80 compared with numerical results.....	72
Figure 4.27. Test result SP5-W360×72 compared with numerical results.....	72
Figure 4.28. Test result SP6-W310×67 compared with numerical results.....	73
Figure 4.29. Test result SP7-W410×67 compared with numerical results.....	73
Figure 4.30. Test result SP8-W310×129 compared with numerical results.....	74
Figure 4.31. Test result SP9-W310×129 compared with numerical results.....	74
Figure 5.1. Effective width of web for bending .....	77
Figure 5.2. Effective width of web for bending .....	78
Figure 5.3 Distortional stiffness ( $K_w$ ) comparison with numerical analysis results .....	83
Figure 5.4. Test vs. predicted results SP1.....	84
Figure 5.5. Test vs. predicted results SP2.....	84
Figure 5.6. Test vs. predicted results SP3.....	85
Figure 5.7. Test vs. predicted results SP4.....	85
Figure 5.8. Test vs. predicted results SP5.....	86
Figure 5.9. Test vs. predicted results SP6.....	86
Figure 5.10. Test vs. predicted results SP7.....	87
Figure 5.11. Test vs. predicted results SP8.....	87
Figure 5.12. Stresses due to axial load and bending effect.....	91
Figure 5.13. Illustration of interaction of stresses according to von Mises equation .....	93
Figure 5.14. Interaction comparison.....	94

Figure 5.15. Error in the predicted capacity with axial load .....	95
Figure 5.16. Moment rotation response under different axial loads.....	96
Figure A.1. Drawing material cut-outs .....	102
Figure A.2. Drawing SP1 .....	103
Figure A.3. Drawing SP2 .....	104
Figure A.4. Drawing SP3 .....	105
Figure A.5. Drawing SP4 .....	106
Figure A.6. Drawing SP5 .....	107
Figure A.7. Drawing SP6 .....	108
Figure A.8. Drawing SP7 .....	109
Figure A.9. Drawing SP8 .....	110
Figure A.10. Drawing SP9 .....	111
Figure A.11. Drawing load transfer beam .....	112
Figure B.1. Coupon drawing SP1 and SP2.....	114
Figure B.2. Coupon drawing SP3 and SP4.....	115
Figure B.3. Coupon drawing SP5 and SP6.....	116
Figure B.4. Coupon drawing SP7 and SP8.....	117
Figure B.5. Coupon drawing SP9 and detailed coupon.....	118
Figure B.6. Stress-strain curves for SP1 coupons.....	120
Figure B.7. Stress-strain curves for SP2 coupons.....	120
Figure B.8. Stress-strain curves for SP3 coupons.....	121
Figure B.9. Stress-strain curves for SP4 coupons.....	121
Figure B.10. Stress-strain curves for SP5 coupons.....	122
Figure B.11. Stress-strain curves for SP6 coupons.....	122
Figure B.12. Stress-strain curves for SP7 coupons.....	123
Figure B.13. Stress-strain curves for SP8 coupons.....	123
Figure B.14. Stress-strain curves for SP9 coupons.....	124

## List of Symbols

$M$	:	Twisting moment
$\Theta$	:	Angle of rotation
$K$	:	Effective stiffness of bracing system
$K_j$	:	Stiffness of the joint
$K_b$	:	Bending stiffness of the bracing member
$K_w$	:	Lateral bending stiffness of web, Local web distortional stiffness
$C$	:	Parametric function expressed in terms of flange to web torsional stiffness
$r$	:	The stiffness ratio by Milner (1977)
$t$	:	Flange thickness
$b$	:	Flange width
$w$	:	Web thickness
$\beta$	:	Parameter analogous to $K_w$ by Yura (2001)
$W_e$	:	Effective width of the web for web stiffness calculation, Yura (2001)
$N$	:	Connection length
$W_{eff}$	:	Effective width of web for bending, Dowswell (2003)
$F_y$	:	Yield stress
$M_n$	:	Maximum elastic moment capacity of unstiffened member, Dowswell (2003)
$M_{tor.fc.op.Rd}$	:	Plastic torsional capacity of the column, Kristensen (2001)
$b_{eff}$	:	Effective width of web in bending
$\gamma_{M0}$	:	Resistance factor
$G$	:	Shear modulus of the steel
$J$	:	St. Venant torsional constant
$L$	:	Length of the member
$C_w$	:	Warping torsional constant
$\theta', \theta'''$	:	1 <sup>st</sup> and 3 <sup>rd</sup> order derivative of $\theta$ w.r.t length
$r_1$	:	Parametric ratio of flange to web torsional stiffness
$P$	:	Load
$L_b$	:	Length of loading beam
$M_y$	:	Initial yield moment
$M_p$	:	Plastic web capacity
$K_U$	:	Net rotational stiffness of flange in unstiffened member
$K_S$	:	Torsional stiffness of the member with the stiffeners
$A, A_g$	:	Cross sectional area

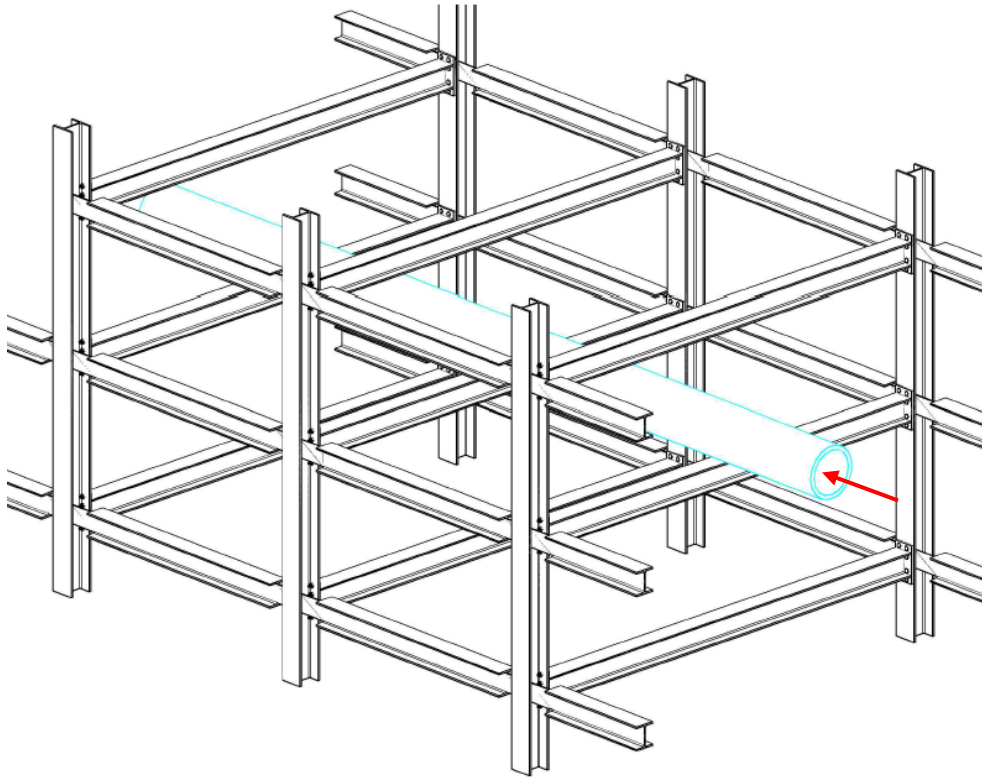
# **1. Introduction**

## **1.1. Background and need for the research**

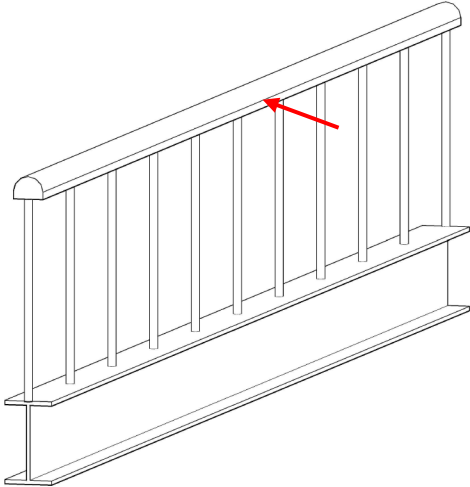
The need for both robustness and economy in the design of structures has led structural engineers to challenges where conventional design methods do not provide the optimal solution, and readily available literature fails to address the relevant issues directly. While wide-flange steel sections are generally selected where in-plane flexural loads predominate, in certain instances they are also called upon to resist torsional moments. The torsional moment often results from transverse loading of a member adjoining the flange of the wide-flange section, and is usually applied to one flange of the member only. Typically, stiffeners are added to engage the entire cross-section at the point of application of the torsional moment, making it twist uniformly and avoiding local deformations. However, the addition of stiffeners adds considerable cost to the joint, and in some structures this becomes a major cost of construction due to the additional cost of fabrication, labour, and delays, apart from the material cost.

Two examples of relevant instances where torsional moments can be significant are shown in Figure 1.1. Figure 1.1a is a modular pipe rack structure with end-plate moment connections between the transverse beams and supporting columns. Due to hydraulic loading in the pipe, weak-axis moment in the beam is transferred to the column as torsion. Another common case, depicted in Figure 1.1b, is guard/hand rails, where horizontal guard forces induce torsion in the beam top flange. In both cases, the cost of stiffeners can be a critical economic factor in the design. Another common example of torsional moment being transferred through a member flange is in the design of beam bracing where the bracing member is connected to the top flange of the beam to provide torsional restraint, potentially causing local distortion in the beam flange. In all of these example cases, a lack of available design guidelines can result in the cost of the fabricated joint increasing significantly.

Stiffeners welded into place between the member flanges and connected to the web tend to make the cross-section undergo uniform rotation when a torsional moment is applied, but unstiffened members may experience local deformations. This action is resisted in unstiffened members by a combination of flange torsion and bending of the web in the region adjacent to where the moment is applied. Distorted shapes of a stiffened and an unstiffened wide-flange section under torsional loading through one flange are shown in Figure 1.2.

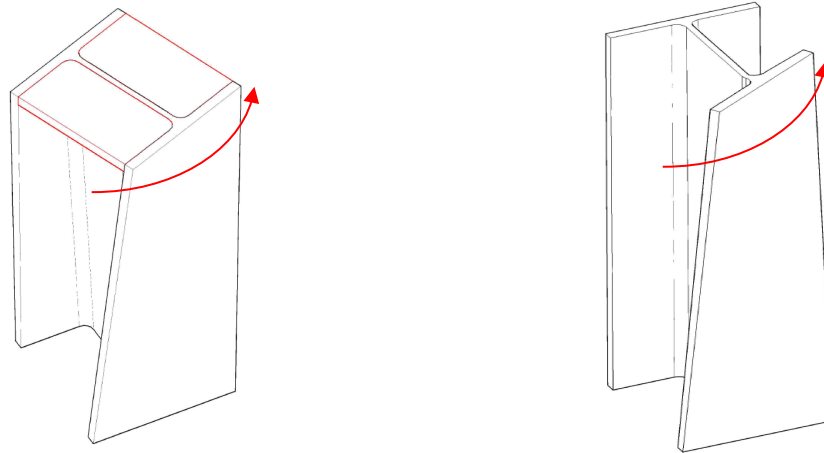


**a. Modular pipe rack**



**b. Guard rail**

**Figure 1.1. Common examples of structures with twisting of flange**



**a. Torsion with stiffeners**

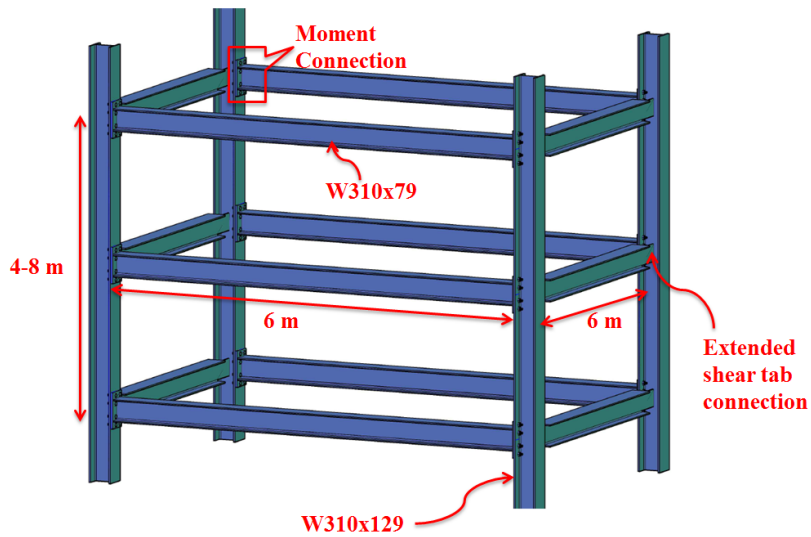
**b. Torsion without stiffeners**

**Figure 1.2. Deformed shape under torsion for stiffened and unstiffened members**

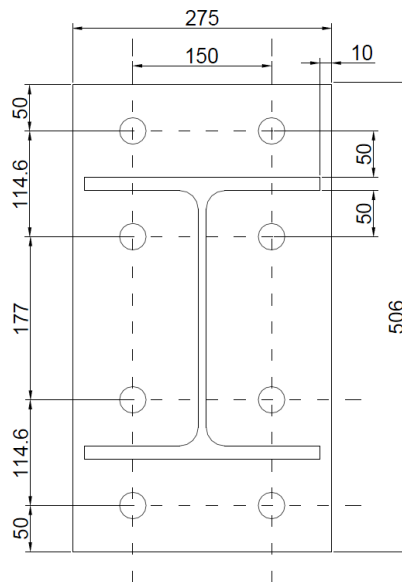
## **1.2. Objectives and scope**

The primary objective of this research is to investigate the behaviour of wide-flange members subjected to torsional moments applied through one flange. A major part of this objective is to identify when joints will function adequately under this type of loading without the need for stiffeners, in order to obtain the most economical design solution. To achieve this, the overall behaviour of unstiffened W-sections subjected to torsion is characterized, and important parameters that influence the stiffness and capacity of the member are identified and examined for the purpose of outlining a framework for the design of unstiffened members. This research includes a combination of numerical studies and full-scale laboratory tests on sub-assemblages modelled after an actual pipe rack structure.

The structure depicted in Figure 1.3a has been used as a reference example. The figure shows the representative dimensions of the modular pipe rack structure, which consists of W-section beams and columns. The beams connected to the column flanges are joined through end-plate moment connections for which the details are shown in Figure 1.3b. Out-of-plane lateral bracing of the columns at each level is provided by beams connected to the column web with coped ends or extended shear tabs. Weak-axis moment produced in the in-plane beams is transferred to the adjoining column flanges as torsion by the moment connection.



**a. Typical dimensions of structure (not to scale)**



**b. Moment connection dimensions (mm)**

**Figure 1.3. Structural details of reference structure**

Sections most commonly used for the fabrication of pipe rack structures of the type shown in Figure 1.3 tend to fall into a particular range of standard sizes. This study focused on that range, but these sections are frequently selected for other structures as well. The typical loadings to which the above structure could be subjected are shown in Figure 1.4.

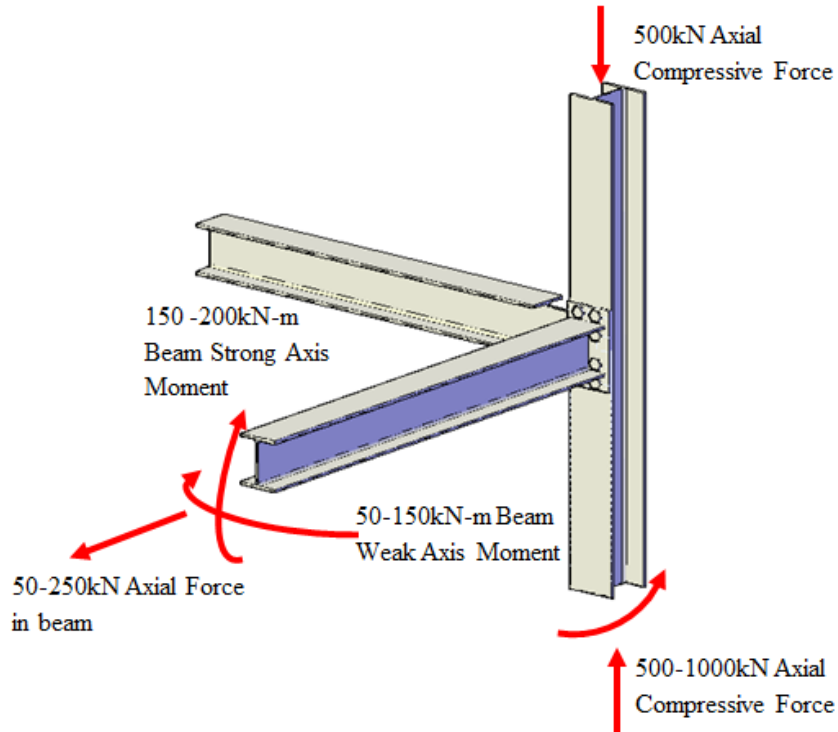


**Figure 1.4. Common loadings on members**

For many cases where in-plane (strong-axis) moment is applied to the column, stiffeners are not required. In such cases, the web provides enough bearing and shear resistance and the flange enough tensile resistance (without excessive local deformations) in response to the forces from each beam flange resulting from the moment. In these cases, the decision on the provision of column stiffeners comes down to the effect of the weak-axis moment from the beam transferred to the column as torsion.

Figure 1.5 shows the deformed shape of the beam resulting from weak-axis moment created by the out-of-plane applied load. Elastic curvature of the beam under the given loading causes the supporting columns to twist. Column sections with stiffeners undergo a certain rotation that can often be calculated and justified using classical elastic torsion theory. However, unstiffened columns undergo local deformations, and the rotation of the flange connected to the beam is greater

in comparison to the column with stiffeners. The additional rotation ( $\Theta$ ) changes the behaviour of the support (connection).

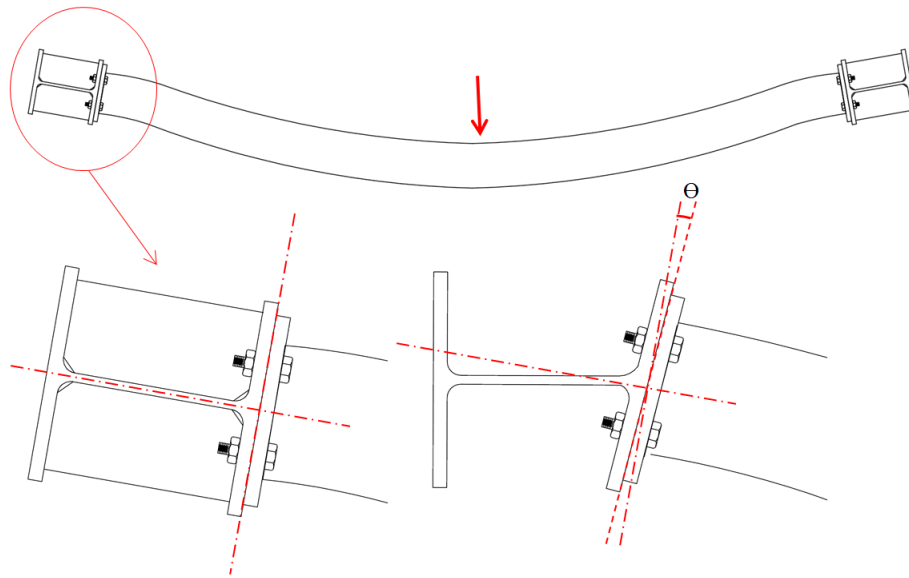


**Figure 1.5. Deformed shape of frame under weak-axis moment (exaggerated)**

Connection behaviour can be categorized into different classes. Figure 1.6 shows a typical beam line diagram, which classifies connections according to their rotational stiffnesses. This classification format is widely used in the design standards of North America and Europe. Three major types of connection are: rigid, semi-rigid and simple. If a connection loses less than 10% of its fully-fixed moment,  $M_f$ , due to rotational deformations, that connection can still be used as a moment connection and is considered rigid (or fully restrained). If a connection resists 90% to 20% of its fully-fixed moment, it is recognized as a semi-rigid (or partially restrained) moment connection. Connections that lose more than 80% of the fully-fixed moment due to support rotation are simple (or shear) connections.

For the beam weak-axis moment under consideration, the presence or absence of stiffeners in the supporting column can have a major impact on the overall support stiffness. Thus, classifying the unstiffened case necessitates the formulation of stiffness offered by a combination of column flange torsion and localized web bending. Where the stiffness of the member without stiffeners is known, it can be used in the primary analysis of the structure and the connection can be designed as a

moment connection, but the connection design moment would tend to be less than that in the stiffened case.

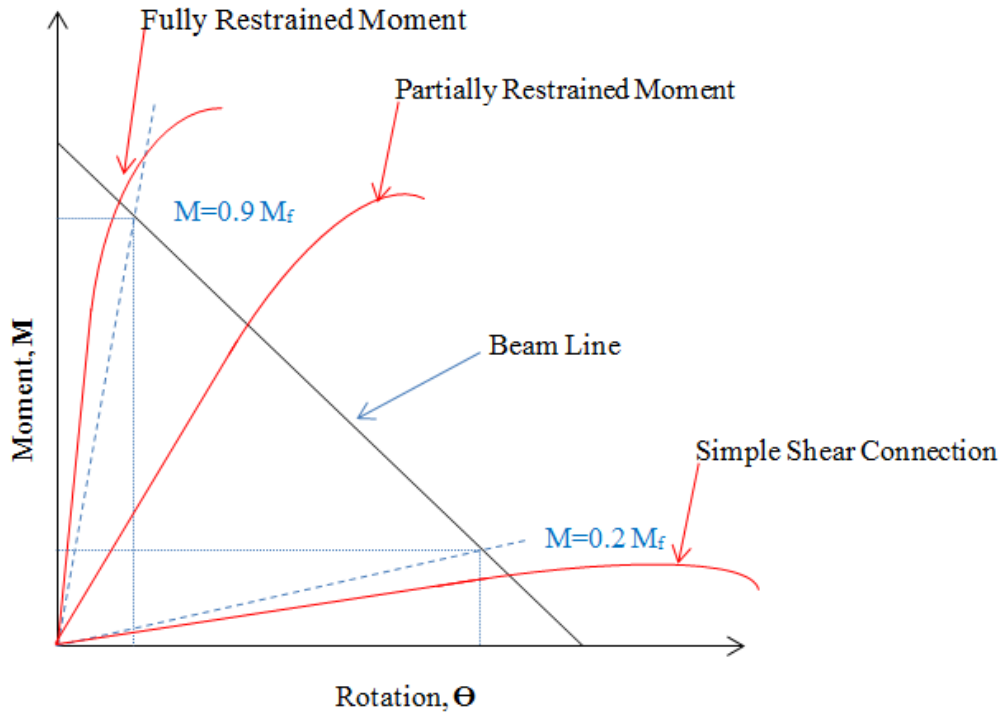


**Figure 1.6. Beam line diagram with typical connection classifications**

Apart from the lower local rotational stiffness of an unstiffened column, the total torque-carrying capacity is also lower. The web-flange junction in the connection region, which undergoes deformation when the flange is loaded torsionally, can limit the design moment. For elastic behaviour, yielding of the web becomes a limiting criterion instead of yielding of the flanges, which would occur first in the stiffened case. Maintaining stresses in the column web in the elastic domain serves to keep cross-sectional distortions small enough so as not to compromise the ability of the column to resist the axial design force determined using conventional procedures. While design standards generally do not explicitly define limits on cross-sectional distortion, since an important purpose of the column is to carry the axial loads the overall performance of a member providing a flexible beam support may be inadequate. Therefore, studies have also been performed on columns with combinations of loadings.

Summarising the above discussion, insight was needed to explain the behaviour of unstiffened W-sections loaded torsionally through one flange. For that purpose, a method to estimate the torsional capacity and stiffness of these members was investigated, and their interaction with axial loads was examined. Numerical analyses and tests were conducted to determine the torsional capacity and stiffness, whereas numerical analysis was performed to investigate the behaviour under combined loading.

### **1.3. Thesis anatomy**

This report is organized in six chapters. Chapter 2 summarizes relevant research and theory pertaining to the project. Chapter 3 discusses the numerical analysis procedures and results, including the numerical modelling of stiffened members and parametric studies of unstiffened members. Chapter 4 focuses on the testing program and provides outlines of the test matrix, test setup, instrumentation, and specimen geometric details, as well as the test results. Comparisons of the test results and formulations by numerical analysis are provided in Chapter 5, in addition to discussions of finite element analysis models incorporating axial load effects. Final conclusions are drawn and recommendations for the further study are given in Chapter 6. Numerical analysis moment–rotation graphs and test specimen drawings are provided in the appendix.

## **2. Literature Review**

Several empirical methods for the solution of the problem described in Section 1.1 can be found according to local practices by design engineers, but there is no single codified method supported by either physical tests or finite element analysis for the design of the unstiffened member. Particularly, for the torsional moment capacity of the member, very little is known. Some of the research that is related to the project is discussed in the following paragraphs. This research does not address the problem directly, but various conclusions can be used towards its solution.

### **2.1. Milner and Rao (1977-78)**

Due to common use in bracing systems, studies have been performed on the flexural behaviour of braces connected to a beam top flange and the resulting twisting response of the unstiffened flange. Early work traces back to Milner and Rao in the 1970s. This work was done to evaluate the rotational stiffness of the bracing system required, when the brace member is connected to the beam tension flange, for the brace to be considered fully effective. The scope is inclined more towards the design of bracing where the member to be braced has a tendency to twist due to lateral-torsional buckling. The research focused on beam bracing using purlin assemblies connected to the top flange to transfer vertical loads to these members. Lateral translational support is essentially provided to the beam by the axial stiffness of the braces, but torsional support also needs to be provided since the brace is connected to the tension flange. Torsion of the member is carried as bending moment by the bracing element, which has its own flexural stiffness. If the beam is unstiffened, this torque creates deformations in the beam web, decreasing the effectiveness of the torsional brace. Therefore, the total rigidity of the bracing system is the combination of beam-web, joint, and purlin stiffnesses. Correct estimation of all these parameters is important for determination of the total stiffness offered by the bracing system.

Milner and Rao (1978) conducted full-scale tests on assemblies of beams braced laterally by light-gauge lipped-channel purlins bolted to a vertical lap plate, in turn welded to the beam top flange. Figure 2.1 shows the test assembly. The boundary conditions for the beams were all “warping-allowed and twist-prevented” at the ends. The purpose of these tests was to study the overall bracing system stiffness required to permit the brace to be considered fully effective for evaluating the lateral-torsional buckling capacity of the beam.

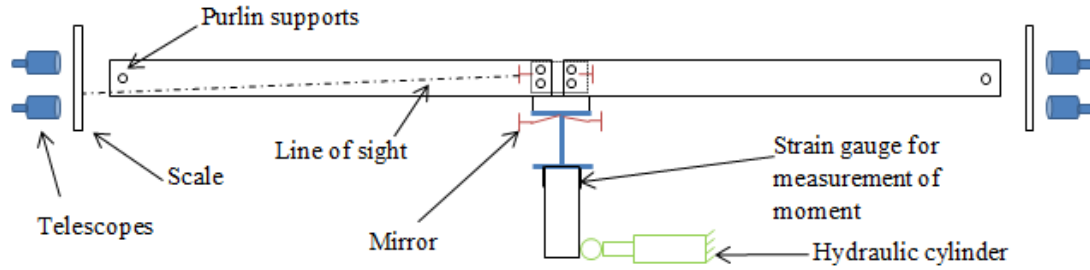


**Figure 2.1. Test setup assembly, elevation view (after Milner and Rao 1978)**

The effective stiffness of the bracing system,  $K$ , is given by:

$$\frac{1}{K} = \frac{1}{K_b} + \frac{1}{K_j} + \frac{1}{K_w} \quad [2-1]$$

where:

$K_b$  = bending stiffness of the bracing member

$K_j$  = stiffness of the connection (joint)

$K_w$  = lateral bending stiffness of the web

Milner and Rao (1977) used a combination of numerical finite strip analyses and tests to evaluate all the parameters in this study. Most relevant to the current research, they conducted detailed studies of the web distortion factor. The web bending distortional stiffness,  $K_w$ , was calculated as the difference of the stiffnesses by clamping both the flanges (stiffened) and unclamping the cross-section (unstiffened), with all other parameters unchanged. These tests were conducted at a laboratory scale of 1/10. The test setup used for determining the web stiffness is depicted in Figure 2.2.

The values from the tests were in close agreement with the finite strip method. Lateral movement of the beam was observed to be small due to the bracing connected to one flange only. The flange rotations observed were used to define the web bending stiffness as a function of an empirical parameter,  $C$ .

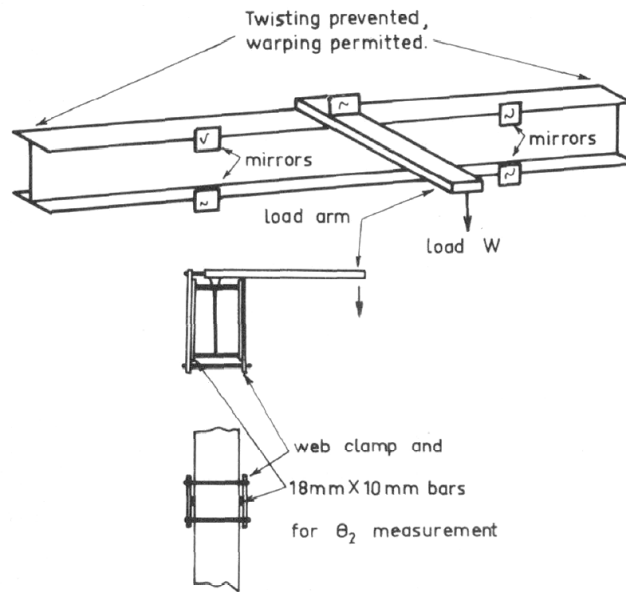


**Figure 2.2. Web stiffness computation setup (Milner 1977)**

The expression for  $K_w$  is as follows:

$$K_w = C E w^3 \quad [2-2]$$

where  $C$  is dependent principally upon the ratio of the web (flexural) to flange (torsional) stiffnesses, given as:

$$C = 1.30 - 1.60r + 0.80r^2 \quad [2-3]$$

The stiffness ratio,  $r$ , was defined as:

$$r = \frac{d w^3}{b t^3} \quad [2-4]$$

where:

$t$  = flange thickness

$b$  = flange width

$d$  = depth of member

$w$  = web thickness

Milner and Rao (1977) proposed that the stiffness ratio,  $r$ , will not change significantly from one section to another for typical standard sections, and  $C$  of 0.5 is conservative for their application in the design of bracing. However, the value saw a variation of 0.51 to 1.01 over the parameters considered.

Milner and Rao (1977) determined  $K_b$  through conventional elastic analysis and  $K_j$  through back-calculation using Equation [2-1]. One major difference compared to the problem described in Section 1.1 is that these purlin connections are not as rigid compared to moment connections in conventional frames, as the purlin connections have the tendency to undergo localised deformations and bolt slip.

## 2.2. Yura (2001)

Yura (2001) extended the previous work on the influence of brace stiffness on the lateral–torsional buckling capacity of a beam, and in particular on the component of the stiffness stemming from the beam’s cross-sectional distortional behaviour at the brace location. One important factor, the effect of the connection width along the member, was not considered by Milner and Rao (1978), most probably because in their tests the connection to the beam flange was made using a relatively thin vertical plate. However, this issue was addressed by Yura (2001) and the proposed guidelines for the design of the bracing became part of the *AISC Specification* (AISC 2010) in Appendix 6. The studies were based on results of the tests conducted by Milner and Rao (1978) and an independent numerical analysis study. Yura (2001) proposed an equation that also considers the presence of stiffeners, if any, as long as the stiffeners extends at least three quarters the beam depth and are connected to the flange to which the brace is attached. The effective width for the computation of the member stiffness was given as the width of the connection,  $N$ , plus 1.5 times the depth of the member between flange centroids, as indicated in Figure 2. 3.

The web stiffness,  $\beta$ , analogous to the parameter  $K_w$  of Milner and Rao (1977), using an effective width approach without stiffeners, is given as:

$$\beta = \frac{3.3 E}{h} \left[ W_e \left( \frac{w^3}{12} \right) \right] \quad [2-5]$$

where:

$$W_e = \text{effective width of the web} = N + 1.5 h$$

$E$  = modulus of elasticity

$h$  = distance between flange centroids =  $d - t$

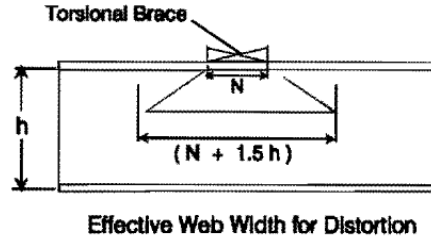


**Figure 2.3. W-section member loaded on one flange (Yura 2001)**

Comparison of Equations [2-2] and [2-5], and setting  $N = 0$  for consistency, implies that Yura (2001) obtained a value of  $C$  equivalent to 0.41, slightly lower than the design value recommended by Milner and Rao (1978) of 0.5.

### 2.3. Dowswell (2003)

Dowswell (2003) utilized Equation [2-5] and studied the parameter  $W_e$  further through a numerical investigation on parametric models and sections from the *AISC Steel Construction Manual* (AISC 2011). He observed the highly stressed region where the loading was applied, and due to localized stresses in the web an effective width (Figure 2. 4) was fitted for the plastic moment capacity of the web, as given in Equation 2-6. Equations [2-7] and [2-8] indicate that the plastic moment capacity of the web, based on the effective width, can be used to determine the web strength.

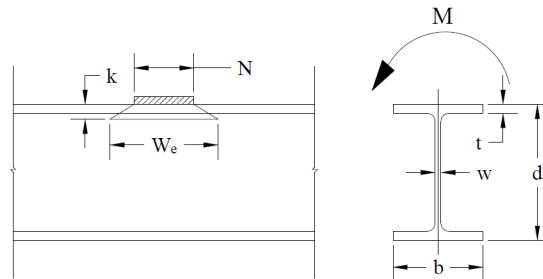


**Figure 2.4. W-section member loaded on one flange (after Dowswell 2003)**

$$W_{eff} = N + 1.8 \frac{t}{w} (\sqrt{bd}) \quad [2-6]$$

$$M_n = F_y \cdot Z_{eff} \quad [2-7]$$

$$Z_{eff} = W_{eff} \cdot \frac{w^2}{4} \quad [2-8]$$

## 2.4. Kristensen (2010)

Kristensen (2010) studied the design of endplate moment connections for beams subjected to out-of-plane (weak-axis) moment. Part of the work proposed an equation for the plastic capacity of the supporting section, which is subjected to a torque applied to one flange. The capacity consists of the summation of two times the plastic torsional capacity of the flange (accounting for the contribution of the sections on each side of the connection) and the plastic moment capacity of the web using an effective width, as follows:

$$M_{tor.fc.op.Rd} = \frac{\frac{f_y}{\sqrt{3}} b t^2 \left(1 - \frac{1}{3} \frac{t}{b}\right)}{\gamma_{M0}} + \frac{f_y w^2 b_{eff}}{4\gamma_{M0}} \quad [2-9]$$

where:

$M_{tor.fc.op.Rd}$  = plastic torsional capacity of the column (torque applied to one flange)

$b_{eff}$  = effective width of web in bending

$\gamma_{M0}$  = resistance factor

Figure 2.5. depicts a column flange with four holes for the bolts of the moment connection. Kristensen (2010) assumed that when a moment is applied to the flange, influence lines from the bolt holes towards the column web progress at an angle of the  $60^\circ$ , which increases the effective width of the bending of the web,  $b_{eff}$ , from just the distance between the holes ( $P_1$ ) by an additional amount of  $1.73 P_2$ , where  $P_2$  is the horizontal distance between the holes. Therefore, the effective width for bending was determined as  $b_{eff} = P_1 + 1.73 P_2$ . This method gives a means of estimating the plastic capacity of the section under torsion applied to one flange, although considerable deformation would need to take place in order to achieve this moment.

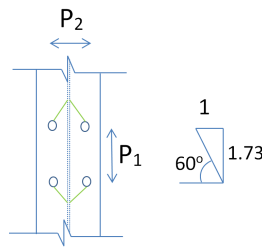


Figure 2.5. Model for determining the effective web width,  $b_{eff}$  (Kristensen 2010)

## 2.5. Torsion of the flange

Twisting of an individual flange can be idealized as a rectangular plate subjected to torque, as shown in Figure 2.6. The elastic relationship between the torque,  $M$ , and angle of twist,  $\theta$ , is given by the following:

$$M = \frac{GJ\theta}{L} \quad [2-10]$$

where  $G$  is the shear modulus of the steel and the St. Venant torsional constant,  $J$ , for the flange is:

$$J = \frac{b t^3}{3} \quad [2-11]$$

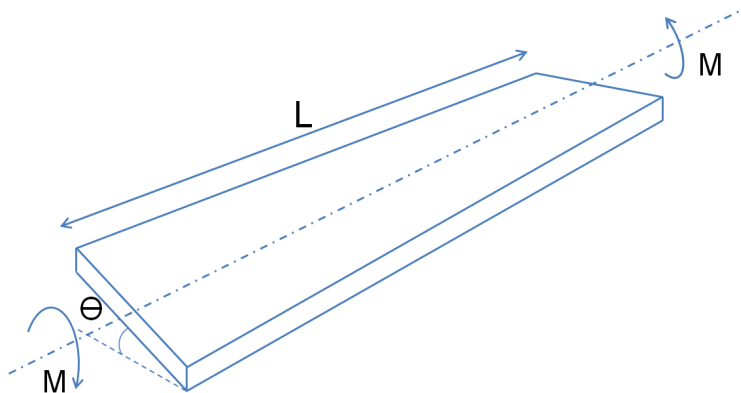


**Figure 2.6. Elastic torsion of flange**

Equation [2-10] is valid only if the flange is discrete and concentrated torques are applied, but in the case of the wide-flange member, a distributed restoring torque is also applied from the bending of the web. Load sharing is therefore a complex mechanism consisting of bending of the web and torsion of the flange, so the parameters in Equation [2-10], i.e.,  $L$  and  $\theta$ , become difficult to approximate. Evaluating the effect of the load sharing is one of the main objectives of this research.

## 2.6. Elastic torsional theory

Although the behaviour of an unstiffened W-section member is different from an equivalent one with stiffeners, elastic torsional theory can be used for comparison purposes. As such, a brief description is given here for the computation of the torsional response utilizing the whole cross-section. Principles outlined by Heins and Seaburg (1964) and Seaburg and Carter (2003) can be used for the whole cross-sectional torsion.

Non-circular cross-sections, when subjected to torsion, give rise to a phenomenon known as warping. Warping in wide-flange sections is longitudinal movement of the flanges relative to each other. The total torque can be divided into St. Venant and warping torque, and the characteristic differential equation for open sections is given as:

$$M = GJ \theta' - EC_w \theta''' \quad [2-12]$$

where  $M$  is the internal torsional moment, and the first and second terms of the equivalency are the St. Venant and warping torque components, respectively. The symbol  $\theta$  represents the angle of twist and  $C_w$  is the warping torsional constant of the cross-section.

Consider the case shown in Figure 2.7, where the member is loaded at the centre by a concentrated torque.

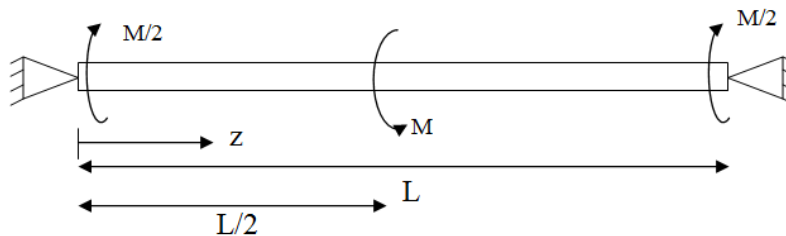


**Figure 2.7. Theoretical torsion problem**

For both rotations and warping prevented at the support boundary conditions (Figure 2.8.), i.e.,  $\theta = 0, \theta' = 0$  at both ends, solving Equation [2-12] results in the relationship for twist angle expressed in Equation [2-13]. Based on this relationship, moment–rotation comparisons have been made in this report.

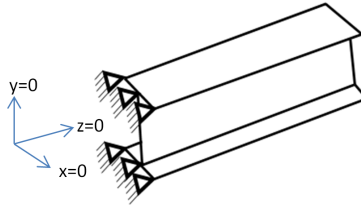


**Figure 2.8. Warping restrained boundary conditions**

$$\theta = \frac{1}{GJ} \times M \times [\lambda z + (-1 + \cosh(\lambda z)) \times \coth(0.5 \times \lambda L) + (1 - \cosh(\lambda z)) \times \operatorname{cosech}(0.5 \times \lambda L) - \sinh(\lambda z)] \quad [2-13]$$

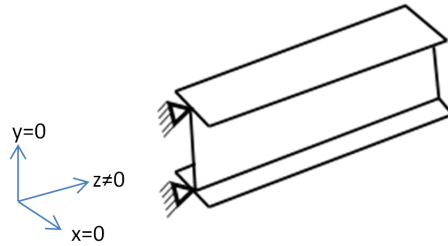


**Figure 2.9. Warping allowed boundary condition**

In the type of boundary condition where twisting is prevented, but the flanges are free to warp (Figure 2. 9), i.e.  $\theta = 0$ ,  $\theta'' = 0$ , the equation for  $\theta$  becomes:

$$\theta = \frac{1}{GJ} M \left[ z + \left( \frac{1}{\lambda} \right) \frac{\sinh(\lambda z)}{\cosh(0.5 \times \lambda L)} \right] \quad [2-14]$$

where :

$$\lambda^2 = \frac{GJ}{EC_w} \quad [2-15]$$

### **3. Numerical Analysis**

The behaviour of wide-flange members under torsion applied to one flange was evaluated with different numerical modelling techniques using the general-purpose finite element software Abaqus. Both the whole undistorted cross-section and the unstiffened case subjected to localized distortion were considered. Member geometry, boundary conditions and geometrical parameters were varied to study their effects. Procedures and details of the numerical models are presented in this chapter, along with the important results.

#### **3.1. Whole cross-section torsion**

Elastic torsion theory for open sections is well-established in the literature. In this study, torsional verification was done to validate the numerical analysis with the elastic torsional theory for W-sections. This exercise served as the first step in the development of the numerical analysis models, which were then modified for the unstiffened case. The goal was to establish the stiffness of the members where the entire cross-section rotates, and later compare it to the members that have a tendency to undergo local cross-sectional deformations.

##### **3.1.1. Shell element model**

The simplest model consisted of shell elements (S4R). The cross-section was constructed in 2D and extruded for the third dimension (member length). The loading was applied as a Static (general) Step. A concentrated torsional moment applied at the centroid of the cross-section would have distorted the element at that point, so to rotate the whole cross-section a couple of concentrated forces was applied at the junctions of the web and flanges, avoiding any local distortions due to concentrated loading. Figure 3.1 is a schematic diagram of the loading applied. In shell elements, load applied at the nodes maintains its local position and orientation as the element deforms, so as the node rotates the load applied on that node also rotates. In other words, if a concentrated load is applied at some orientation with respect to the local element, it will keep the same orientation to the element regardless of the global deformations of the part.

Rotations and displacements in all three directions were set equal to zero for the boundary conditions at the ends. However, for the warping-free boundary condition, elements at the member ends were free to displace in the Z-direction (longitudinal).

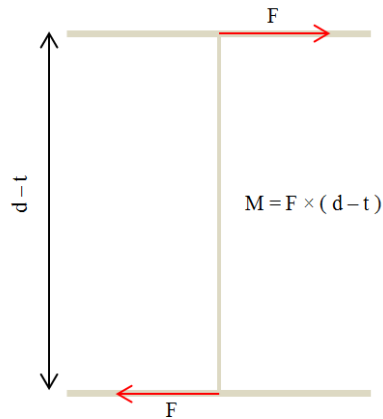


**Figure 3.1. Shell model loading**

Material properties were defined in the model to represent a “typical” Grade 350W steel. The elastic part of the curve was modelled using a modulus of elasticity of 210,000 MPa, with a Poisson’s ratio of 0.3, and the yield stress was taken as 350 MPa. The hardening strain was set at 0.017 and the ultimate true stress was 700 MPa.

### **3.1.2. Solid element model**

For the study of cross-sectional distortions and stress analysis through the thickness of the web, it was requisite to model the torsion problem with 3D elements. These elements were used to give more detailed behaviour when the web was to undergo bending. On that account, a numerical model for the whole cross-sectional torsion was created with 3D brick elements. The parts were created in a similar fashion as for the shell elements. The cross-section was drawn in the X-Y plane and extruded in the Z-direction for the given length of the member. The member was meshed using C3D4R elements. These elements are three-dimensional with four nodes, and reduced integration is employed. Studies for the mesh refinement in the workable range were also conducted. Material properties were same as those for shell model described in Section 3.1.1.

It was not feasible to apply the loading as it was applied in the shell element model, as it would have created distortions at the particular node where it was applied. Moreover, loading in solid elements does not support element rotation, so the concentrated applied load will keep the same

direction as the member rotates. Two different loading methods were used to simulate the entire cross-sectional rotation.

In the first method, a rigid plate, made up of shell elements, was created and was cut out in the centre to the cross-sectional dimensions of the W-section member, as shown in Figure 3.2. This rigid plate was then tied around the member. A reference point was created at the centroid of the plate and the concentrated moment was applied at that reference point. This rigid plate forced the cross-section of the main member to rotate entirely without any local cross-sectional distortions.

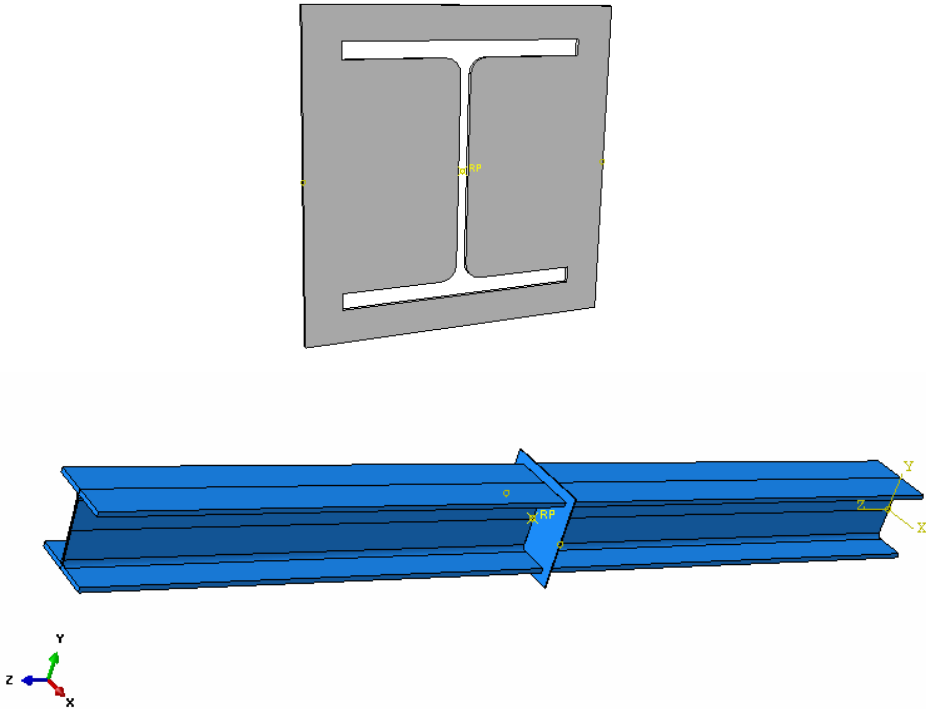


**Figure 3.2. Solid model rigid plate and assembly**

The second method was similar to the one shown in Figure 3.1, except instead of concentrated loads, pressure was applied on two defined small surfaces to create the torque. This pressure remained normal to the surface as the member rotated. Figure 3.3 is the illustration of the loading applied on the member. (The discontinuity gaps in the flanges are the removed elements from the view just for the visual depiction of the loading locations.) Local distortion of flange elements was thereby avoided, as the pressure load was applied on a larger area compared to a concentrated load. The two methods of preventing cross-sectional distortion produced the same results.

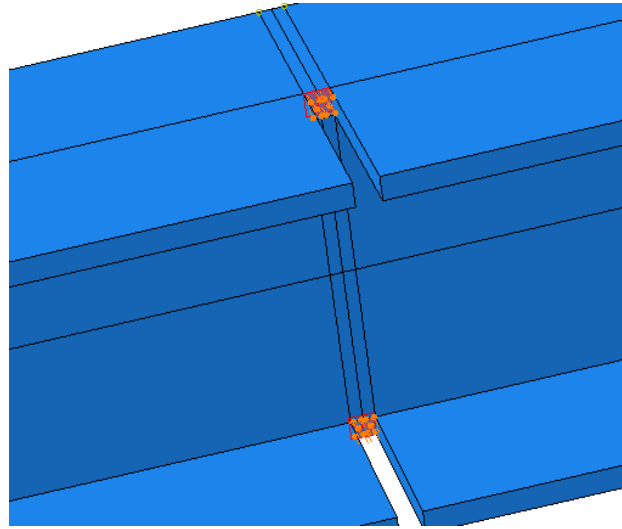


**Figure 3.3. Solid model pressure couple loading**

Boundary conditions in solid elements are only governed by displacements of the nodes. Rotation and translation at the ends of the member were restrained by restraining the X and Y displacements at these locations. For the warping-permitted case, displacements at the ends in the Z-direction were not restrained; a few nodes on the web on one end were restrained in the Z-direction to make the model globally stable.

It could be a valid argument that as the member rotates, axial shortening takes place and due to the boundary condition not permitting any displacements in the Z-direction, an axial tensile force gets generated in the member. This axial force could alter the results compared to a member with only torsional moment, so this behaviour was investigated by modelling another method. A thick plate with a very high modulus of elasticity was tied to one end of the member, which prevented the warping of the flanges. For this plate, displacements were restrained in the X- and Y-directions, but unrestrained in the Z-direction. This plate prevented warping, but allowed the member to shorten and prevent the development of axial tension. It was observed that this effect had a negligible influence on the stiffness in the elastic range, which is the range of interest in the following discussions.

For shell elements, rotations of the nodes can be directly obtained while post-processing the data. Similarly, in the solid element model where loading is applied through the rigid plate, rotation of the reference node can be taken. However, for the model that contains only solid elements and where loading is not applied through a rigid plate, rotation can be calculated from the displaced

coordinates of two points on the cross-section. These two points were selected to be on the web of the member near the web-to-flange junction. Figure 3.4 depicts the calculation method for the rotation based on the displacements of Points A and B, where the origin is at the cross-sectional centroid.

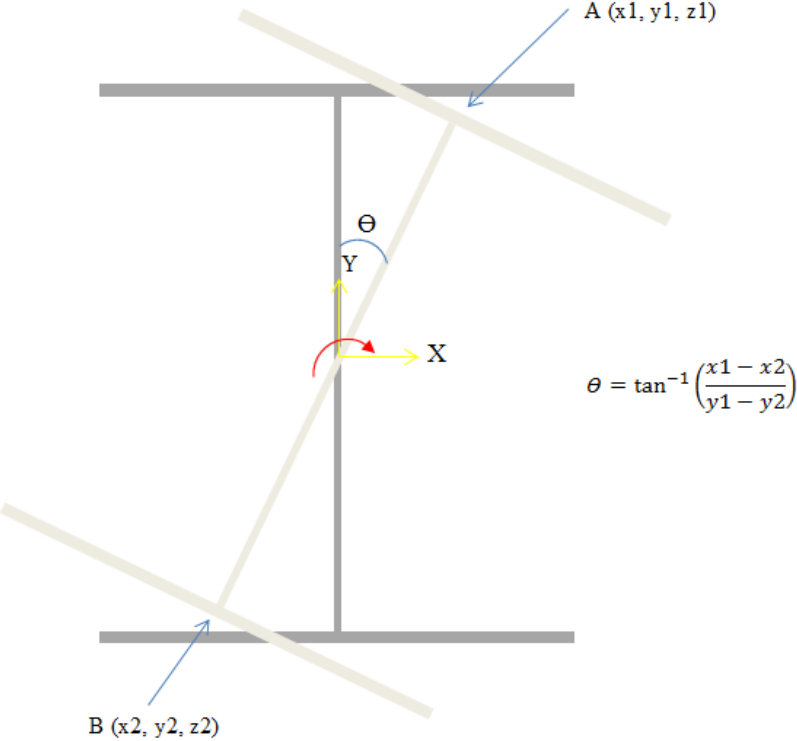


**Figure 3.4. Rotation calculation**

**3.1.3. Results for torsion on entire cross-section**

Figures 3.5 to 3.7 show the moment–rotation response curves of a W310×129 section as the length of the member is increased from 2 m to 8 m. “Restrained” stands for the case where warping-prevented boundary conditions are provided at the both ends, whereas the warping-allowed case is indicated by “Unrestrained”. The “Theoretical” series has been plotted based on a classical elastic analysis for the torsion of the member using Equations 2-13 and 2-14. “Solid” and “Shell” stand for the results from the solid element model and shell element models, respectively.

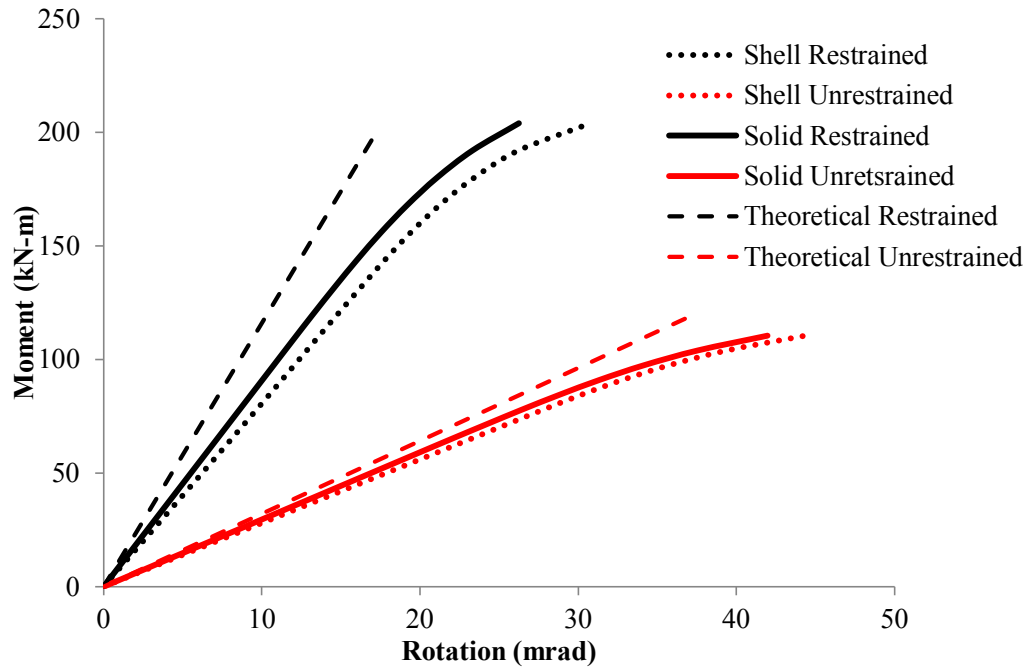


Figure 3.5. Torsion results of 2 m long member

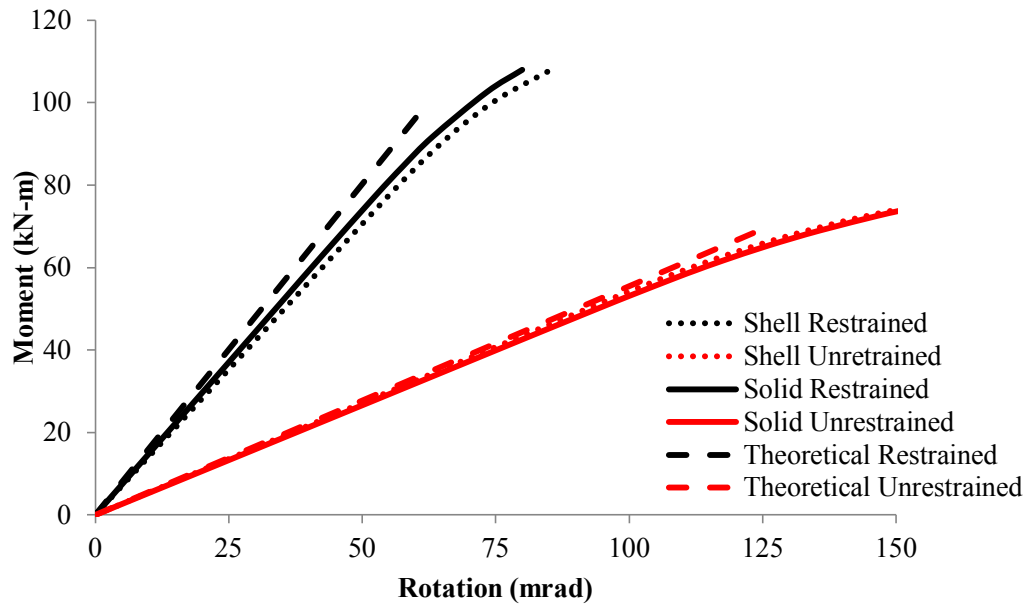
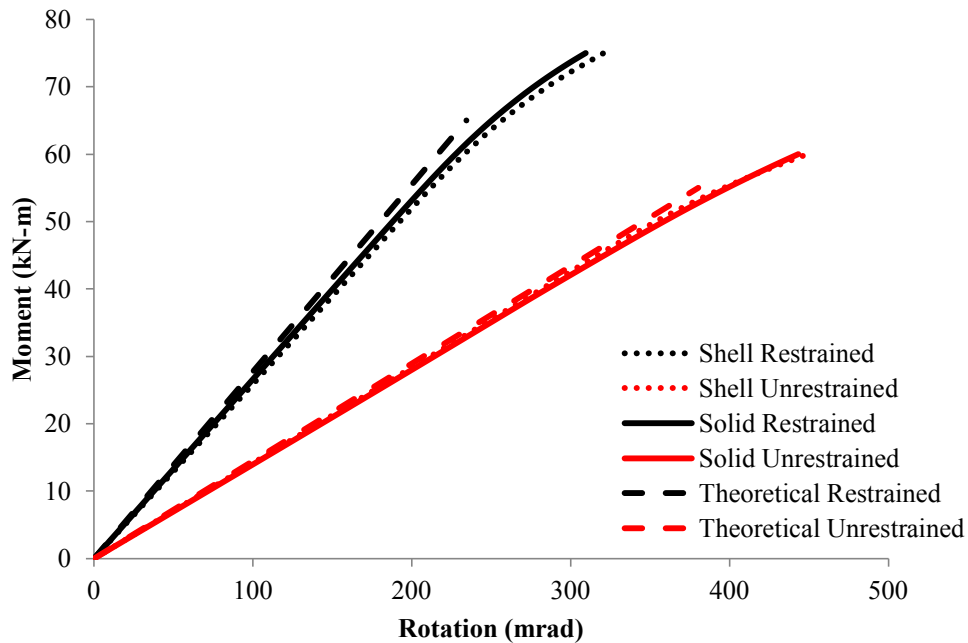


Figure 3.6. Torsion results of 4 m long member



**Figure 3.7. Torsion results of 8 m long member**

In general, results from the solid and shell element numerical models match well. However, the stiffness obtained by the numerical models is slightly less than that given by the elastic theory. This fact is most prominent in members with the “shorter” lengths, as the theory assumes an idealized transfer of the torsional load and reactions into the member cross-section. Nonetheless, as the length is increased, this effect dissipates and results from the numerical analysis and theory start to converge. To investigate this further, the length was increased significantly and Figure 3.8 shows the numerical analysis results of the W310×129 member with a length of 18 m. Only shell elements were used to obtain this result, as the solid element model provides similar results and would have been computationally expensive. The resulting stiffness is almost exactly the same as that predicted by the theory.

The torsional response of the member was further investigated by changing the cross-sectional dimensions. Figure 3.9 shows the cross-sectional dimensions considered, which are modified from the standard W310×129 section. HT represents a member where the flange and web thicknesses have been reduced to one-half of the standard thicknesses of a W310×129, DT represents the case where the thicknesses of the flanges and web have been doubled, and AT represents the standard dimensions.

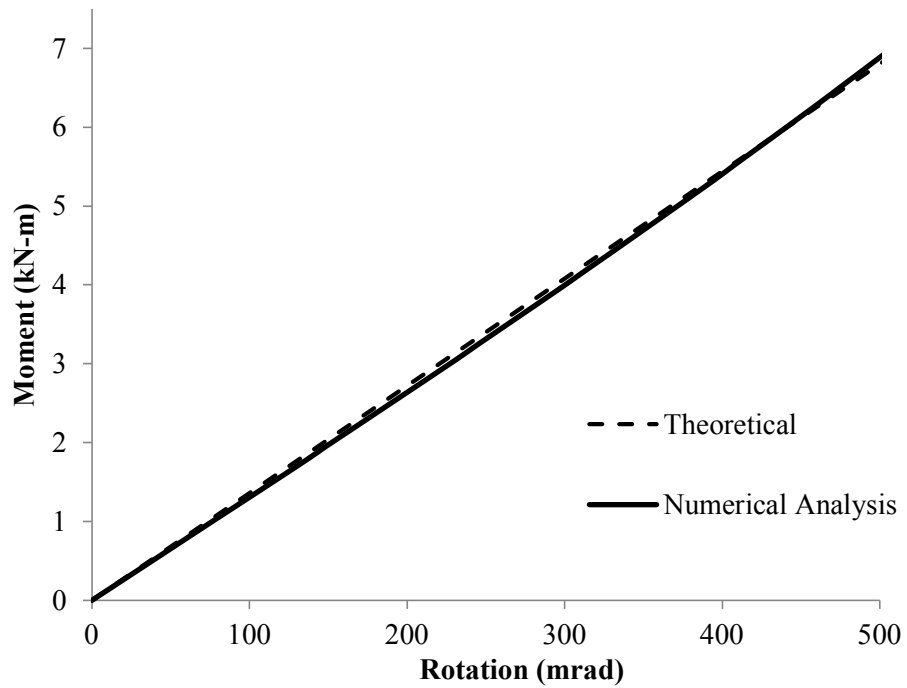


**Figure 3.8. Torsion results of 18 m long member**

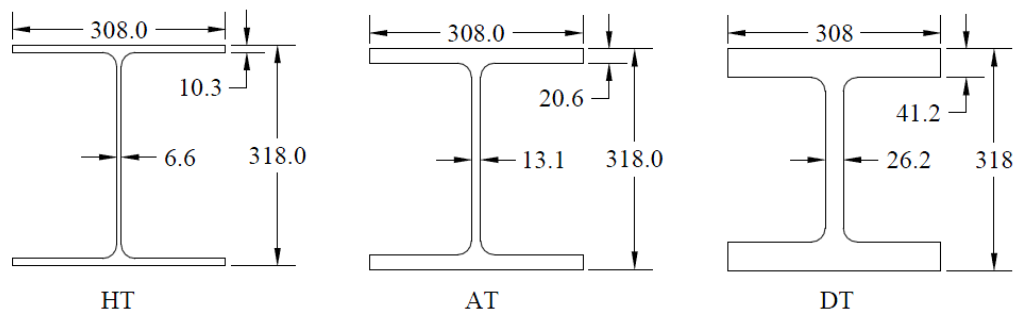


**Figure 3.9. Modified cross-sectional dimensions**

Figure 3.10 shows the moment–rotation curves for all three sections, using a length of 8 m. The greatest under-prediction of stiffness compared to the theoretical curve occurs for the stockiest member, whereas the result for the lightest section matches very closely with the theoretical calculations. However, it was observed that as the length is increased the stocky cross-section also converges to the theoretical stiffness results.

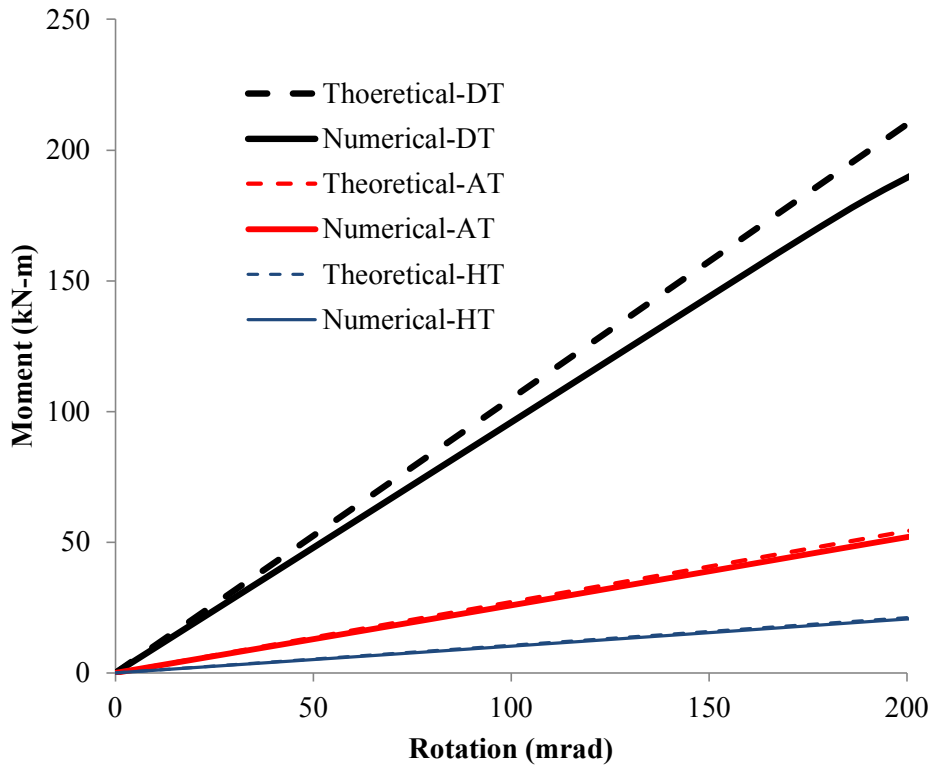


Figure 3.10. Modified cross-section torsion results (8 m long)

## 3.2. Numerical analysis with stiffeners

### 3.2.1. Full member and joint assembly

The torsion applied to the models discussed in the previous section rotated the whole cross-section, but the manner in which the loading was applied does not represent how loading is generally applied on the member. In most practical applications, it is a reaction from an adjacent member. Proceeding to a more practical case, as shown in Figure 1.3, a full member and joint assembly of that structure was replicated in Abaqus. As the application required, the full 3D model was created using 3D solid elements. Details of the various parts are discussed in the following.

#### Column

The column was created by defining the cross-section in the local X-Y plane and extruding it in the third dimension for a height of 4 m. The 26 mm diameter holes were cut-extruded for the

dimensions given for the connection detail in Figure 1.3 to accommodate the bolts. The column part is shown in Figure 3.11.

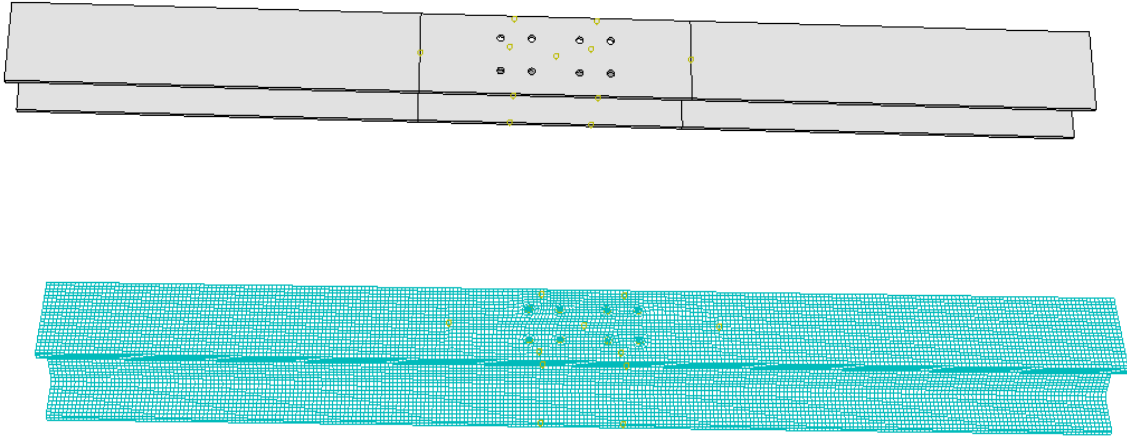


**Figure 3.11. Column part with attributed mesh**

**Beam**

The beam was also extruded in a similar manner to the column for the cross-sectional dimensions of a W310×79. The beam was modelled as a cantilever part, where out-of-plane loading applied to the beam could be transferred to the column as torsion. One end of the part was modified so that a pressure could be applied, instead of point loads, to enable the beam to rotate in a circumferential manner. The beam part is shown in Figure 3.12.

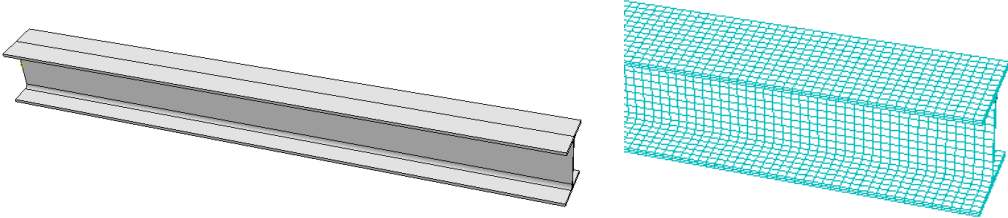


**Figure 3.12. Beam part with corresponding mesh**

## Endplate

A rectangular end plate was extruded through a thickness of 25 mm. The cross-sectional dimensions of the plate were selected to contain the beam cross-section and the connection details in Figure 1.3. The holes in the plate were positioned to align with the column holes.

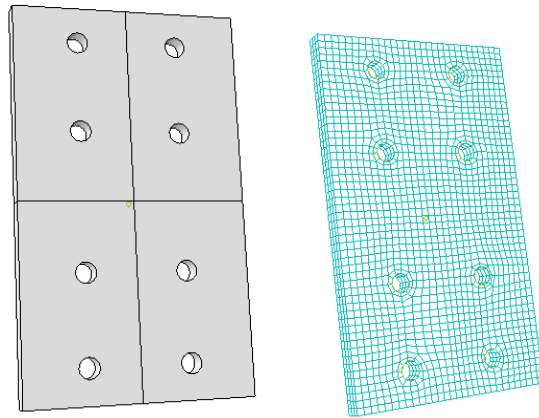


**Figure 3.13. End plate with corresponding mesh**

## Bolts

Bolts were created by the “Solid Revolve” option of Abaqus. Dimensions were selected to replicate 25 mm (1 in.) diameter A325 bolts. However, many details were simplified for practical purposes. The bolt head and nut were modelled with the same dimensions, and the bolt shank length was selected to match the thicknesses of the end plate and flange, as shown in Figure 3.14. Material properties for the bolts were selected as those used by Salem and Driver (2013). An axis was defined, along which pre-loading would be applied.

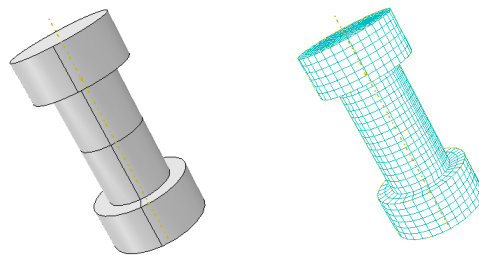


**Figure 3.14. Bolt part with assigned mesh**

## Stiffeners

Stiffeners were modelled for a thickness of 20 mm. The shape and dimensions of the stiffeners were selected to fit within the column section.

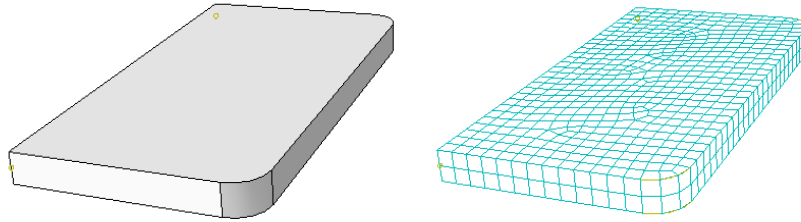


**Figure 3.15. Stiffener with corresponding mesh**

After the creation of the parts, they were assembled to ensure a realistic loading mechanism. One end of the beam was tied to the end plate with the surface-to-surface tie option of Abaqus. Stiffeners were similarly tied to the column opposite the beam flanges. Bolts were positioned to clamp the end plate and column flange. The entire assembly is shown in Figure 3.16.

Hard contact was used to model the interaction between the contact pairs: column–end plate, bolts–endplate, and bolts–column. Abaqus’ automated contact pairs recognition option was used to identify master and slave surfaces. Pairs were also automatically selected by the software to enhance the processing. Tangential and normal contact properties were defined with a coefficient of friction of 0.3 between all surfaces, and Abaqus’ default contact algorithm was employed for contact interpretations.

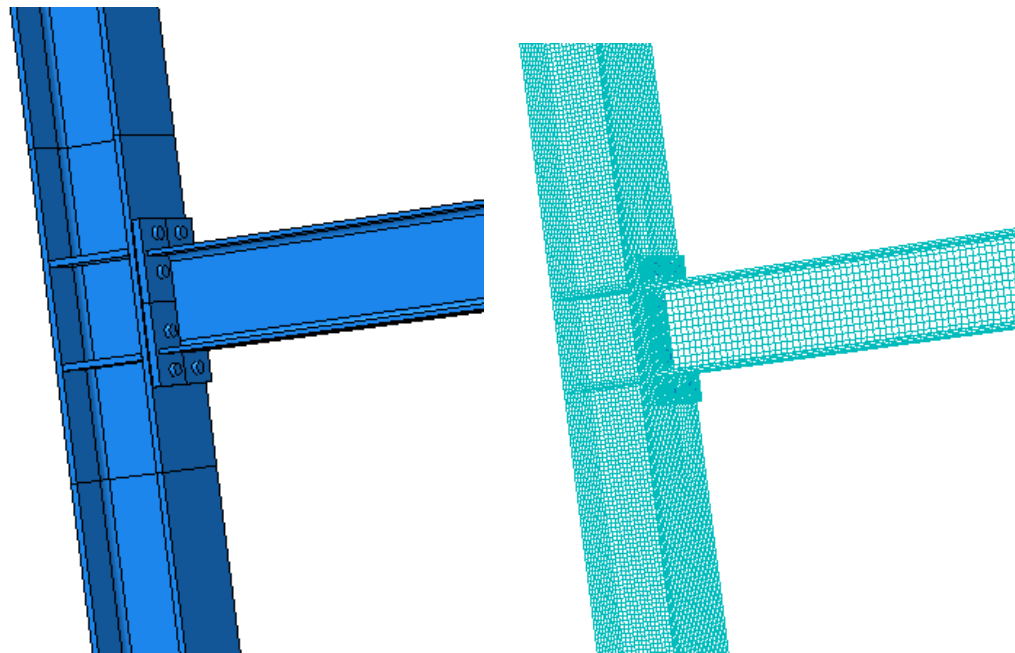


**Figure 3.16. Entire assembly with mesh**

The boundary conditions were applied at the ends of the column to restrain the nodes from moving in any direction. As such, the ends were torsionally fixed.

Loading was applied in two steps. In the first step, a pre-tension load of 55 kN was applied on the bolts. In this step, contact was initiated. Cantilever loading was then applied in the second step, which was conveyed to the column through the end plate and bolts. This loading was further carried from the flange to the entire cross-section by the stiffeners between the flanges.

Applied moment on the flange can be calculated as the product of the beam length, including the end plate, and equivalent force resulting from pressure applied at the end of the beam. The rotation of the flange was determined in a similar way to that shown in Figure 3.4, but using the displaced coordinates of the flange tips.

### **3.2.2. Results for torsion with stiffeners**

The response of the W310×129 column with torsionally fixed boundary conditions for the full member and joint assembly is plotted in Figure 3.17. The model with the stiffeners (ST) shows slightly greater stiffness as compared to the solid-model curves in Figures 3.6 and 3.7, reproduced

in Figure 3.17, since the stiffeners reduce the distance between the applied loading and support. Figure 3.18 depicts the principal reason for the difference in results.

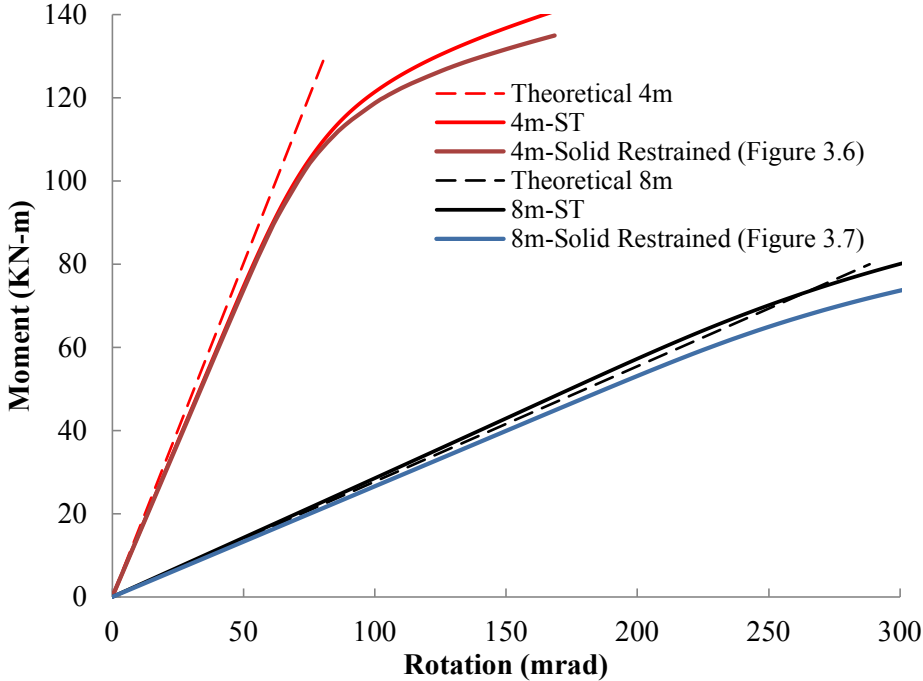


Figure 3.17. Torsion with stiffeners

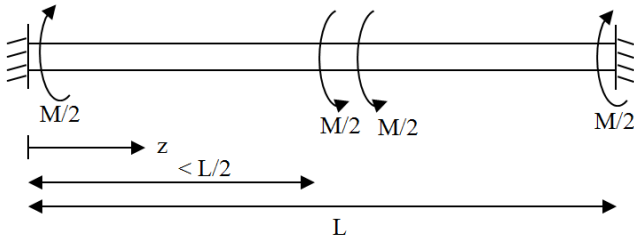


Figure 3.18. Schematic of torsion with stiffeners

### 3.3. Torsion without stiffeners

The model described in Section 3.2 was altered to get the unstiffened response of the member. The stiffeners were suppressed, keeping all other properties of the model unchanged.

A W310×129 member loaded torsionally at mid-length through one flange, considering overall member lengths of both 4 m and 8 m, was modelled with and without stiffeners using the finite element method, and a plot of the applied moment and corresponding rotation is shown in Figure 3.19. As expected, there is a significantly lower moment capacity, as well as stiffness, in cases where no stiffeners are provided (NST), and the difference is larger where the length of the member is shorter. In the case of the 4 m-long member, the elastic stiffness is 66% lower than that of its stiffened counterpart (ST), whereas for the 8 m-long member it is 22% lower. The elastic portions of the curves for the stiffened members agree well with classical elastic torsion theory, denoted “Theoretical” in the figure. Moreover, while the onset of inelastic response occurs at a much lower moment in the longer member when stiffened, when unstiffened there is little or no difference. In both cases, it occurs at a much greater rotation in the longer member.

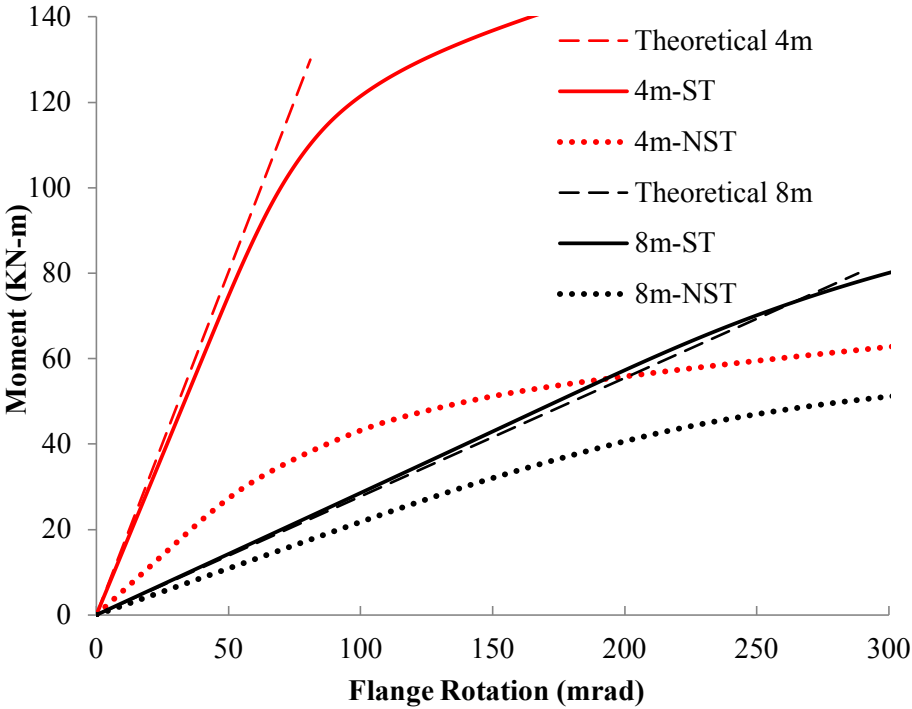


Figure 3.19. Stiffened vs. unstiffened torsion

**3.3.1. Effect of depth of stiffener**

For full utilization of the torsional capacity of the member, stiffeners generally must fully extend between the flanges and be connected to both the flanges and the web. In the case of discontinuous stiffeners between the flanges, local web bending can occur at the root of the stiffener where it

terminates. Different scenarios with stiffeners extending half the distance between flanges, three-quarters the distance, and full-depth have been compared with the unstiffened case for a 4 m-long W310×129 member loaded torsionally at mid-length. Stress distributions and deformed shapes at an applied moment of 30 kN·m are shown for all models in Figure 3.20. Figure 3.21 is a moment–rotation plot for the corresponding models. The cost of installing the stiffeners represented in Models B and C is effectively equivalent, with a premium being imposed for those in Model D due to the fitting and welding of the stiffeners to both flanges. Most importantly, however, the cost represented by Model A without stiffeners would be substantially lower than any of the stiffened options, so the importance of being able to determine accurately the torsional moment capacity of a member without stiffeners is highest when the applied moment is small compared to the full cross-sectional capacity in case stiffeners can be eliminated entirely. For the same reason, it is also important that the torsional demands be calculated accurately, rather than being chosen “conservatively” from an overly simplified analysis. Detailed parametric behaviour for the unstiffened member has been explored in this report.

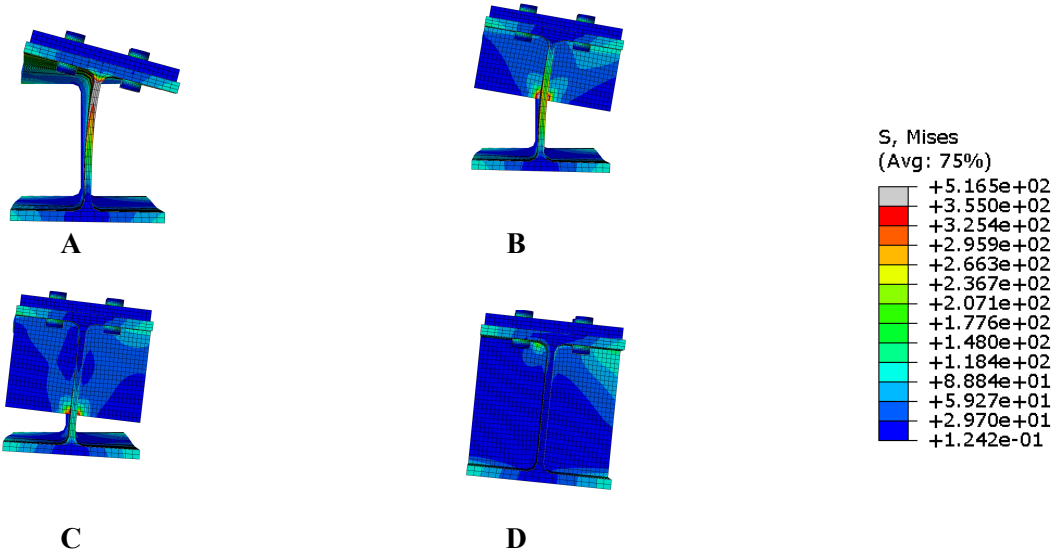
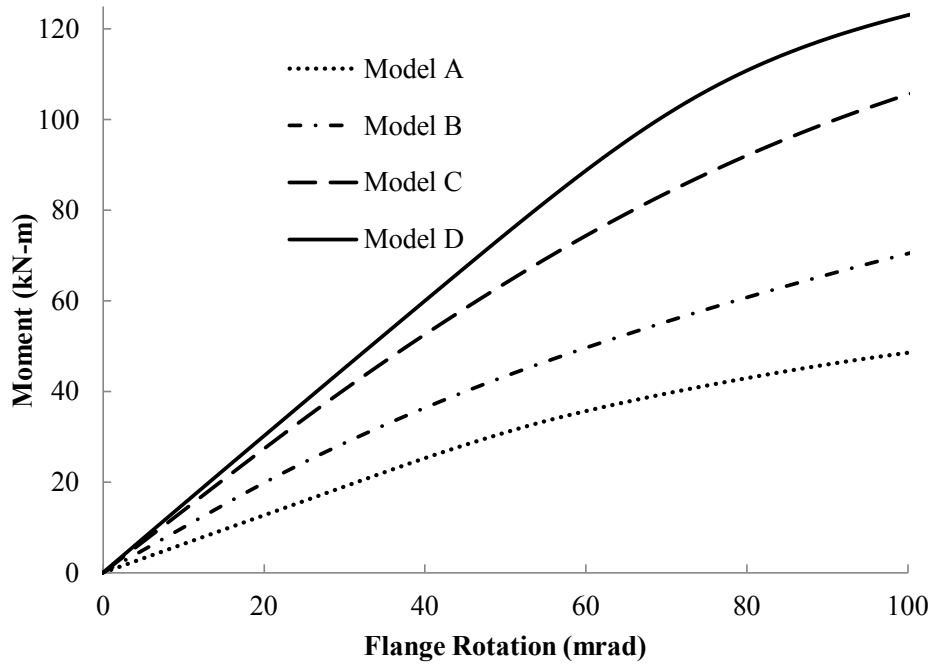


Figure 3.20. Stresses and deformed shapes of cross-section with various stiffener geometries



**Figure 3.21. Effect of stiffener geometries on moment–rotation response**

### 3.3.2. Simplified loading

A simplified model, shown in Figure 3.22, can potentially serve the purpose of load application, with considerably less modelling effort than for the full member and joint assembly. Pressure is applied at the bolt locations perpendicular to the flange surface and it remains perpendicular throughout the analysis, thus creating a couple that applies the torsional moment to the flange. The use of pressure is advantageous because concentrated loads on solids using brick elements do not support nodal rotation and therefore as the flange rotates, the force maintains the same direction as applied initially. In addition, much of the localized element distortion that can occur under a point load is avoided by applying pressure on a larger area.

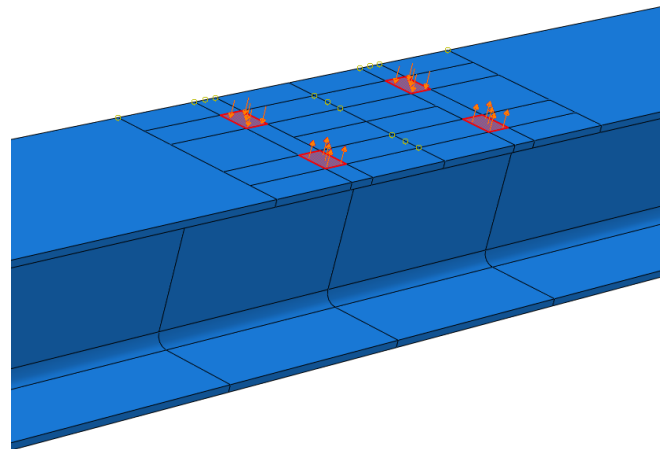


**Figure 3.22. Simplified loading model**

To facilitate comparisons of different model cases while varying the key geometrical parameters, the notation shown in Figure 3.23 is adopted, where the symbols L, D, B, W, and F represent the member length, depth, flange width, web thickness, and flange thickness, respectively. The units are millimetres except for the length, which is in metres. Figure 3.24 depicts the resultant moment-rotation responses obtained by the two different loading schemes for model 4L-300D-300B-8W-12F, which is a wide-flange column section with a length of 4 m, section depth of 300 mm, flange width of 300 mm, web thickness of 8 mm, and flange thickness of 12 mm. There is only a very small difference in the results, particularly within the initial loading stages. For this reason, the simplified loading method is used in the remainder of this research.

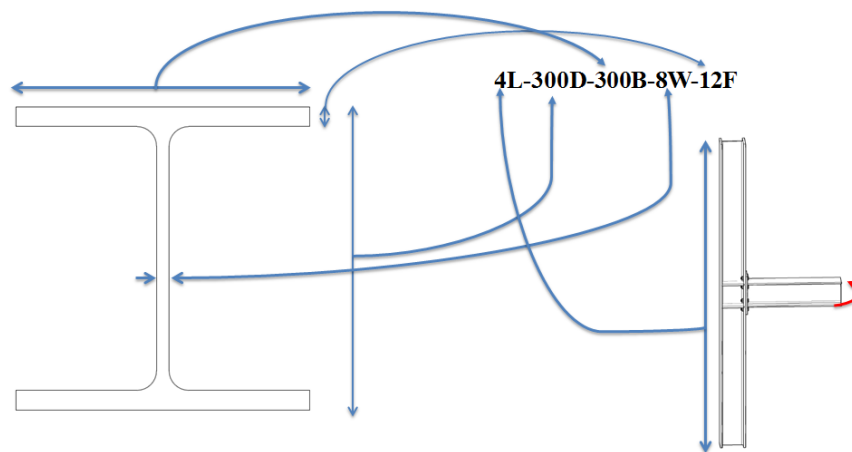


**Figure 3.23. Notation used in parametric study**

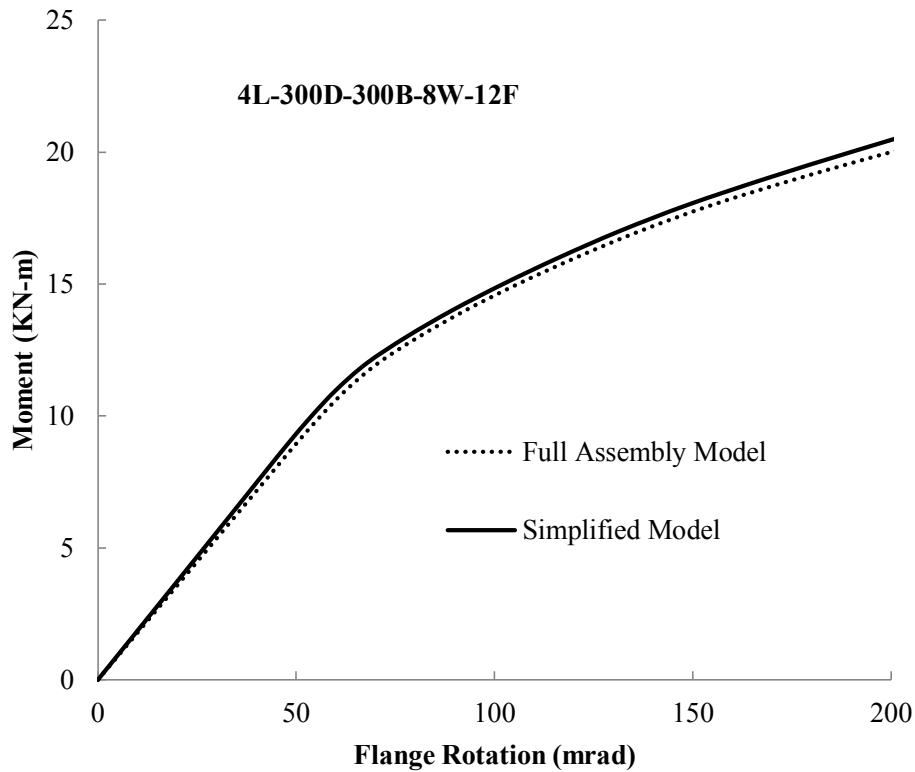


**Figure 3.24. Full-assembly vs. simplified loading model results**

### **3.3.3. Boundary conditions effect**

Torsional stiffness is influenced by the boundary conditions at the member ends, even for unstiffened members that tend to deform locally. Figure 3.25 shows the response of a 4 m-long unstiffened W310×129 member with warping restrained at both ends in comparison to an equivalent case where warping at the ends is unrestrained. Boundary conditions with warping unrestrained were implemented by preventing displacements of all the end nodes within the plane of the cross-section, but releasing the displacements perpendicular to this plane (i.e., along the axis of the member). For the case with warping restrained, nodal displacements in all three directions were fixed. In order to provide comparisons among geometric parameters only, all models in the parametric study described in Section 3.3.5 have boundary conditions where warping is restrained.

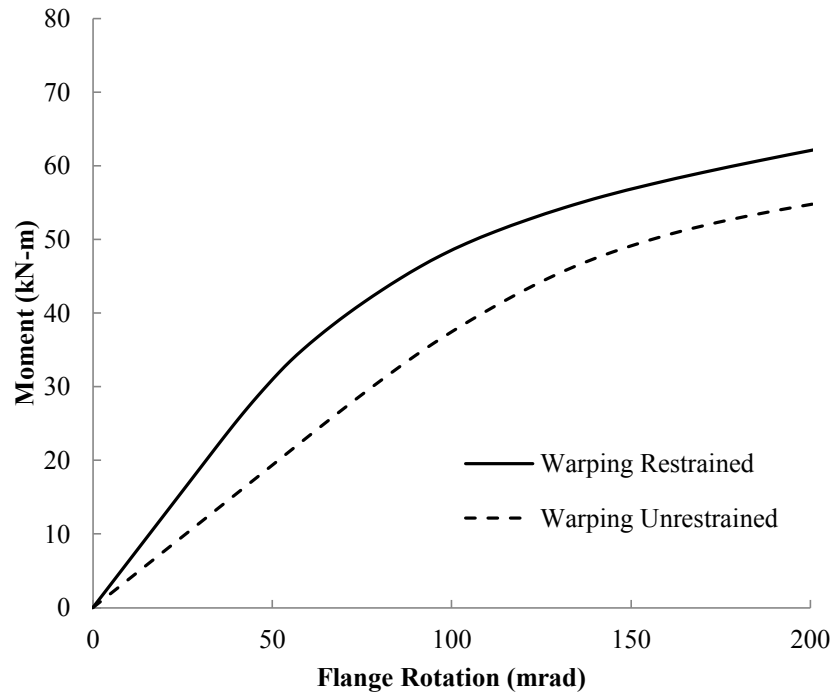


**Figure 3.25. Effect of warping boundary conditions on unstiffened member**

### 3.3.4. Mesh refinement

To examine the local web and flange distortional behaviour, solid 3D brick elements were selected. Refinement in the stress variation through the thickness was achieved by increasing the number of elements through the web thickness. Three elements through the thickness with reduced integration resulted in a poor representation of the variation of stress from one element to another, whereas with four elements and full integration a gradual change in the stress, without discontinuities, was achieved. Furthermore, reduced integration resulted in less stiffness, as depicted in Figure 3.26, and inconsistent stiffness comparisons were observed in the parametric study. As a result, for the parametric study presented in the next section, full integration was utilized with three elements through the flange thickness and four for the web in the central region of the member.

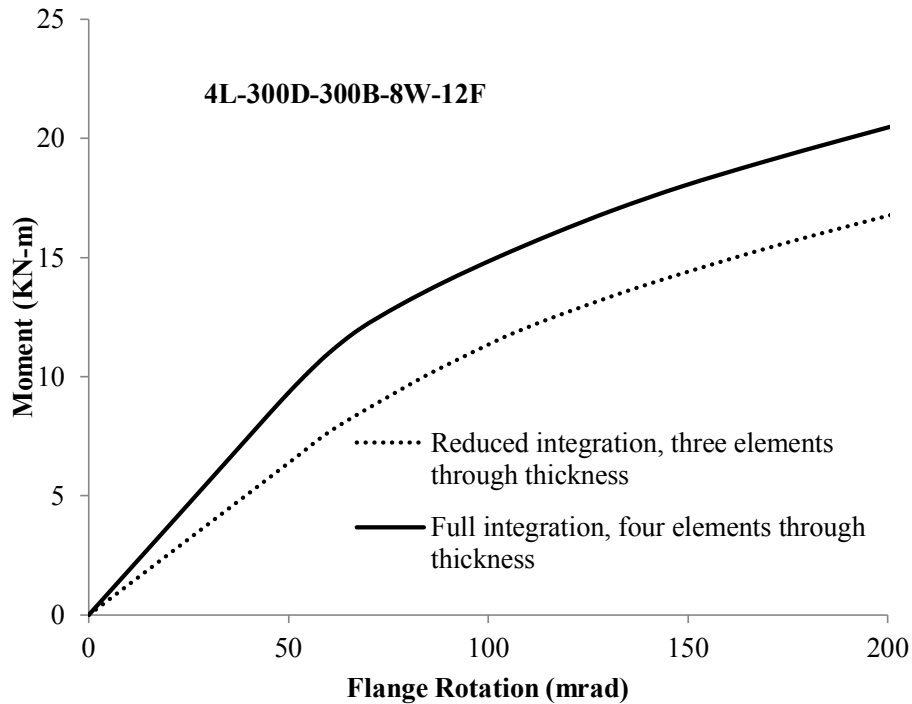
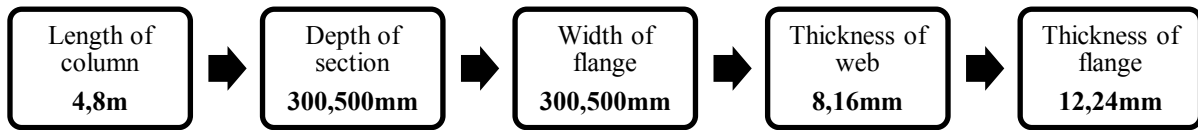


Figure 3.26. Effect of number of elements through web thickness and integration technique

### 3.3.5. Parametric study

The torsional resistance mechanism of unstiffened wide-flange members can be devolved into two main components: torsion of the flange and bending of the web. Torsion of the flange can be idealized as a rectangular plate subjected to the torque, for which the significant geometric parameters are the flange width and thickness. For web bending, the web thickness is of primary importance. Section depth was also considered in the parametric study as it imparts stiffness variation during bending of the web. Another important parameter is the length of the member, which influences both of the resistance components, as well as the overall stiffness of the member. Based on these considerations, five geometric parameters were selected for the parametric study and the combinations examined are shown in Figure 3.27. It is important to note that the parameters are selected to study their influence on torsional response of the member, rather than to result in typical cross-sectional dimensions.



**Figure 3.27. Parameters with combination values**

Figure 3.28 is a typical plot of applied torsional moment and resulting rotation of the flange to facilitate the explanation of general behaviour. Von Mises stress plots at different applied moments are shown for the overall member in the loaded region and for the corresponding web cross-sections at the web-to-flange junction over a length of 875 mm in Figures 3.29 and 3.30, respectively. Referring to Figure 3.28, before point “A” the member shows elastic behaviour. Yielding at the surfaces of the web cross-section starts at this point (grey in Figures 3.29 and 3.30) and progresses towards the middle surface up to point “B”. A gradual decline in the slope of the curve can be observed after appreciable yielding in this range causes material softening. The entire web thickness becomes plastic at point “B”, whereas the flange remains elastic. Initiation of yielding at the surface of the flange occurs at point “C” and the entire flange thickness adjacent to the applied torque becomes plastic at point “D”. It can be observed that both the web (“A” to “B”) and the flange (“C” to “D”) yield gradually by the continuous rotation of the flange. Any inelastic solution must account for the large flange rotation, which approximately doubles from the values shown in Figure 3.28 if the length is doubled.

While the full torsional response of a member is of interest for characterizing the overall behaviour, practical limits must be placed on the rotation of the flange for design purposes. In a real structure, these members may also be subjected to other loadings in addition to torsion. For example, excessive rotation of the flange could compromise the axial load carrying capacity of the member. Therefore, it is necessary to limit the rotation of the flange in order to avoid any compromise to the capacity of the member under other loadings. Design standards do not address this issue directly, so limit criteria must be sought elsewhere. ASTM Standard A6 provides the maximum out-of-plane rotation of the flange for rolling mill practices, which is dependent upon the cross-sectional dimensions and varies from about 20 mrad for a 300 mm wide flange to 60 mrad for a 100 mm wide flange for W310 sections and smaller, and 20 mrad for a 400 mm wide flange to 40 mrad for a

200 mm wide flange for sections larger than W310. This tolerance is only intended as an initial imperfection limit, so it serves as a point of reference, but is generally too restrictive to be used as an ultimate limit state. Winter et al. (1949) demonstrated that for a braced channel beam the capacity decreases significantly as the overall rotation of the section is increased beyond 3 degrees (52 mrad). Again, this is not an ultimate limit state for the design case under consideration, but can be taken as another point of reference.

As a practical limit to the rotation of the flange that is independent of the cross-sectional dimensions and prevents the accelerated rotation arising from inelastic straining, Point “A” (initial yield) of Figure 3.28 has been taken as the moment capacity of the member. At this point, if the member is unloaded it can retract back to its original position. Up to this point, the behaviour of the member is elastic; therefore, the response of the unstiffened web under torsion combined with other loadings such as axial force can be characterized using elastic interactions. Details for this interaction are discussed in this report in Chapter 5. The initial yield point is also considered the reference point to compare the elastic capacity results of different models in this report. From the numerical models, the initial yield point has been computed using the parameter PEEQ (equivalent plastic strain) for the precise estimation of the initiation of yielding in the member.

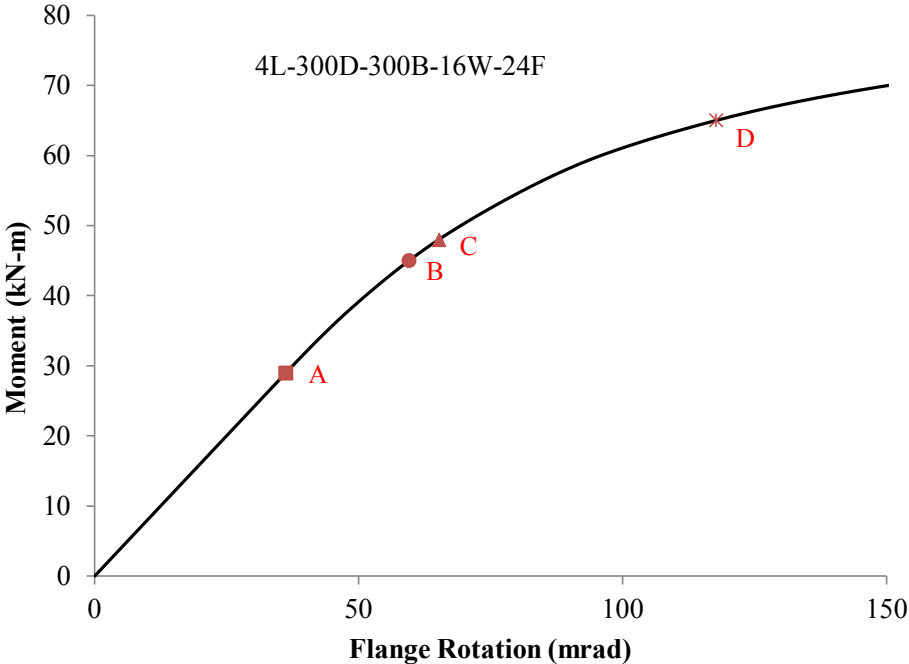
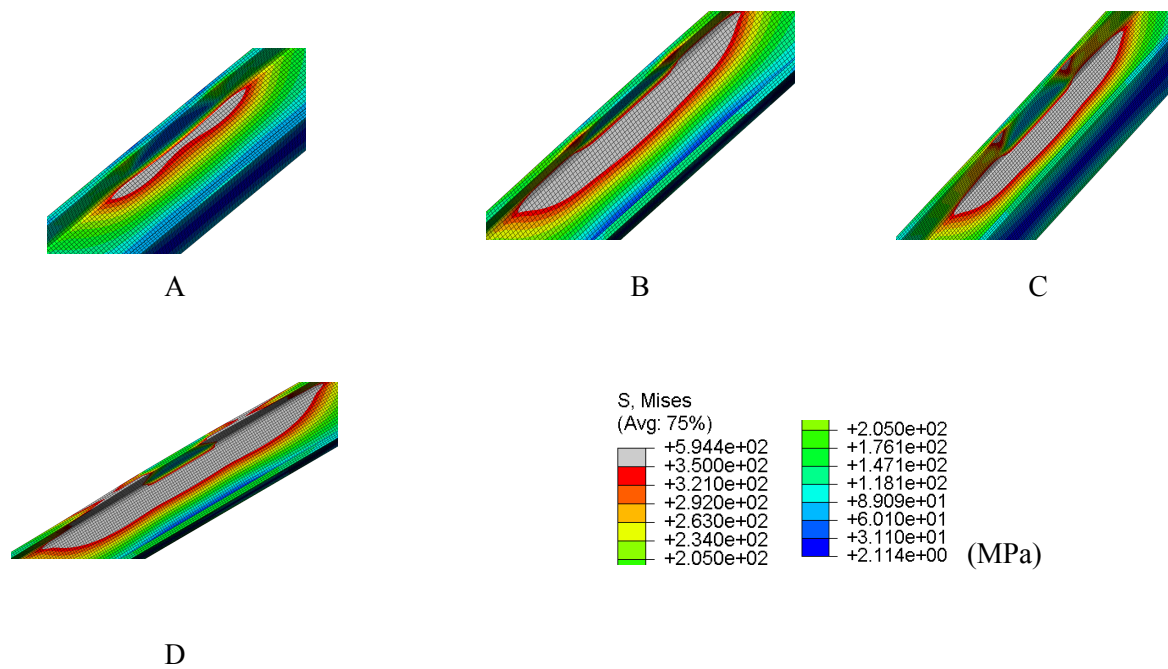
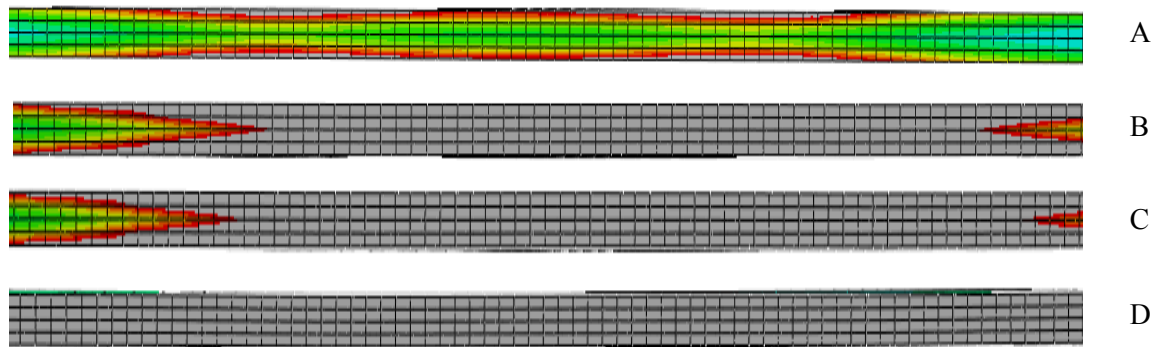


Figure 3.28. Typical moment-rotation response



**Figure 3.29. Stress plot for web surface at various moments**  
(see Figure 3.28)



**Figure 3.30. Stress plot for cross-section of web at various moments**  
(see Figure 3.28)

### Flange thickness

Increasing the flange thickness from 12 to 24 mm results in a significant increase of resisting moment, but this effect is less conspicuous when the web is thicker, as the flange's relative contribution to the moment resistance decreases. Figure 3.31 shows selected results by varying the

parameters. Comparing models 4L-300D-300B-8W-12F and 4L-300D-300B-8W-24F, not only is there is an increase in the moment by thickening the flange, there is also an increase in the initial stiffness, as expected.

### **Web thickness**

Bending strength and stiffness of the web is decidedly affected by its thickness. The resisting moment and stiffness are both enhanced significantly by increasing this variable. Representative curves in Figure 3.31 are those for models 4L-300D-300B-8W-12F and 4L-300D-300B-16W-12F.

### **Flange width**

Increasing the flange width adds both resisting moment and stiffness. However, as illustrated in Figure 3.31, by comparing the curves for models 4L-500D-300B-8W-12F and 4L-500D-500B-8W-12F, in comparison to the flange and web thicknesses, the flange width has considerably less influence.

### **Depth of section**

As the yielding due to bending of the web initiates at the junction of the web and flange, it was observed that the depth of the section has a comparatively smaller effect than all of the other parameters investigated in terms of both strength and stiffness. This can be seen by comparing the curves for models 4L-300D-300B-8W-12F and 4L-500D-300B-8W-12F in Figure 3.31.

### **Length of member**

A considerable decline in the initial slope of the moment–rotation curve can be observed by increasing the length from 4 m to 8 m (in Figure 3.31, models 4L-300D-300B-8W-12F and 8L-300D-300B-8W-12F, respectively). While this decline is expected for stiffened members and can be justified by classical elastic analysis, the localization of the resistance mechanism in the unstiffened case reduces the influence of this parameter somewhat. An important thing to note is that even though the longer length gives rise to a lower stiffness, if the onset of yielding is to be the torsional limit state, both lengths achieve approximately the same capacity for unstiffened webs.

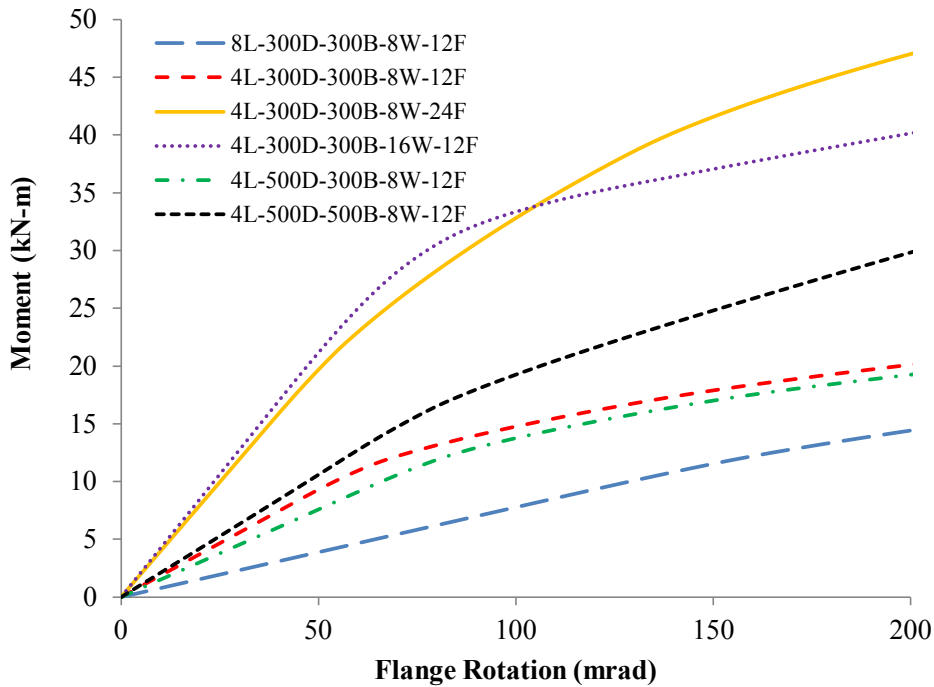


Figure 3.31. Parameter comparisons

### 3.4. Numerical analysis of selected W-sections

#### 3.4.1. Strength and stiffness

The parametric study models discussed in Section 3.3.5 have large variations in the cross-sectional properties; however, in standard wide-flange sections the variation is somewhat less profound. Also, any method to predict the behaviour of the member should account for the sections being used for practical purposes. For these reasons, standard sections from the *CISC Handbook of Steel Construction* (CISC 2011) were selected for further numerical analysis. All the sections within the flange thickness range of 12 to 24 mm in the nominal depth range of W250 to W410 were chosen. The maximum flange width used in the parametric study of 500mm was kept, but the lower limit of 300mm was relaxed to include additional W250 sections and some sections that are more commonly used as beams than columns in other depth groups.

Figure 3.32 shows graphically the numerical analysis results of these sections for the maximum elastic moment (initial yield moment). Figure 3.33 is a plot of the member stiffnesses with a 4 m length and warping-restrained boundary conditions.

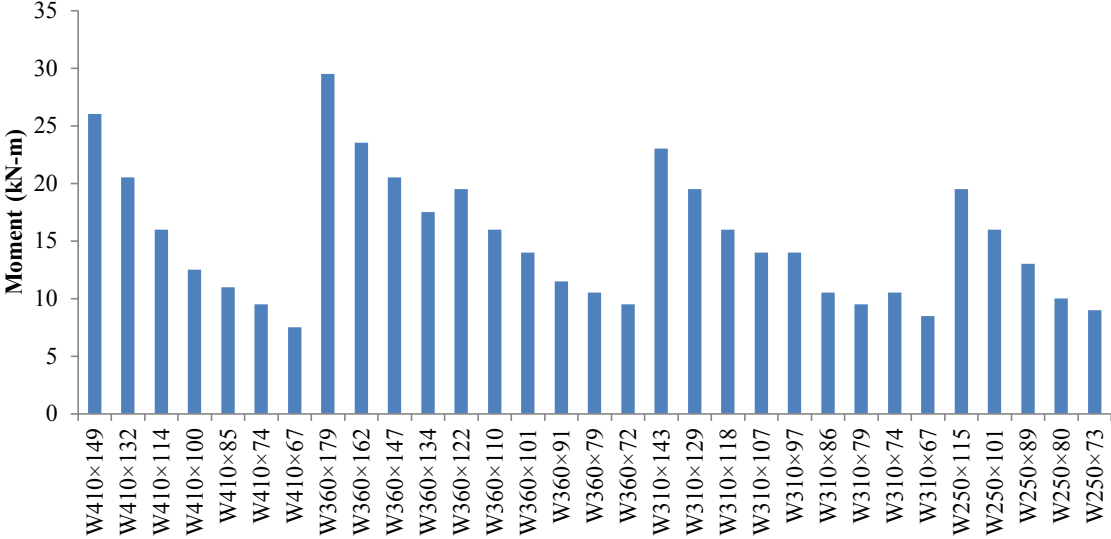


Figure 3.32. Maximum elastic moment predicted by numerical analysis

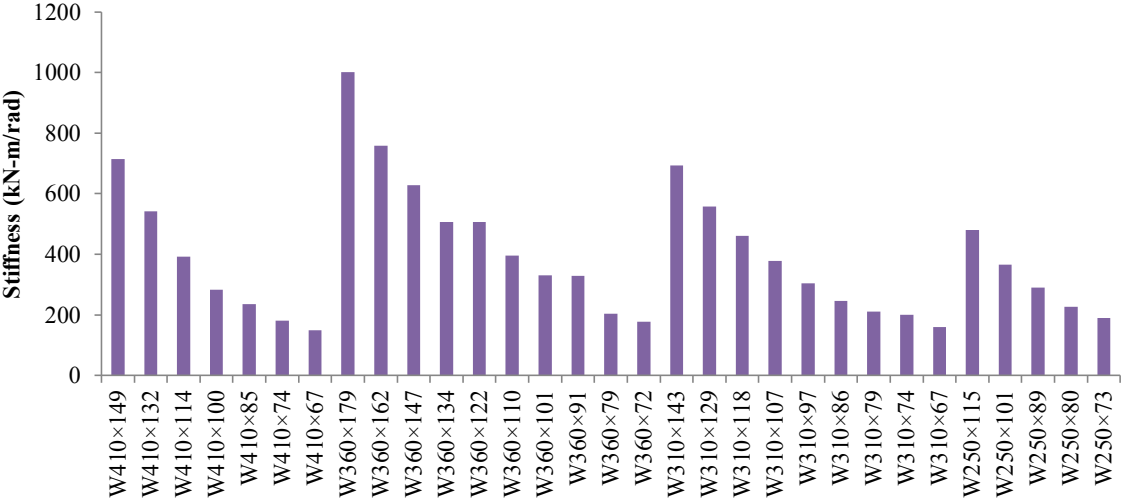


Figure 3.33. Elastic stiffness predicted by numerical analysis

### 3.4.2. Parametric comparisons

The parametric study showed that two distinct components—torsion of the flange and bending of the web—combine to provide the resisting moment to the rotation applied to the flange. However, their separate computation is complicated due to the inherent interaction. In order to simplify this task considerably, it is proposed that the torsional resistance be determined according to web bending only, by determining an effective length that indirectly accounts for both components. Since the two mechanisms share in resisting the applied load in accordance with their respective stiffnesses, this effective length will be function of the ratio of torsional stiffness of the flange to bending stiffness of the web. For bending of the web, Figure 3.34 shows an approximation of the bending condition using a beam analogy, and Equations [3-1] and [3-2] describe the elastic bending stiffness of the web. It was observed from the parametric study that the depth of the section had very little influence on the moment capacity, so it was eliminated from the equation along with the parameter  $E$  (considered constant for steel) and the constant 12. Since the effective length,  $b_{eff}$ , is the parameter ultimately to be determined, the only parameter considered to influence the web bending stiffness strongly is the web thickness and its influence is cubed, as indicated in Equation [3-3]. For the flange torsion, Equation [2-10] is rearranged to show the torsional stiffness in Equations [3-4] and [3-5], assuming a constant rate of change of twist. The length over which the twist takes place,  $L$ , is unknown and will be superseded by the effective length,  $b_{eff}$ , to be determined. Therefore, the most influential parameters for the flange contribution are captured in Equation [3-6], with the parameter  $G$ , considered constant for steel, and the constant 3 removed. Dividing the stiffness parameter in Equation [3-6] by that in Equation [3-3] gives a normalized stiffness ratio  $r_z$ , defined in Equation [3-7]. This ratio is similar to the reciprocal of the ratio  $r$  in Equation [2-4] given by Milner (1977), the only difference being that the depth of the section, which has been shown to have little influence on the torsional capacity, has been removed.

$$\frac{M}{\theta} \propto \frac{E \times I}{h} \quad [3-1]$$

$$\frac{M}{\theta} \propto \frac{E \times b_{eff} \times w^3}{12 \times h} \quad [3-2]$$

$$\frac{M}{\theta} \propto w^3 \quad [3-3]$$

$$\frac{M}{\theta} = \frac{GJ}{L} \quad [3-4]$$

$$\frac{M}{\theta} = \frac{G b t^3}{3L} \quad [3-5]$$

$$\frac{M}{\theta} \propto b t^3 \quad [3-6]$$

$$r_1 = \frac{b \times t^3}{w^3} \quad [3-7]$$

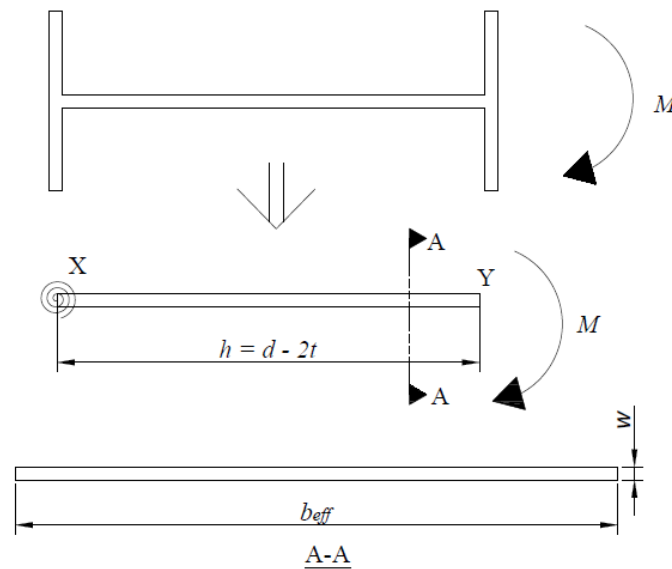


**Figure 3.34. Beam analogy for web bending**

Equation [3-8] is the proposed equation for determining the elastic torsional moment capacity of an unstiffened W-section member with the load applied through one flange. This equation utilizes only the web flexural behaviour, with the flange torsional behaviour to be incorporated into the term  $b_{eff}$ . The ratio  $r_1$  in Equation [3-7] represents the stiffness ratio for the two resisting components and can be used for the purpose of obtaining an appropriate effective length,  $b_{eff}$ , for use in design. Beyond the effective length of the web,  $b_{eff}$ , the moment capacity is proportional to the square of the web thickness,  $w$ . Equation [3-9], therefore, shows the geometric parameters (without any material properties) upon which the elastic moment capacity depends. The resulting variable,  $R$ , can be plotted to compare with the elastic moment capacity by normalizing both quantities to the associated maximum value obtained for all of the sections considered. This plot simply compares how  $R$  changes with the maximum moment from the numerical analysis to assess its proportionality

to the member capacity, and therefore its appropriateness as a proxy for the actual moment capacity for use in design. The fact that the trends for the two parameters are very similar implies that when using Equation [3-8] for design,  $r_l$  can be used to characterize the effective length,  $b_{eff}$ . Further discussions about the capacity and stiffness evaluations are presented in Chapter 5.

$$M = \frac{b_{eff} w^2}{6} F_y \tag{3-8}$$

$$R = \frac{b \times t^3}{w^3} \times w^2 = \frac{b \times t^3}{w} \tag{3-9}$$

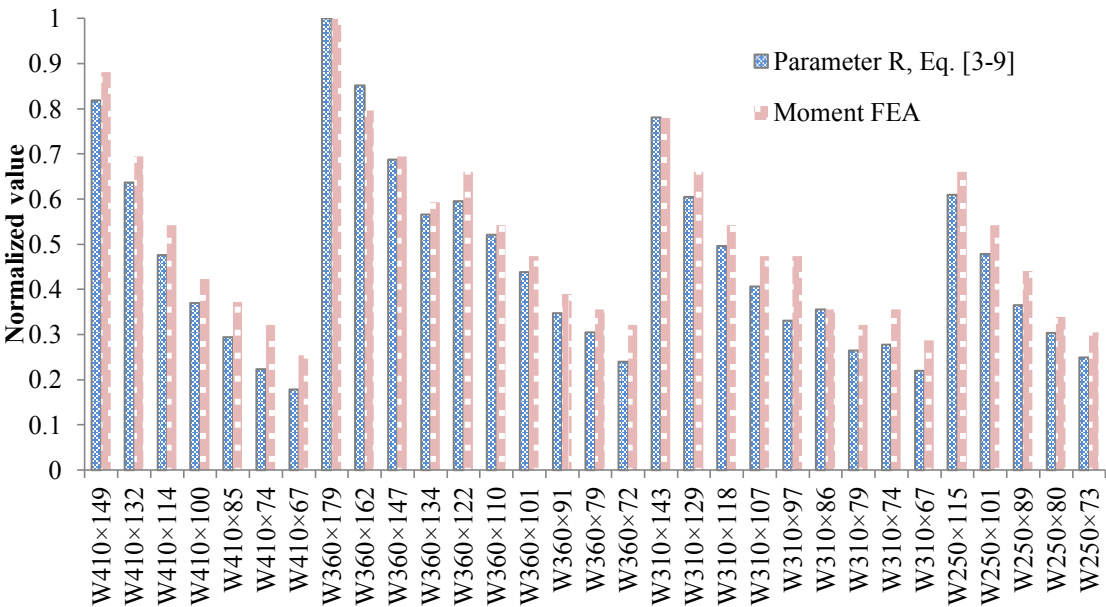


Figure 3.35. Parametric comparison with numerical analysis

## 4. Experimental Program

Unavailability of any experimental results on the unstiffened torsion of wide-flange sections dictated that a testing program was needed to give a better understanding and assurance in characterizing the behaviour of the member under this unique loading case. To have the results applied in an actual structure, it was also necessary that full-scale tests of the member with the surrounding assembly be executed. Wide-flange members conforming to dimensions and properties of as-built field conditions for a modular pipe rack system were tested. However, instead of typical sections used only for this type of structure, the program was expanded to including a variety of wide-flange sections with different cross-sectional dimensions. A total of nine tests were conducted, eight on unstiffened members and one on a member with stiffeners installed between the flanges. Details relating to the testing program, test results, and their comparisons with numerical analysis are described in the subsequent sections.

### 4.1. Test matrix

The main aim for the selection of the test matrix was to focus on sections for which the results could be interpreted for the entire general range of sections discussed in Section 3.4. Important parameters for unstiffened torsion are flange thickness, web thickness and flange width, as was revealed by the numerical analysis parametric study. Variation of the stiffness ratio of the flange to the web influences the moment capacity and stiffness. A higher flange-to-web stiffness ratio will have a longer influence zone for bending of the web if the length of the member is large (see Section 3.4.2), whereas if the length is small then the restoring torsional moment of the flange will be provided by the supports. The stiffness ratio parameter  $r_f$ , defined in Equation [3-7], was considered as the principal factor for the selection of the test specimens.

Figure 4.1 contains the W-section members included in the numerical analysis investigation, specifying the stiffness ratio given by Equation [3-7], normalized by the maximum value of  $r_f$  for all the sections. The range of this normalized ratio is about 0.5 to 1.0, which means that the stiffness ratio,  $r_f$ , varies by approximately 100% for the extreme cases. In order to include a broad range of behaviours in the testing program, sections with the maximum or minimum ratios in each depth group were initially selected. An additional W310 section with an intermediate stiffness ratio was added to the matrix, as this was considered to be the most commonly-used section for the modular pipe rack system that was the primary impetus for this research. Since the two W250 sections had

ratios in close proximity to one another, one was dropped from the matrix. In Figure 4.1, the red bars indicate the sections used for the test specimens.

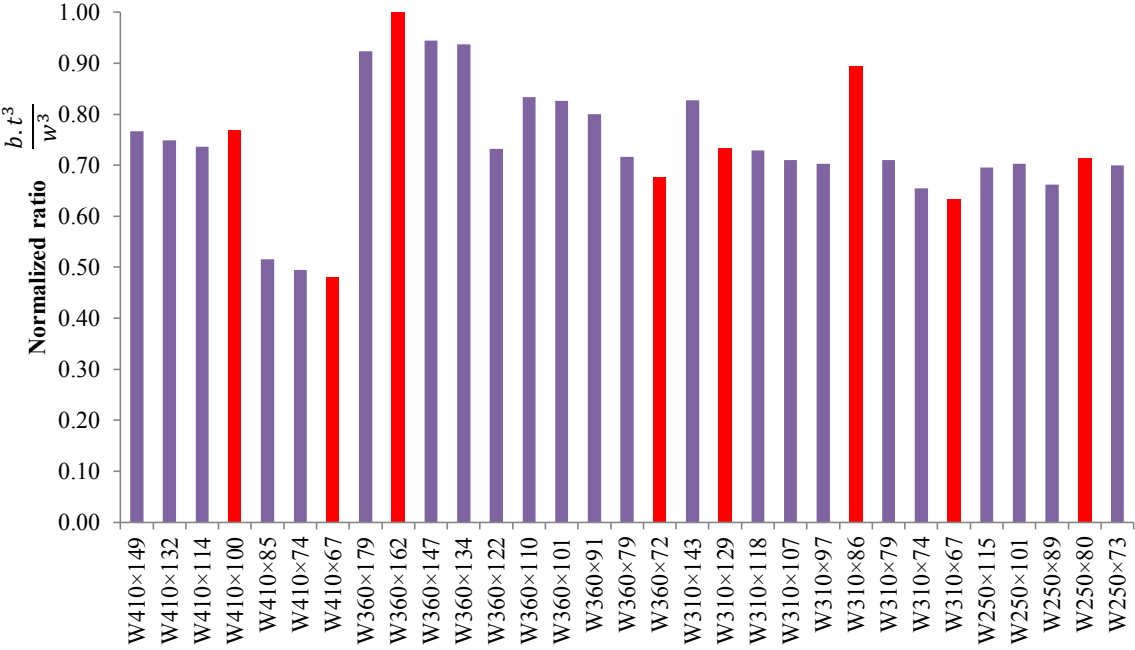


**Figure 4.1. Normalized ratio of flange-to-web stiffness**

A ninth specimen was added to the matrix (W310x129), which created a duplicate pair, except with one having stiffeners installed between the flanges. This specimen was added to provide a direct comparison with the unstiffened W310x129 member. The final test matrix is shown in Table 4.1. Sections in the matrix had a wide variety of cross-sectional dimensions, nominal values of which are shown in Figure 4.2.

Table 4.1. Test matrix

Specimen Designation	Section
SP1	W360×162
SP2	W310×86
SP3	W410×100
SP4	W250×80
SP5	W360×72
SP6	W310×67
SP7	W410×67
SP8	W310×129
SP9	W310×129-Stiffened

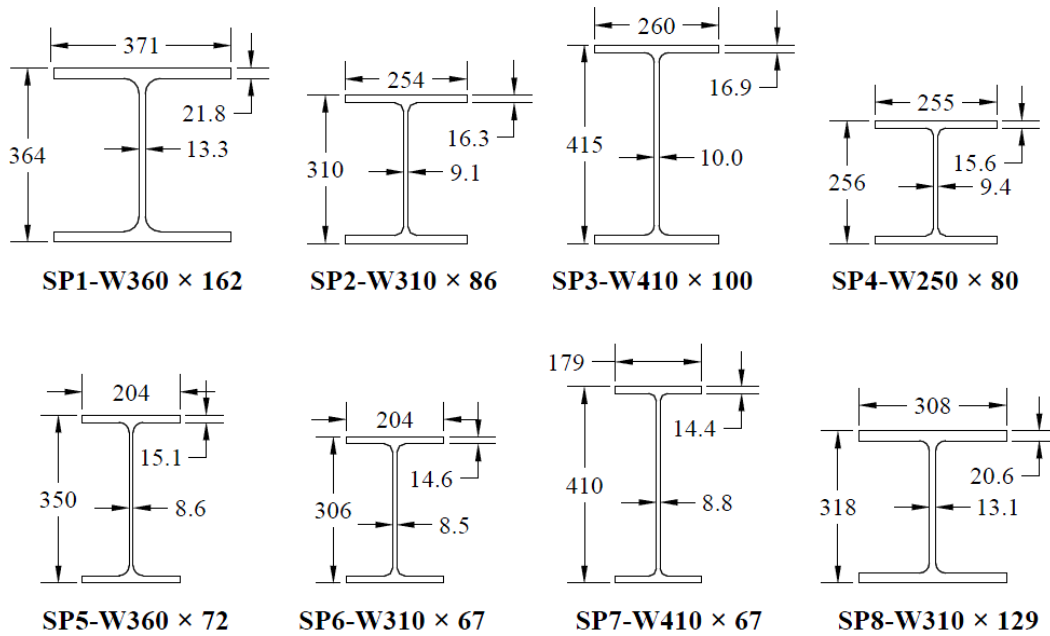
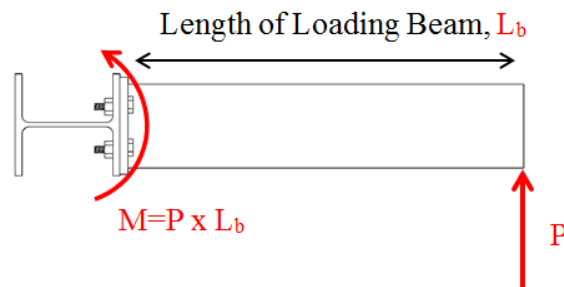


Figure 4.2. Nominal dimensions of tested sections  
(SP9 same as SP8, but with added stiffeners)

## 4.2. Test setup

The test setup was designed to facilitate the full-scale torsion testing of the wide-flange members. The test setup's ability to provide the necessary force reactions and stiffness was kept as the governing design parameter. The main objective was to obtain the moment–rotation curves and a correct estimation of ultimate elastic capacity of the member under torsional loading. Torsional loading had to be applied as it is applied in a real structure, so a typical connection assembly was used to apply the load to the flange of the columns.

Loading was applied on the cantilever end of the beam, which is converted to a torsional moment at the flange of the connected member, as illustrated schematically in Figure 4.3. The length of the beam was selected such that the available stroke of the jack was sufficient to push the beam well beyond the elastic limit, while keeping the shear force applied to the test specimen relatively low in order to reduce its influence on the moment-rotation results.



**Figure 4.3. Schematic loading diagram**

A three-dimensional diagram of the test setup is shown in Figure 4.4, and top and side views are depicted in Figures 4.5 and 4.6, respectively. The loading jack, which had a stroke of 400 mm (16 in.), was supported by a distributing beam, which in turn got its reaction support from a stiff pair of shear walls. The loading beam was a W310×86 section, which was kept the same for all the tests. The test specimen member (shown red in Figures 4.4 to 4.6) was supported at the ends by strong columns, connected by pre-tensioned 25 mm (1 in.) diameter ASTM A325 bolts. The specimen was only connected to the flanges of the strong columns, which were 25 mm thick but

unstiffened. The strong columns were bolted to the floor by pre-tensioned rods to have adequate stiffness and resistance to overturning. Installation of the specimen within the test setup was carried out by adjusting the locations of the strong columns to the exact length of the specimen member so that it would not be subject to unintentional forces when the connecting bolts were pre-tensioned.

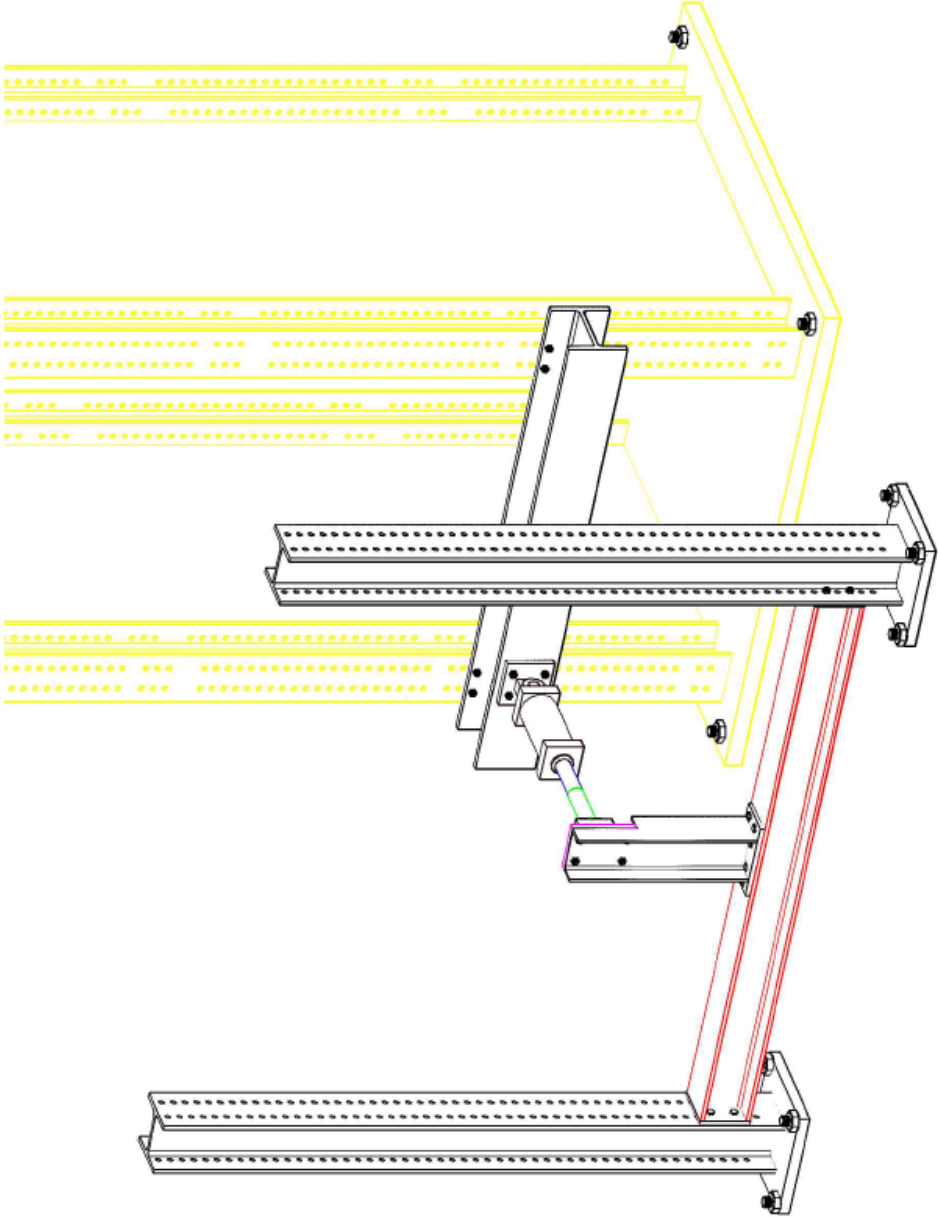


Figure 4.4. Test setup—3D view

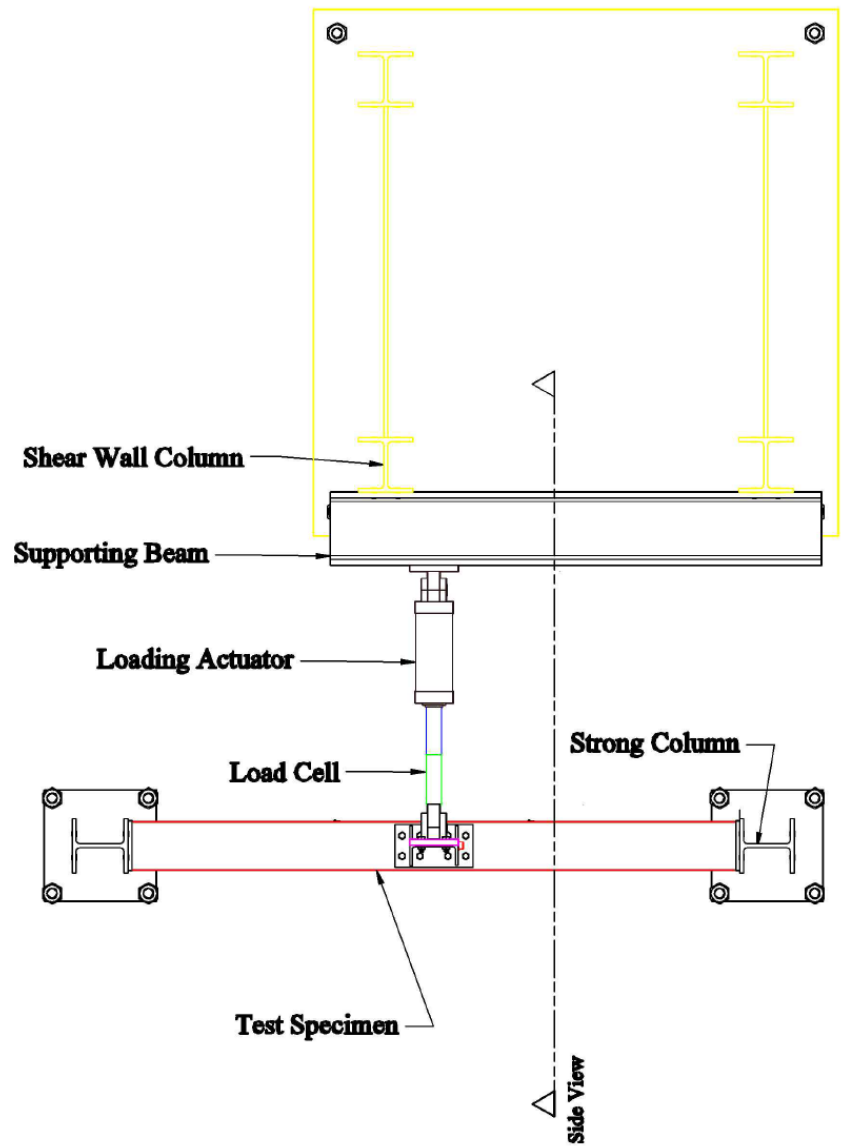
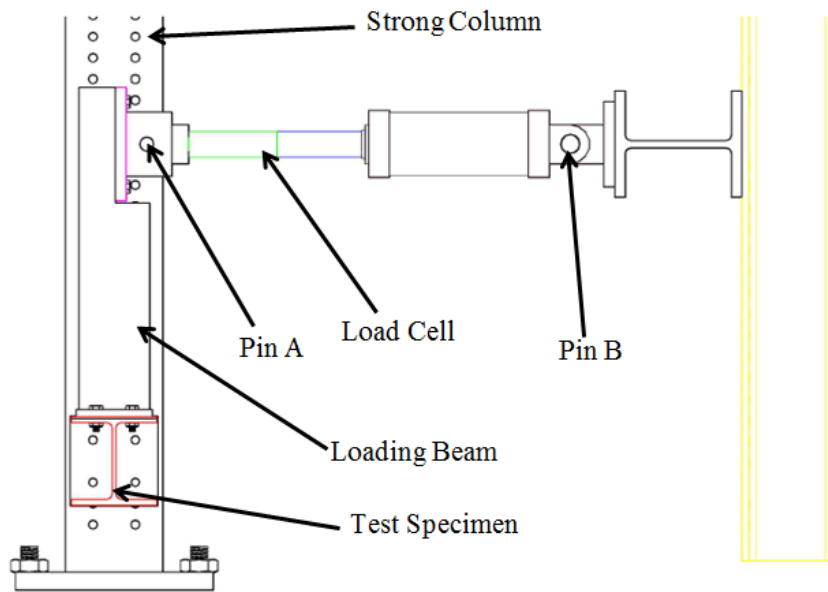


Figure 4.5. Top view of test setup



**Figure 4.6. Side view of test setup**

The procedure for swapping specimens between tests is as follows. Pin A from the actuator was taken out and the loading jack was removed from the loading beam connection with the aid of a chain hoist. The connection of the loading beam to the specimen was then unbolted and the beam was removed. The tested specimen was then unbolted from the strong columns and removed from the test setup. The floor bolts were loosened on one of the strong columns to fix the new specimen within the strong column supports, after which the connection bolts between the strong column and specimen were snugged and pre-tensioned. Subsequently, the floor bolts anchoring the repositioned strong column were pre-tensioned. Finally, the beam was attached to the new specimen and the jack was lowered into the pin assembly and connected to the beam.

### **4.3. Test Specimens**

Figure 4.7 shows a typical drawing of a test specimen without stiffeners, and drawings for all of the specimens can be found in Appendix A. The test specimens consisted of a 3.87 m long member with end plates of 25 mm thickness for connection to the strong columns. The plate was welded to the member with an 8 mm fillet weld all around for the unstiffened members and a 10 mm fillet weld for the stiffened specimen, as loads expected for the unstiffened members were significantly lower than that for the stiffened member. Standard holes were drilled in the end plates to accommodate 25 mm (1 in.) diameter bolts. Positioning of these holes was decided based on the

strong column hole profile (76 mm (3 in.) spacing and 152 mm (6 in.) gauge). Holes in the specimen member for its connection with the loading beam were drilled with the dimensions shown in Figure 1.3.

For the stiffened member, 19 mm (3/4 in.) thick fitted stiffeners were welded between the flanges. The size of the welds between the stiffeners and the loaded flange was increased over that of the other stiffener welds, as loads from the beam were transferred directly through this flange and large transfer forces were expected on the tension side.

To enable the connection of the loading beam with the actuator, the flanges of the beam were blocked flush with the web, as can be seen in Figure 4.6. Four holes were drilled in the web for the connection with the jack. The bolt diameter used in the connection was 38 mm (1.5 in.) and the bolts were pretensioned with the pin and clevis assembly of the jack. Detailed geometric dimensions of the beam are given in Appendix A.

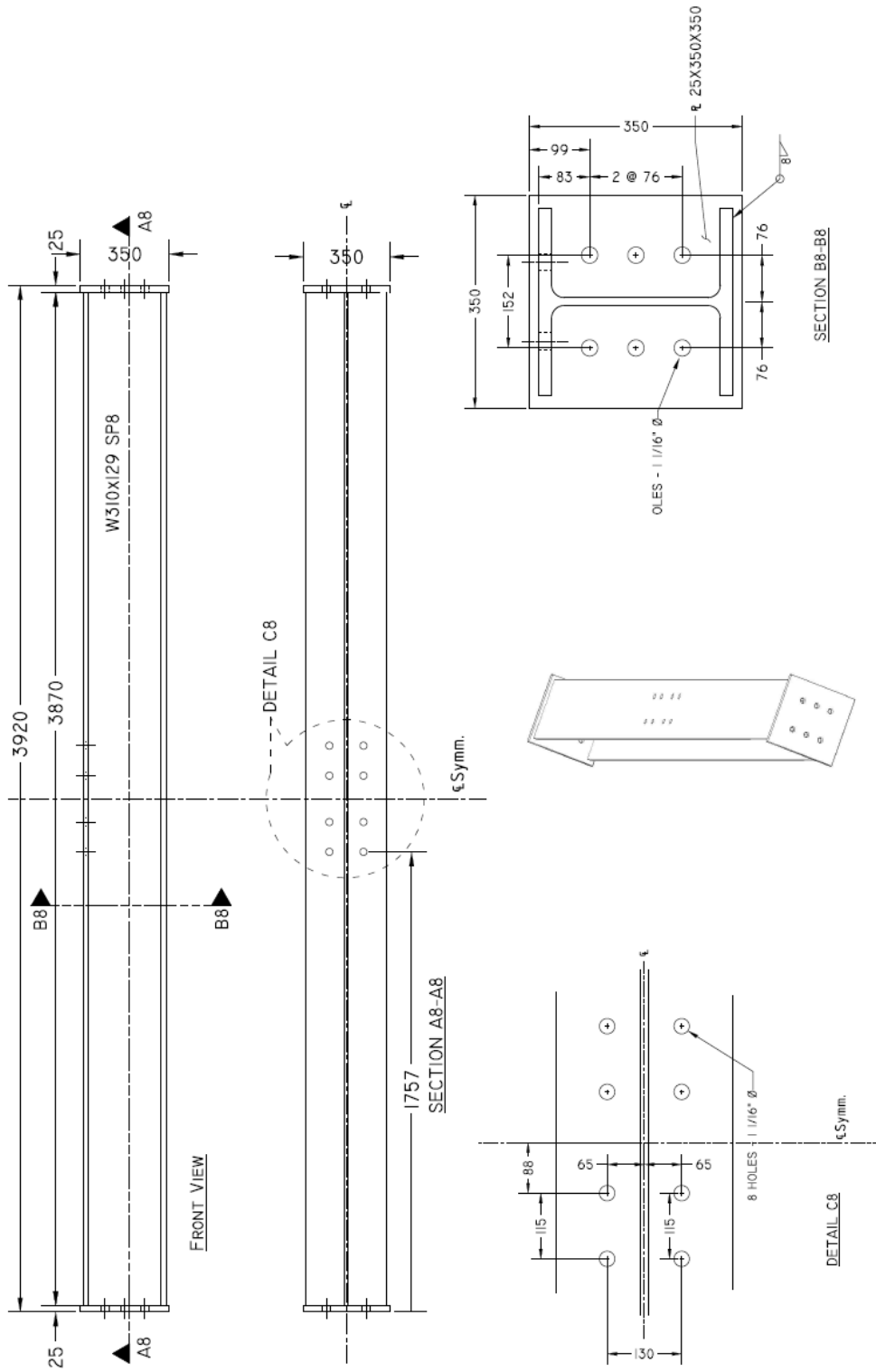


Figure 4.7. Fabrication drawing of test specimen SP8

#### 4.4. Instrumentation

Diagrams of the applied force components are shown in Figure 4.8, where the torsional moment applied to the specimen,  $M$ , is the net effect of three forces parallel (purple) and three perpendicular (yellow) to the axis of the beam, which is rotated at an angle  $\theta_b$ . The self-weight end reaction of the actuator,  $W$ , was measured accurately by attaching a load cell to the end to be connected to the beam, and supporting it with the laboratory crane. All other forces and displacements could be determined by the load cell measuring the actuator force,  $P$ , and the instrumentation for the measurement of displacements and rotations shown in Figure 4.9.

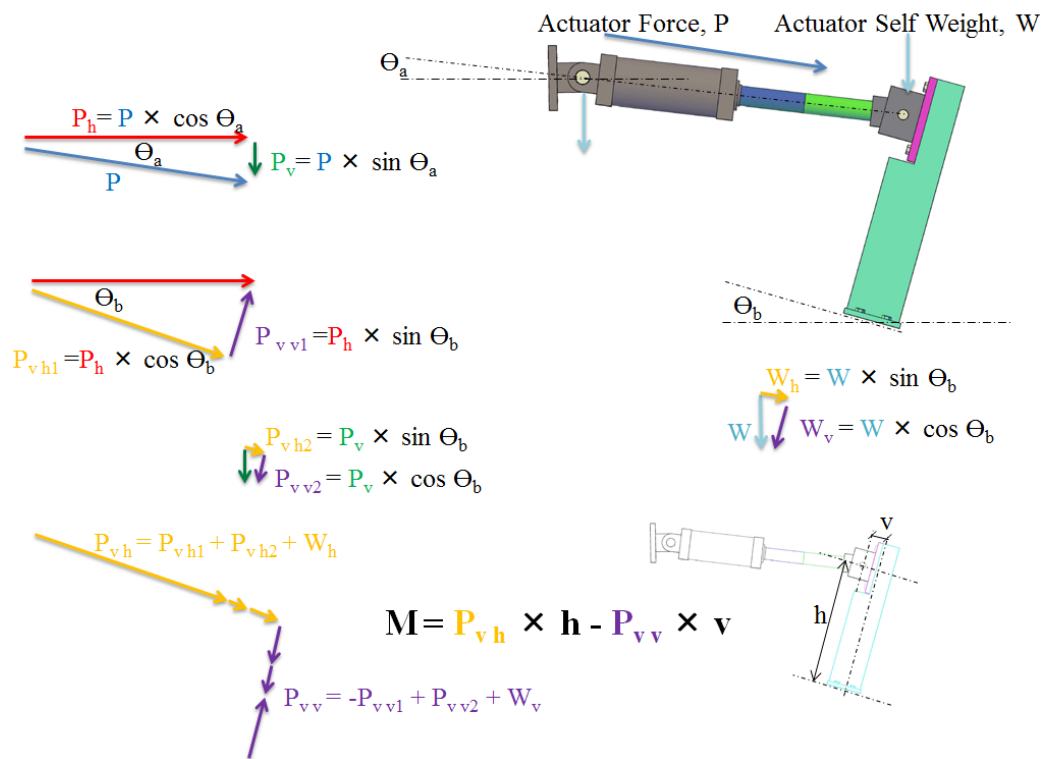


Figure 4.8. Diagram showing the breakdown of forces

Four inclinometers were used to measure the rotations of the top flange of the specimen, attached in the pattern shown in Figure 4.9. This pattern was adopted on one side of the member centreline only due to the symmetry of the test setup, although a clinometer was placed under each flange of the beam (CL-2 and CL-6) for an accurate measurement of the flange rotation in this region. One

inclinometer (CL-5) was attached to the bottom flange to measure the overall rotation of the cross-section at the specimen midspan. Two other inclinometers (CL-3 and CL-4) were attached to obtain the twist profile of the flange under torsion. While the actuator force was measured by a load cell in series with the piston, due to the importance of this parameter a redundant measurement was also recorded from a pressure transducer installed within the hydraulic line. The load cell was calibrated immediately before installation into test setup.  $\Theta_b$  in Figure 4.8 is given by CL-2 and CL-6, whereas CL-1 was used to measure  $\Theta_a$ .

Inclinometer : CL

Cable Transducer : CT

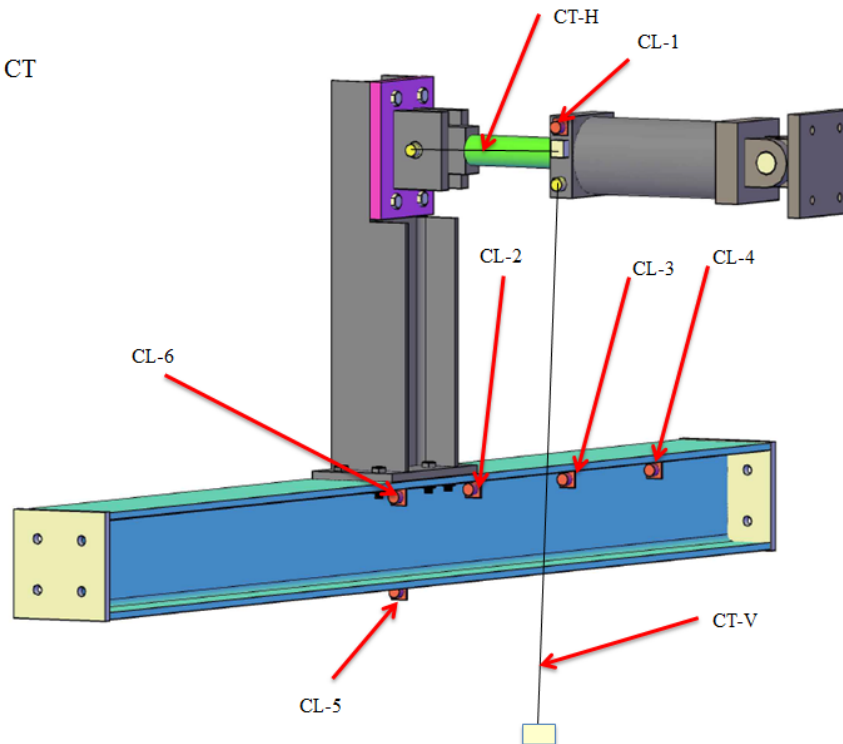


**Figure 4.9. Primary instrumentation to measure displacements and rotations**

Strain gauges on the web of the specimen were mounted at the locations shown in Figure 4.10. The gauges closer to the specimen centreline were spaced closer together as the stresses due to the applied torsion were expected to be higher in that region. The strain gauges were attached as close as possible to the fillet as the numerical model showed that yielding started at the junction of the web and flange. Symmetry was also utilized in placing the strain gauges and they were installed on only one side of the connection.

Initially it was planned that the white-washed surface of the web would indicate the onset of yielding. However, during the first test this method was not found helpful to clearly pin-point the yielding strain of the web. This was due to the fact that yielding was very localized and occurred in very close proximity to the fillet. As such, the elastic limit of the W360×162 member was not determined accurately in the first test. Nonetheless, the moment capacity at the onset of web yielding was clearly defined using the strain gauge data for the rest of unstiffened test specimens.

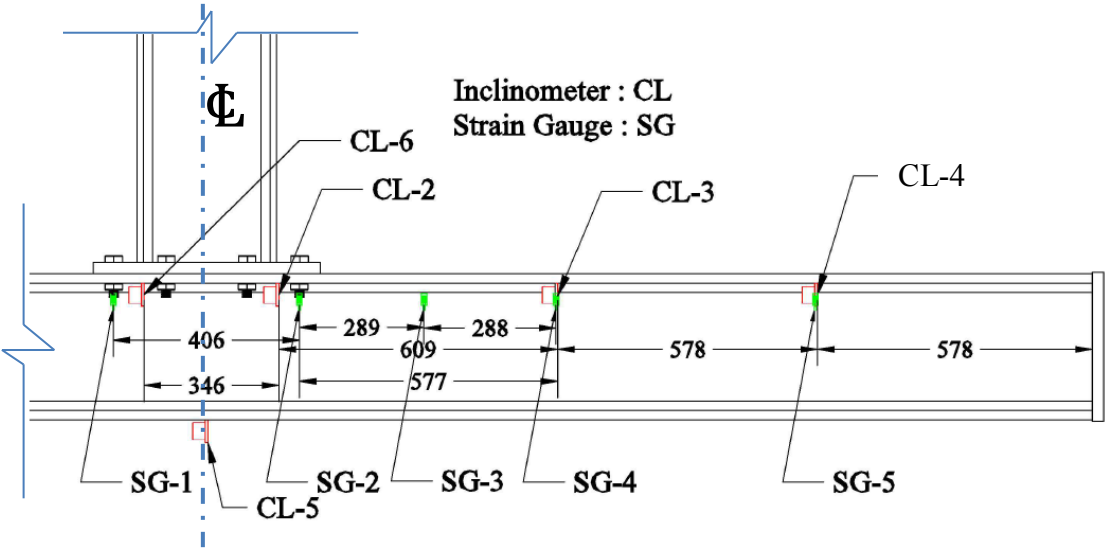


**Figure 4.10. Instrumentation profile**

Apart from the instrumentation discussed above, other redundant measurements were also taken, although they did not participate directly in the calculation of the moment or rotation; rather, they were used to ensure that the test setup was behaving in accordance with the intended design. A set of two LVDTs on each end of the specimen measured any slip rotation between the test specimen and the strong column, although during all the tests no appreciable slip was noted. One cable transducer was attached on each strong column to see if any significant movement was detected in the direction in which the actuator push was applied, but no significant movement was observed. An overall view of the instrumentation used is shown in Figure 4.11.

For the stiffened specimen, the force applied was comparatively larger than those applied to the unstiffened specimens and displacement of the specimen centreline was expected in that direction. Accordingly, a cable transducer was attached at the centre of the specimen (along the length and the depth) to measure this movement in the direction of the applied force. This deflection increased

gradually throughout the test to a maximum value of 20.8 mm (L/186) at a flange rotation of 200 mrad.



**Figure 4.11. Test specimen in place with instrumentation before the test**

#### **4.5. Ancillary tests**

All steel material was designated as CSA G40.21 Grade 350W. To determine the material properties, tension coupons were taken with the dimensions and positions shown in Figure 4.12. The lengths from which these coupons were taken were cut from the same pieces as the specimens themselves. Coupons were taken from the web and flanges: one from each flange and two from the web.

Coupons and testing procedures conformed to the general requirements of ASTM Standard A370. Most coupons had a thickness under the limit for “sheet-type” coupons; however, some of the coupons were slightly greater than the 19.5 mm thickness limit. For the sake of uniformity and simplification, the dimensions shown in Figure 4.12 were used for all coupons.

Coupons were tested in an MTS universal testing machine and the elastic and plastic properties were noted. Static yield stress measurements were taken and averaged for use in interpreting the torsion test results. A summary of the coupon test results is presented in Table 4.2. Coupons were

designated to include the specimen number. For instance, in “C1-4”, 1 means that this coupon corresponds to specimen SP1 and the 2<sup>nd</sup> numeral stands for location from which it has been taken (1&2 for the web and 3&4 for the flanges). Coupon cut-out drawings and stress–strain diagrams are given in Appendix B.

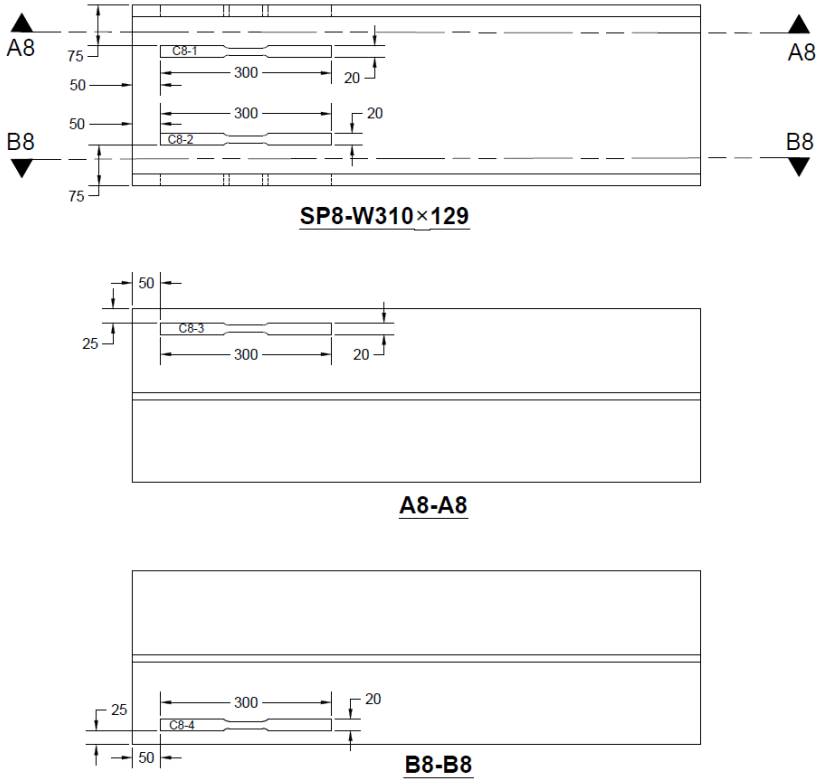


**Figure 4.12. Tension coupon cut-out locations**

## 4.6. Test results

Similar readings from inclinometers CL-2 and CL-6 suggested that the expected symmetry was achieved: the values in all experiments never differed by more than 5%. Similar results were also observed in the strain data recorded by gauges SG-1 and SG-2. Measurements of the slip between the specimen end and the strong column revealed that the end rotation never exceeded 2 mrad by the terminal point of the test or 0.15 mrad at the elastic limit, which is very small and was therefore neglected. Experimental moment–rotation response curves are given for all the test specimens in Figures 4.13 to 4.21, wherein the same scale is used to facilitate comparisons of stiffness and strength.

**Table 4.2. Coupon test results**

Specimen	Coupon Designation	Yield Stress (MPa)		Tensile Stress (MPa)		Young's Modulus (GPa)		Elongation (%)	Area Reduction (%)
		Individual	Mean	Individual	Mean	Individual	Mean	Mean	Mean
SP1- W360x162	C1-1	372.3	376.4	471.4	472.7	176.5	189.5	41.7	66.7
	C1-2	380.5		473.9		187.4			
	C1-3	376.8	373.5	471.5	470.3	196.6			
	C1-4	370.2		469.1		197.7			
SP2- W310x86	C2-1	354.7	351.8	443.1	442.2	190.1	193.9	38.6	62.8
	C2-2	348.8		441.3		187.8			
	C2-3	340.7	338.2	450.2	448.3	192.0			
	C2-4	335.7		446.5		205.8			
SP3- W410x100	C3-1	345.5	347.7	439.1	440.1	190.2	190.1	41.1	62.8
	C3-2	349.9		441.0		190.2			
	C3-3	327.8	326.3	444.9	440.3	196.0			
	C3-4	324.8		435.7		184.0			
SP4-W250x80	C4-1	333.3	330.1	429.6	444.9	195.2	195.2	40.2	61.8
	C4-2	326.9		460.1		196.9			
	C4-3	306.9	305.9	423.7	418.4	196.1			
	C4-4	305.0		413.1		192.5			
SP5- W360x72	C5-1	363.0	363.9	480.0	466.0	198.1	195.7	40.7	62.4
	C5-2	364.8		451.9		193.4			
	C5-3	346.1	340.4	450.2	448.9	195.6			
	C5-4	334.8		447.6		195.7			
SP6- W310x67	C6-1	375.0	378.5	462.9	466.3	191.2	198.9	38.3	59.6
	C6-2	382.0		469.7		201.1			
	C6-3	349.6	346.4	468.3	450.1	203.1			

	C6-4	343.2		431.9		200.3			
SP7- W410x67	C7-1	376.0	370.2	450.0	443.9	196.1	199.3	39.7	60.2
	C7-2	364.5		437.8		192.8			
	C7-3	333.5	335.4	398.9	416.9	216.2			
	C7-4	337.3		434.8		192.2			
SP8- W310x129	C8-1	362.5	358.6	417.4	432.6	206.4	203.7	42.6	64.1
	C8-2	354.7		447.9		200.8			
	C8-3	351.9	346.3	448.4	447.7	204.4			
	C8-4	340.7		446.9		203.1			
SP9- W310x129	C9-1	358.9	358.7	448.6	449.5	201.8	199.9	41.9	63.5
	C9-2	358.4		450.3		199.5			
	C9-3	336.2	343.8	437.9	442.8	197.7			
	C9-4	351.4		447.7		200.6			

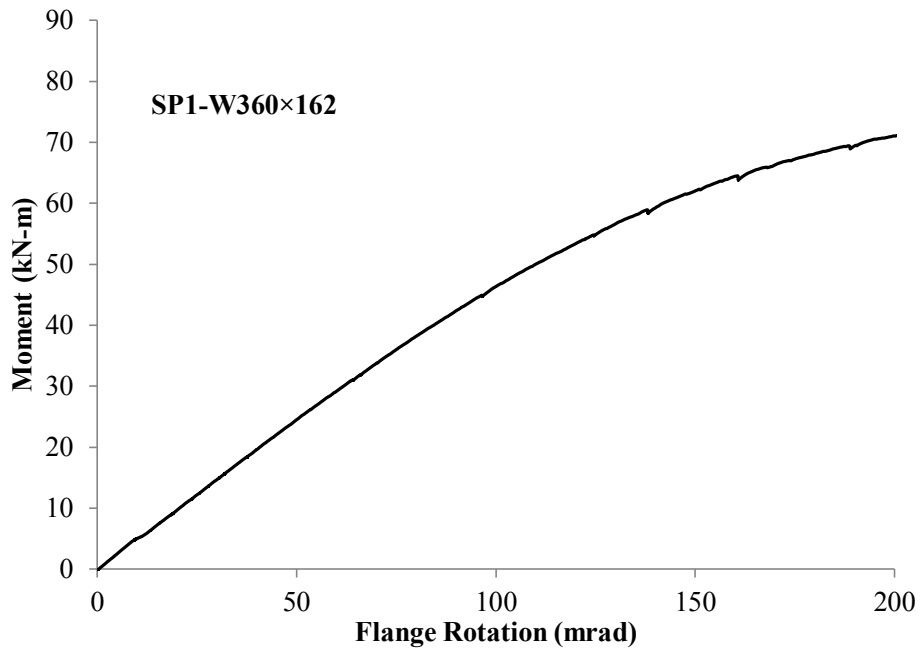


Figure 4.13. Test result SP1-W360x162

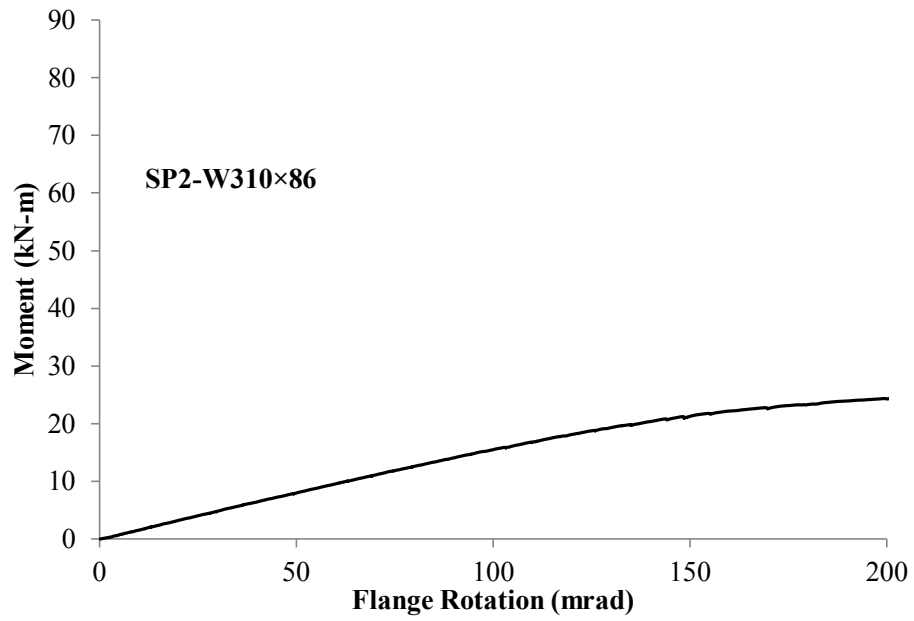


Figure 4.14. Test result SP2-W310×86

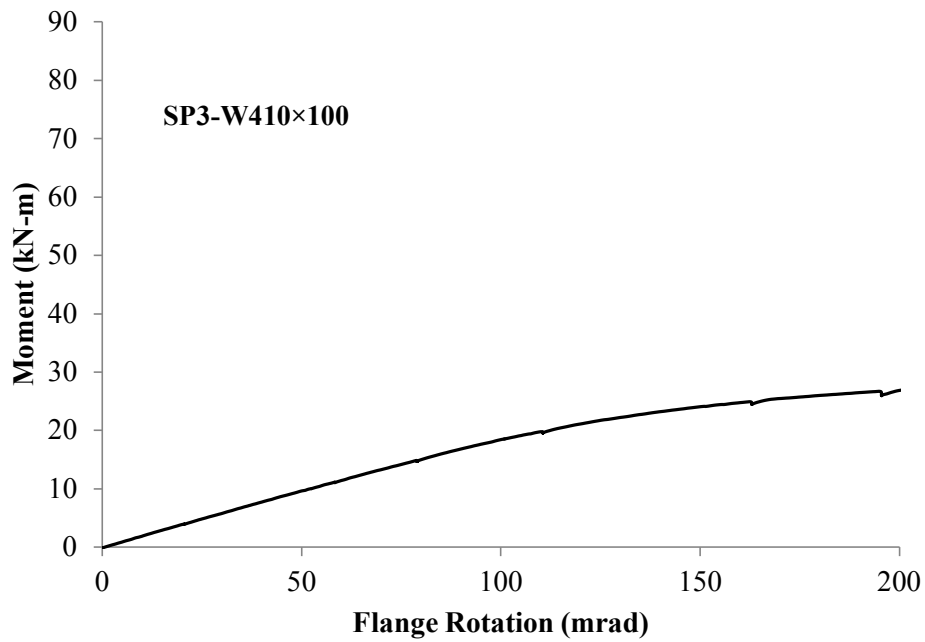


Figure 4.15. Test result SP3-W410×100

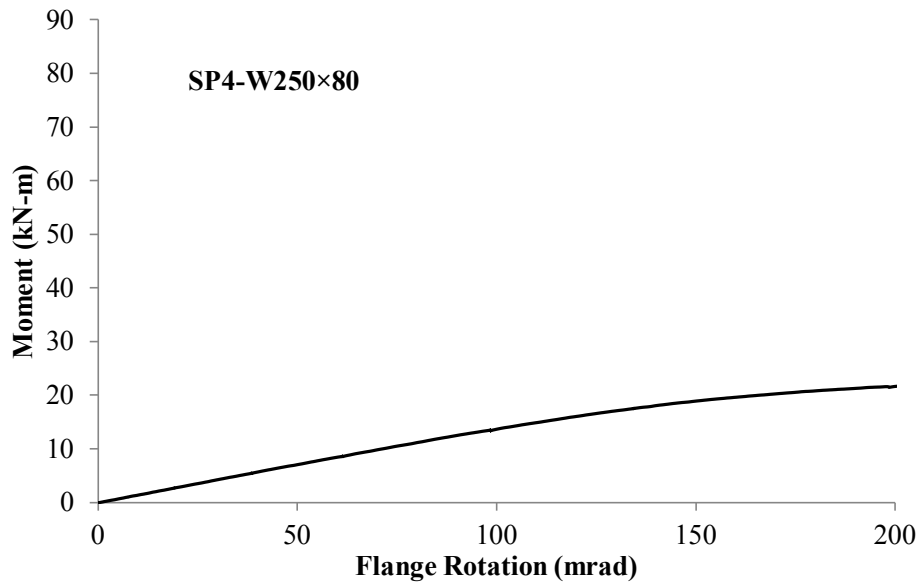


Figure 4.16. Test result SP4-W250x80

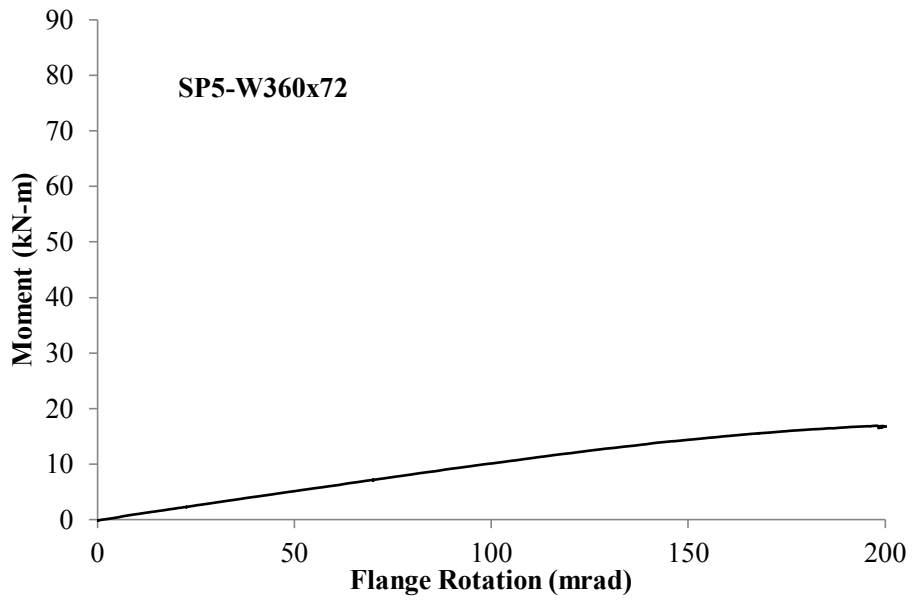


Figure 4.17. Test result SP5-W360x72

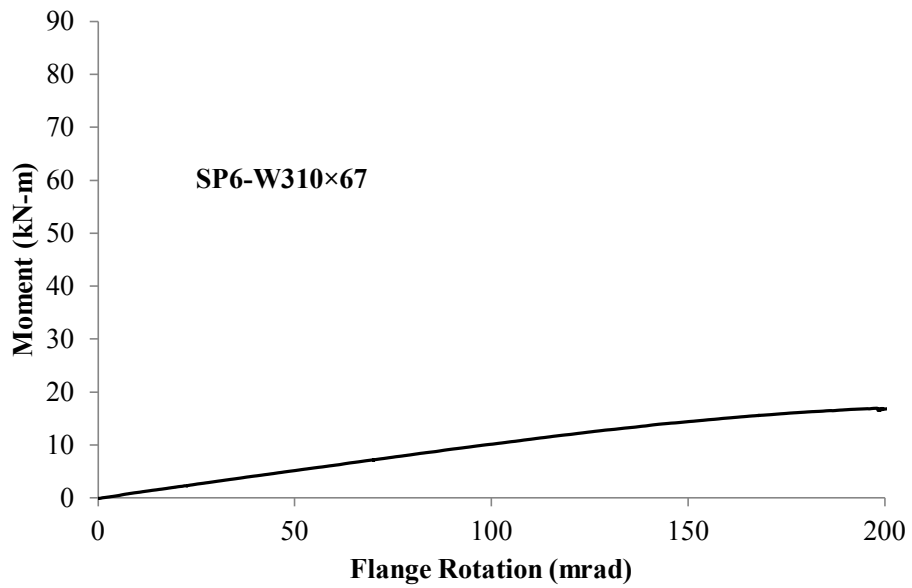


Figure 4.18. Test result SP6-W310x67

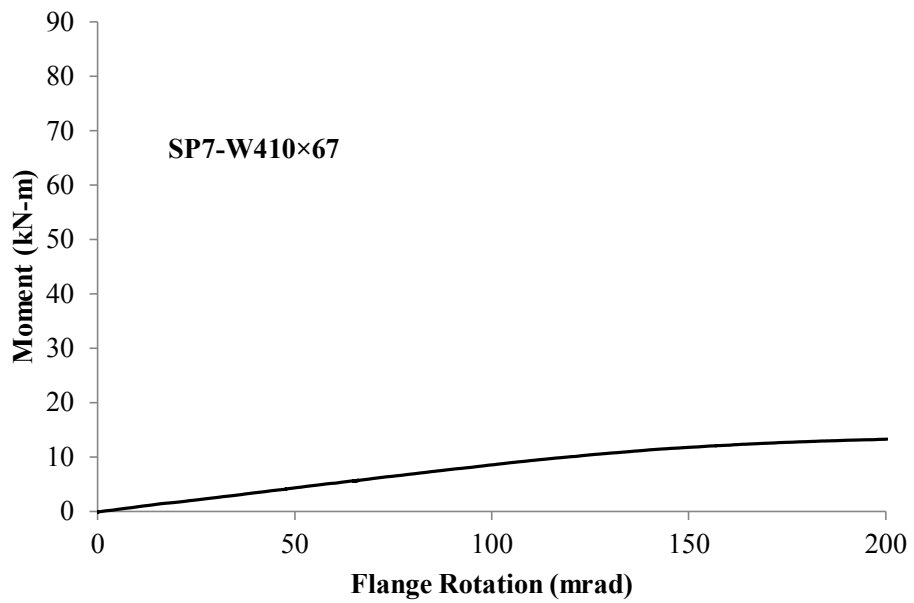
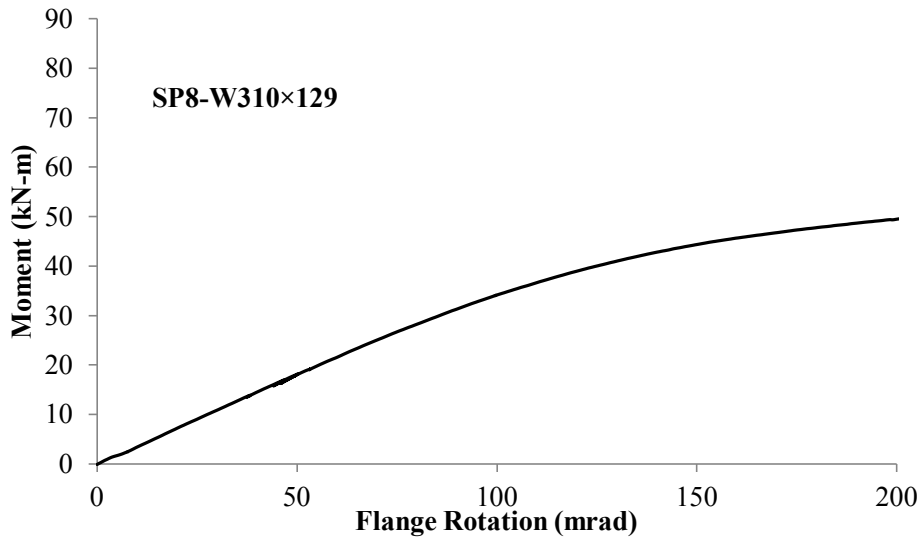
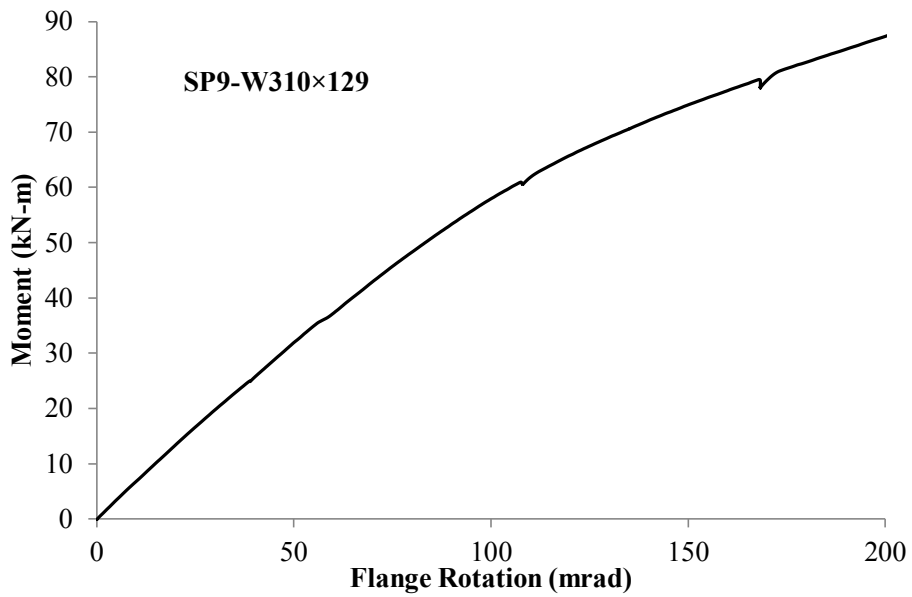


Figure 4.19. Test result SP7-W410x67



**Figure 4.20. Test result SP8-W310x129**



**Figure 4.21. Test result SP9-W310x129**

Although the strong columns provided fixity against rotation at the specimen ends, warping was not completely fixed at the supports; i.e., the thickness of the end plates of the specimens and the

connection with the strong column were not selected to fulfill the criteria for the warping-prevented boundary condition. In fact, the test results suggested that the supports behaved more like the warping-permitted case, and this was most prominent for stiffened specimen SP9. If warping were prevented then at the supports the material would be expected to yield first at the flange tips, as predicted by classical torsional theory, whereas if warping were to be unrestrained it would yield first midway along the flange width. Mill scale flaking along the flange centreline suggested that the supports permitted significant warping. No signs of yielding were observed along the tips of the flanges of the member, even by the end of the tests.

End plates of the specimens were attached to the strong column by pre-tensioned bolts, which initially eliminated any gaps between the parts. However, after the tests a clear gap between the strong column flange and the end plate was noted, due mainly to end plate deformations. From the numerical model of specimen SP9, which imposed the most demand at the supports, it was observed that only about 3.5 mm of longitudinal movement at the flange tips would occur when warping deformations are completely unrestrained. Figure 4.22 shows that a gap of 2.18 mm was observed after the test, excluding any recovered elastic deformations in the plate and the strong columns. The degree of warping restraint provided at the specimen ends is discussed further in the next section.



**Figure 4.22. Post-test gap between end plate and strong column (SP9)**

## 4.7. Numerical analysis comparisons

Comparisons of the test results with the numerical analyses are shown in Figures 4.23 to 4.31, where the dots on the numerical curves indicate the onset of yielding of the cross-section at the surface of the web adjacent to the loaded flange. While the numerical studies conducted before the tests (Chapter 3) used the nominal material and geometric properties, the actual static yield stress and modulus of elasticity from the coupon tests were introduced for comparisons with the test results. The mean yield stress of the two web coupons was used for the whole model as yielding of the web was considered the limit state that needed to be identified clearly, and further refinement for the flanges was deemed unnecessary. The modulus of elasticity is the mean value for all four coupons from the specimen. Test specimens are also subject to mill rolling tolerances, and the measured thicknesses for the coupons are given in Appendix B. For example, for SP1-W360x162, one flange was 1 mm thinner than the nominal value and the other was 2 mm thinner. Small variations from the nominal web thicknesses were also observed, which can be a reason for differences in the stiffness response during the tests. In numerical modelling, it can be challenging to introduce such small localized variations; hence, nominal geometric properties have been used.

The numerical analyses are based on a simplified loading model, as discussed in Chapter 3. Simplified loading made it feasible to increase the number of elements for the initial studies without increasing the computational effort required, providing good results; however, full optimization was not achieved due to the large overall size of the assemblies being modelled and the long resulting run times. For comparisons with the results of the eight unstiffened specimen tests, a finer mesh was used. Therefore, the stiffness and moment capacity in Figure 4.30 are somewhat less than those shown in Figure 3.25, although the sections are the same. However, in both cases the stiffness is decreased as the boundary conditions are changed from warping-restrained to warping-permitted. The numerical analysis results from the models where warping is permitted at the ends are generally closer to the test results.

Table 4.2 shows the initial web yield moment given by the numerical models compared with those determined from the strain gauges on the webs during the tests. The initial yield moment from the numerical analysis has been extracted using the warping-permitted boundary condition—as the warping restraint condition has very little effect on the yield moment—and the PEEQ parameter to determine the yield point. In this case, fully-optimised meshing was used but since the analysis was so computationally expensive only the elastic limit shown in Table 4.2 was obtained rather than the

entire response curve. The differences in the slopes of the elastic curves were very small, but the refinement did have some influence on the initial web yield moment.

Coupon test results showed that the uniaxial yield strain for the steel in the specimen webs varied from about 0.0017 to 0.0020. This strain is taken as the mean measured static yield stress divided by the mean measured modulus of elasticity. Strain readings from gauges SG-1 and SG-2 were averaged to get the initial yield values for the test specimens, assuming uniaxial straining without significant initial residual stresses. In Table 4.2, the initial yield moment values obtained from the tests are slightly lower than those obtained by numerical analysis. However, the actual onset of yielding is influenced by the presence of tensile residual stresses at the web-to-flange junction aligned with the axis of the member. Residual stresses were not measured for the test specimens and have been neglected, as in this plane stress situation one side of the web would yield at a higher bending stress and the other at a lower bending stress than the yield stress determined from the uniaxial tension coupon tests. The agreement between the initial yield moments obtained from the refined numerical analyses and those from the tests is considered acceptable.

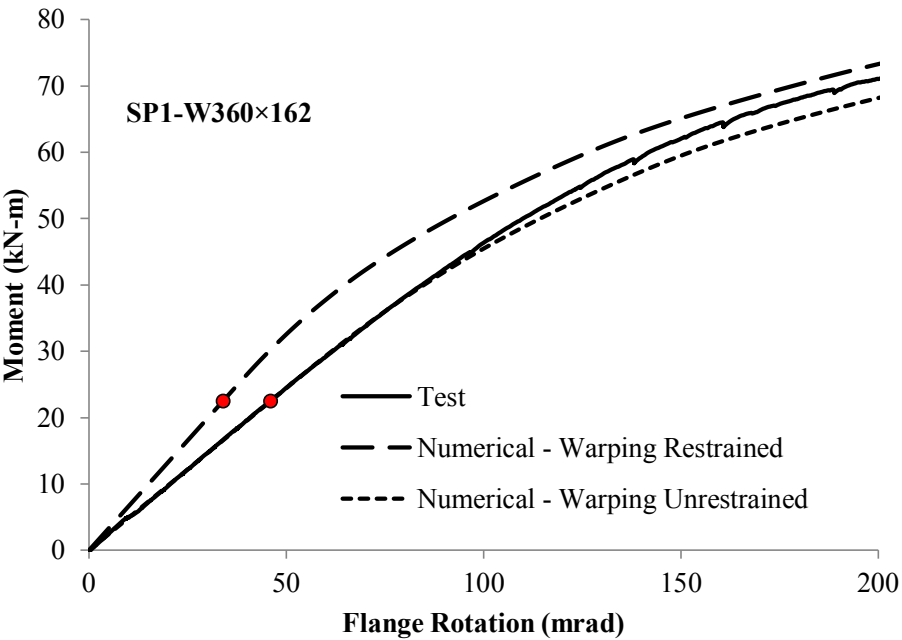
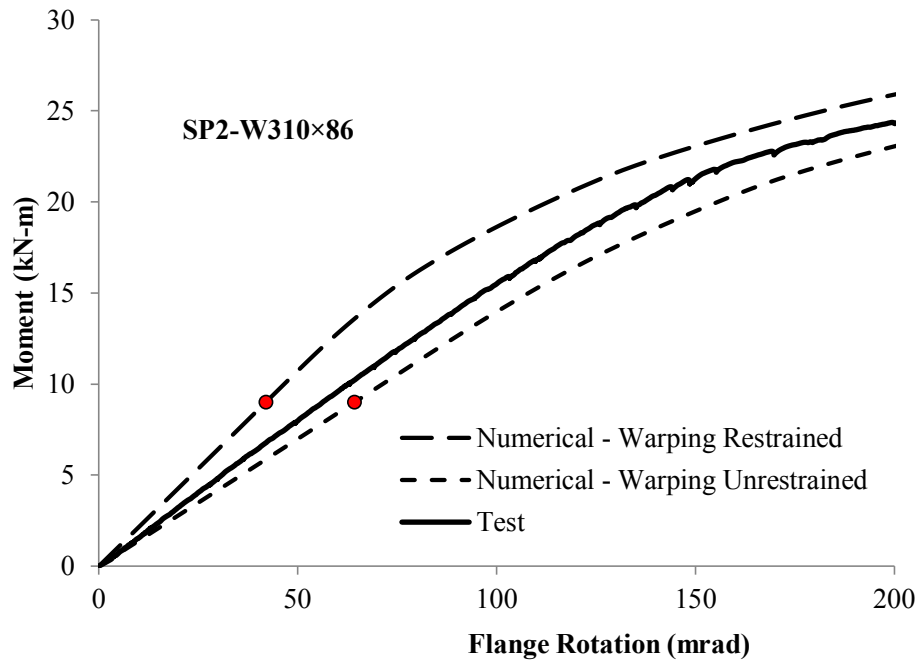
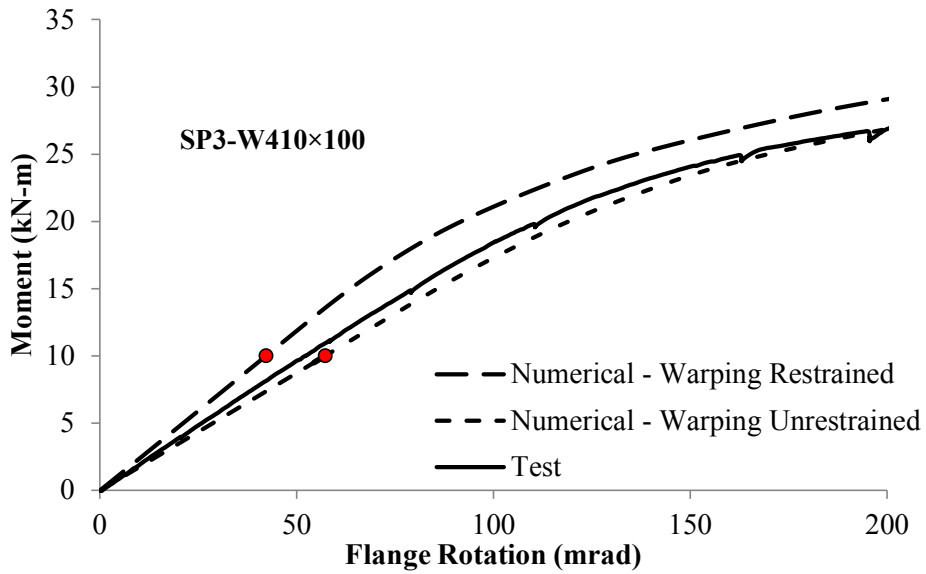


Figure 4.23. Test result SP1-W360x162 compared with numerical results



**Figure 4.24. Test result SP2-W310×86 compared with numerical results**



**Figure 4.25. Test result SP3-W410×100 compared with numerical results**

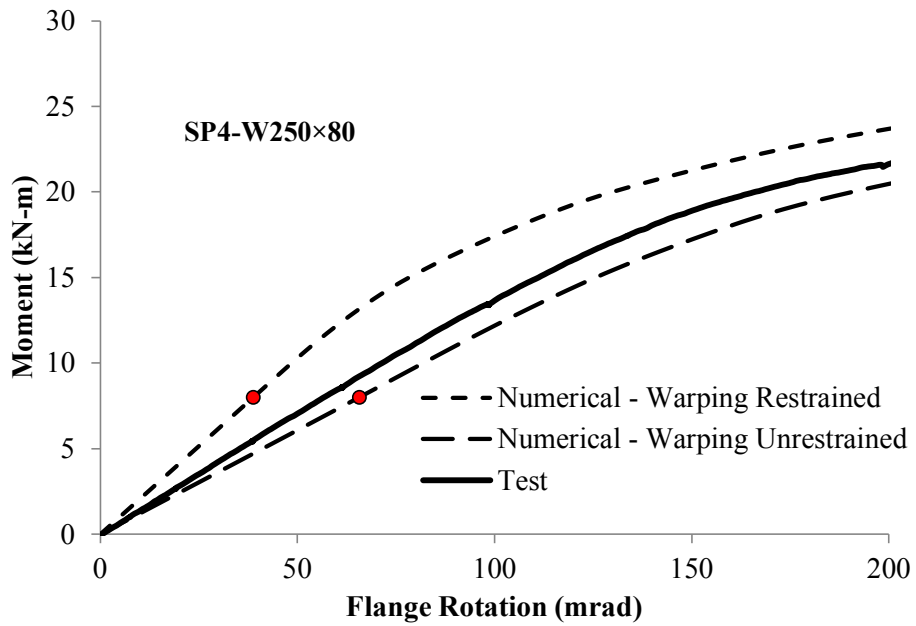


**Figure 4.26. Test result SP4-W250×80 compared with numerical results**

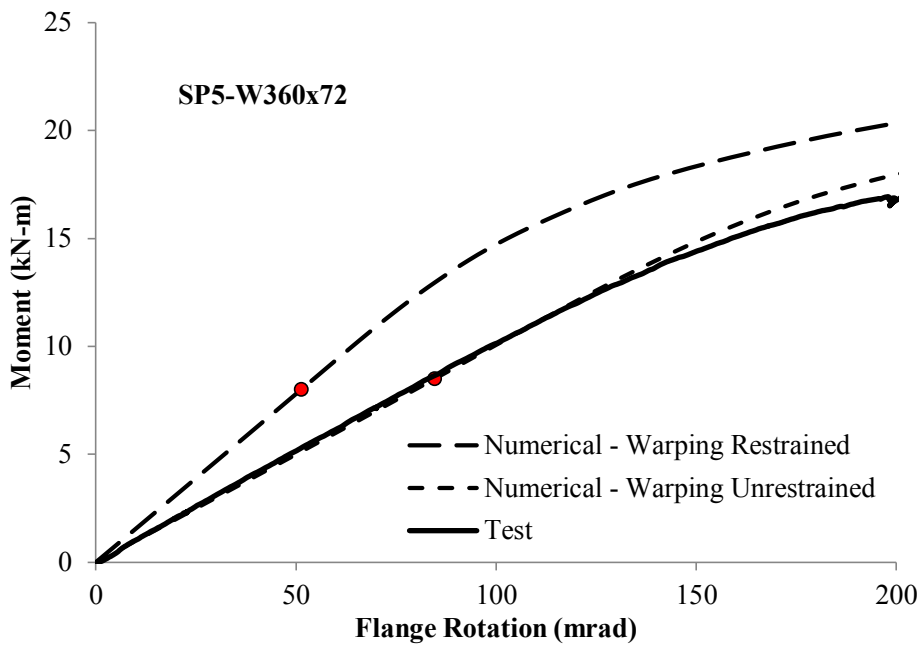


**Figure 4.27. Test result SP5-W360×72 compared with numerical results**

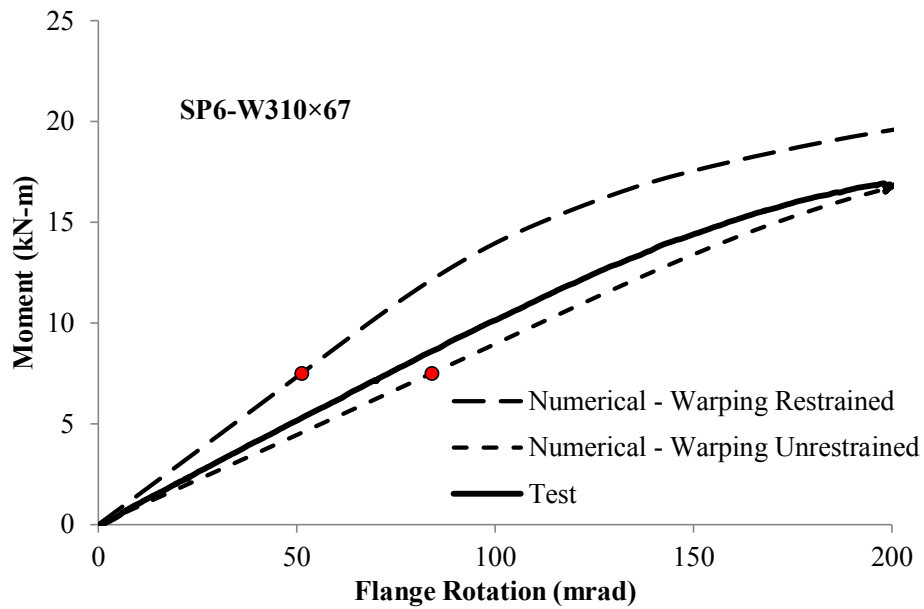


Figure 4.28. Test result SP6-W310×67 compared with numerical results

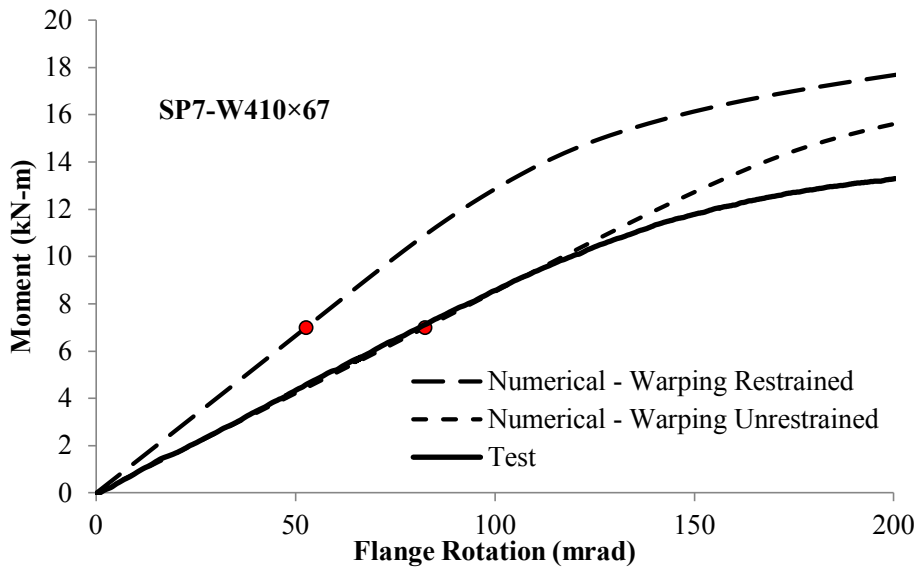


Figure 4.29. Test result SP7-W410×67 compared with numerical results

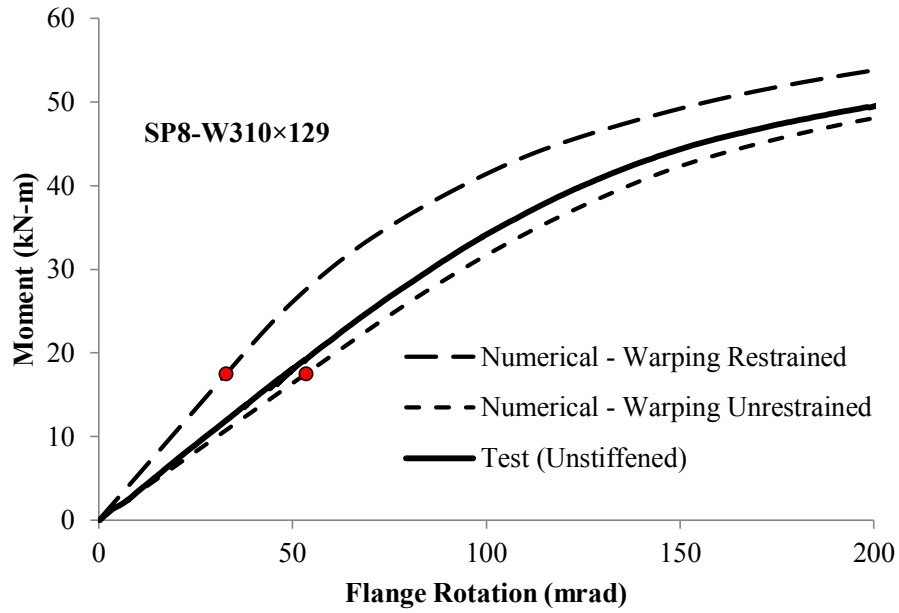


Figure 4.30. Test result SP8-W310×129 compared with numerical results

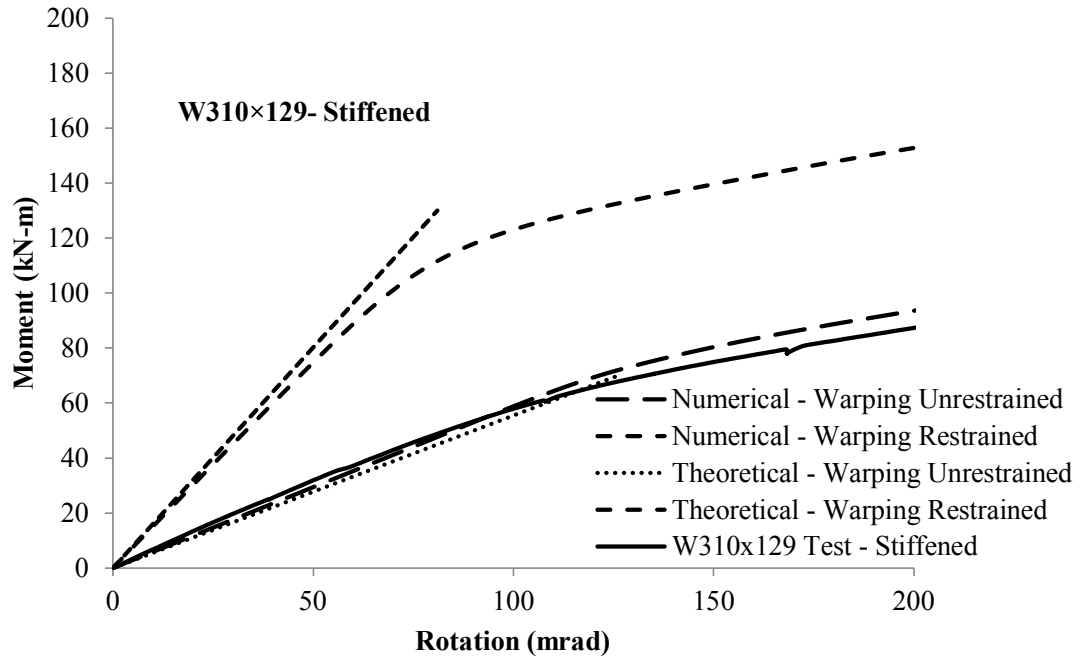


Figure 4.31. Test result SP9-W310×129 compared with numerical results

**Table 4.3. Initial yield moment comparison**

<b>Designation</b>	<b>Initial yield moment (kN-m)</b>		
	<b>Section</b>	<b>FEA (Warping Permitted)</b>	<b>Test results</b>
<b>SP1</b>	W360×162	22.5	No data
<b>SP2</b>	W310×86	9.0	8.14
<b>SP3</b>	W410×100	10.0	9.21
<b>SP4</b>	W250×80	8.0	7.35
<b>SP5</b>	W360×72	8.0	6.93
<b>SP6</b>	W310×67	7.5	6.58
<b>SP7</b>	W410×67	7.0	5.28
<b>SP8</b>	W310×129	17.5	16.0

## 5. Moment and Stiffness Prediction

Different methods for the assessment and prediction of the behaviour of unstiffened W-sections under torsion are discussed in the following sections. Separate formulations for initial stiffness and elastic moment capacity, based on the tests and numerical analysis, are presented. Behaviour under combined loading is explored numerically in this chapter and details for the introduction of axial load in the numerical models is discussed. Axial load is then incorporated into the calculation of the torsional elastic moment capacity of the members.

### 5.1. Maximum elastic moment capacity

It has been established in the previous chapters that as a torsional moment is applied through one flange of a W-section without any stiffeners, the restoring force is a combination of torsion of the flange and bending of the web along an effective width in the region where moment is applied. The restoring torque for the flange is provided in part by the supports at the ends of the member if the length of the member is small. However, the estimation of the exact parameters for the torsion of the flange and bending of the web is complex. Therefore, a simplified approach is used for prediction of the elastic capacity of the web that includes the contribution of the flange torsion.

The stresses in the web are highest in the connection region and decrease towards the supports. An effective width can be selected to approximate the decreasing profile of the stress away from the connection. Stress in this effective width is assumed to be constant throughout the length. In this method, the torsion of the flange is converted to an equivalent effect of bending of the web to create a simple method for design.

The most influential factor for determining the effective width is the ratio of torsional stiffness of the flange to bending stiffness of the web,  $r_f$ , as defined in Equation [3-7]. Numerical parametric studies and the test matrix discussed in Chapters 3 and 4 were based principally on this factor. Figure 5.1 shows the member with the effective width,  $b_{eff}$ , extending on both sides of the connection, where the full connection width to the extreme bolt lines is  $N$ . The extent of the effective width beyond the connection is determined by scaling the value of  $r_f$  based on the full set of 31 numerical analysis results for the initial yield moment, giving a mean test-to-predicted ratio of 0.96 for the W-sections in the range of the experimental study. The initial yield moment in the web is determined using Equation [5-1] and the associated total effective width, including the connection, is given by Equation [5-3].

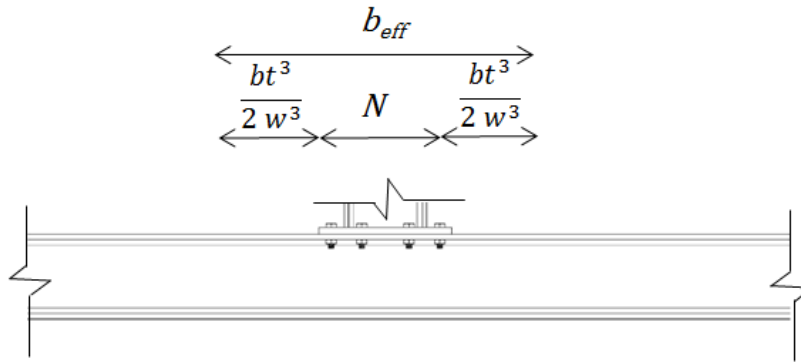


**Figure 5.1. Effective width of web for bending**

$$M_y = \frac{F_y \times w^2 \times b_{eff}}{6} \quad [5-1]$$

$$M_p = \frac{F_y \times w^2 \times b_{eff}}{4} \quad [5-2]$$

$$b_{eff} = N + 2 \times \frac{b \times t^3}{2 \times w^3} = N + r_1 \quad [5-3]$$

The initial yield moments determined from the tests and the numerical analyses, as well as those predicted by Equations [5-1] and [5-3], are given in Table 5.1. All cases utilize the yield stress or strain obtained from the coupon tests and the nominal geometrical properties. The initial yield moment values from the tests follow the same general trends as those predicted by the equation, but they are slightly lower in most cases. As discussed in Chapter 4, the presence of longitudinal tensile residual stresses in the critical region of the web would affect the point of onset of yielding, but this has been neglected as one side of the web would yield sooner and the other later. Moreover, as the initial yield moment was selected as the limit state, there is actually considerable excess capacity in the web even though it cannot be fully mobilized until deformations are quite large.

The same effective width can be used to compute the plastic web capacity by using Equation [5-2] instead of Equation [5-1]. If the effective width is considered equal for elastic and plastic capacities,

then a multiplier of 1.5 (shape factor for a rectangular section) can be applied to the initial yield test results to get the plastic web capacity in the tests. By assuming that the effective width does not change by extending to the fully plastic condition in the web, the test-to-predicted ratios will remain the same for the plastic web bending capacity as for the elastic capacity.

The web bending surface stress distribution (oriented perpendicular to the flange) for the W310×129 member with a 4 m length can be visualized using Figure 5.2. Bending stresses obtained from the numerical model at the surface nodes of the web are plotted along the length of the member. Two curves are depicted in Figure 5.2: elastic web capacity (initial yield point) and plastic web capacity ( $1.5 \times$  initial yield point). The extent of the assumed effective width is also marked on the plot for reference. As can be seen from the figure, the shapes of the two curves are similar, implying that the effective width of Equation [5-3] is reasonable for both conditions. Moreover, the contribution of the flange torsion in extending the effective bending width is significant.

Table 5.2 shows the maximum flange rotation for each test specimen at both the initial yield point and at the point where the web is nominally fully plastic. Rotations tabulated in Table 5.2 at  $M_y$  and  $1.5 \times M_y$  are extracted from the test data. In the experimental moment–rotation graphs the behaviour remains almost linear up to the point of  $1.5 M_y$ , and for that reason the ratio of the rotation at  $1.5 \times M_y$  to that at  $M_y$  is approximately, but slightly greater than, 1.5.

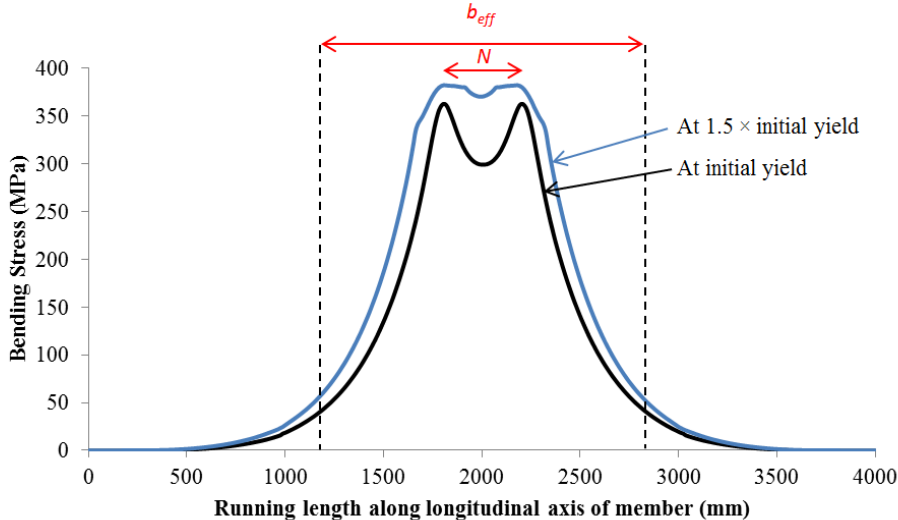


**Figure 5.2. Effective width of web for bending**

**Table 5.1. Comparison of initial yield moment**

Designation	Initial yield moment (kN-m)			Test-to-Predicted Ratio	
	Section	FEA (Warping Permitted)	Predicted by Eqn. [5-1]		Test
SP-1	W360×162	22.5	22.63	No data	-
SP-2	W310×86	9.0	9.06	8.14	0.90
SP-3	W410×100	10.0	9.63	9.21	0.96
SP-4	W250×80	8.0	7.64	7.35	0.96
SP-5	W360×72	8.0	6.77	6.93	1.02
SP-6	W310×67	7.5	6.56	6.58	1.00
SP-7	W410×67	7.0	5.69	5.28	0.93
SP-8	W310×129	17.5	16.39	16.02	0.98

**Table 5.2. Maximum flange rotations from test**

Designation	Flange rotation (mrad)		
	Section	At initial yield moment	At 1.5 × initial yield moment
SP1	W360×162	-	-
SP2	W310×86	50.7	77.0
SP3	W410×100	47.6	72.4
SP4	W250×80	52.5	79.3
SP5	W360×72	64.4	98.0
SP6	W310×67	63.6	96.3
SP7	W410×67	60.8	91.6
SP8	W310×129	43.6	66.5

## 5.2. Stiffness prediction comparisons

Studies conducted by Milner (1977; 1978) and Yura (2001) provide the grounds for the solution to compute the initial elastic stiffness of unstiffened W-sections under torsion applied through one flange. Equation [5-4] shows the structure of the stiffness prediction equation, where  $K_U$  is the net rotational stiffnesses of the connected flange in an unstiffened member. This equation utilizes the local bending stiffness of the web,  $K_w$ , and combines it with whole cross-sectional rotational stiffness of the member,  $K_S$ , as if it were stiffened sufficiently to transmit the applied torque into the member without localized distortion.

$$\frac{1}{K_U} = \frac{1}{K_S} + \frac{1}{K_w} \quad [5-4]$$

If the member is stiffened, the rotation will be dependent upon the properties of the whole cross-section, the length of the member, and the boundary conditions at the ends of the member. If unstiffened, it will be localized and will depend upon the cross-sectional dimensions of the web and flange.  $K_w$  is the factor that accounts for the distortion of the cross-section at the unstiffened web and, as this is a local phenomenon in the assumed configuration, it should not depend upon the member length or boundary conditions.

The numerical parametric study results are used to assess the effect of member length on the stiffness parameter  $K_w$ , which is computed by back calculation using Equation [5-4] and summarized in Table 5.3.  $K_S$  is calculated using Equation [2-13] and  $K_U$  is obtained by numerical analysis. Of the 32 models in the parametric study, 16 had a member length of 4 m, while the remaining 16 were 8 m in length.  $K_w$  values computed from the two groups matched well with their counterparts; that is, even with the large variation of cross-sectional properties  $K_w$  is influenced little by the length of the member. All the models in Table 5.3 had boundary conditions where warping was restrained, so to illustrate the ineffectiveness of the boundary conditions, selected models were re-run with warping permitted at the ends. It can be observed from Table 5.4 that in most cases  $K_w$  remains almost the same for the warping-restrained and warping-permitted boundary conditions. Where there is a significant difference, it is not expected to make any major difference in the resulting stiffness of the unstiffened member. For example, in 8L-300D-300B-16W-24F the difference in the computed  $K_w$  is significant (about 24%). However, when it is combined with the

elastic analysis of whole cross-sectional torsion of the member, the difference is 2% in the computed  $K_U$ . From Tables 5.3 and 5.4, it can be confirmed that neither the boundary conditions nor the member length have a significant effect on the local distortion of the web and flange.

The important factor in Equation [5-3] is  $K_w$  for the correct quantification of stiffness of a member without the stiffeners. Attempts made by Milner (1977; 1978) and Yura (2001) to set  $K_w$  were taken into account. Figure 5.3 shows values of  $K_w$  computed by Equation [2-5] (Yura 2001) compared with values computed from the numerical analysis back calculations of Equation [5-3]. In an attempt to improve the results, Equation [5-5] was developed using a scaled non-dimensional ratio of the most influential dimensions affecting the flange and web stiffnesses,  $t/w$ , which was observed to give same trends in the values of  $K_w$  as those derived from the numerical analyses. Based on the results of the parametric studies, and in particular the observation that the parameter  $r_l$  effectively incorporates the contribution of flange torsion into the effective width, Equation [5-5] was further modified to Equation [5-6]. In Equation [5-6],  $r_l$  has been scaled to achieve good agreement with the numerical analysis results. However, it was observed that for flanges with extremely high torsional stiffness, the full benefit of the stiffness could not be achieved. To account for this, in  $r_l$  an upper bound on the flange stiffness ( $bt^3$ ) is taken as  $3.5 \times 10^6 \text{ mm}^4$ . (It should be noted that this limit applies only to very heavy flanges, and it would not be encountered in most design cases.) In general,  $K_w$  given by Equation [5-6] is closer to numerical analysis results, as shown in Figure 5.3.

$$K_w = \frac{3.3 E}{h} \left[ (N + 1.5h) \left( \frac{w^3}{12} \right) \right] \times \frac{1.5 \times t}{w} \quad [5-5]$$

$$K_w = \frac{3.3 E}{h} \left[ (N + 1.5r_l) \left( \frac{w^3}{12} \right) \right] \quad [5-6]$$

Figures 5.4 to 5.11 show the predicted initial stiffnesses, using the  $K_w$  value computed by Equation [5-6], compared to the test results. For use in Equation [5-4],  $K_S$  has been computed for both the warping-permitted and warping-restrained boundary conditions. In all cases, the prediction for the warping-permitted case more accurately predicts the test behaviour.

**Table 5.3. Effect of member length on  $K_w$**

No.	Model Designation	$K_w$ (kN-m/rad)	
		4 m	8 m
1	300D-300B-8W-12F	246.6	246.8
2	300D-300B-8W-24F	530.1	633.2
3	300D-300B-16W-12F	903.6	894.0
4	300D-300B-16W-24F	1558.0	1661.9
5	300D-500B-8W-12F	310.9	305.2
6	300D-500B-8W-24F	873.4	873.9
7	300D-500B-16W-12F	733.7	695.5
8	300D-500B-16W-24F	1636.6	1633.1
9	500D-300B-8W-12F	163.5	163.9
10	500D-300B-8W-24F	358.1	349.1
11	500D-300B-16W-12F	603.3	596.0
12	500D-300B-16W-24F	986.4	1002.9
13	500D-500B-8W-12F	216.9	214.9
14	500D-500B-8W-24F	609.9	577.9
15	500D-500B-16W-12F	545.1	534.0
16	500D-500B-16W-24F	1108.5	1102.4

**Table 5.4. Effect of warping restraint on  $K_w$**

No.	Model Designation	$K_s$ (kN-m/rad) Warping Permitted	$K_U$ (kN-m/rad) Warping Permitted	$K_w$ (kN-m/rad)	
				Warping Permitted	Warping Restrained
1	4L-300D-300B-8W-12F	227.1	119.4	251.8	246.6
2	4L-300D-300B-16W-24F	656.8	475.5	1722.5	1558.0
3	4L-500D-500B-8W-24F	4994.9	549.6	617.6	609.9
4	8L-300D-300B-8W-12F	46.1	39.6	282.6	246.8
5	8L-300D-300B-16W-24F	201.1	184.0	2173.1	1661.9

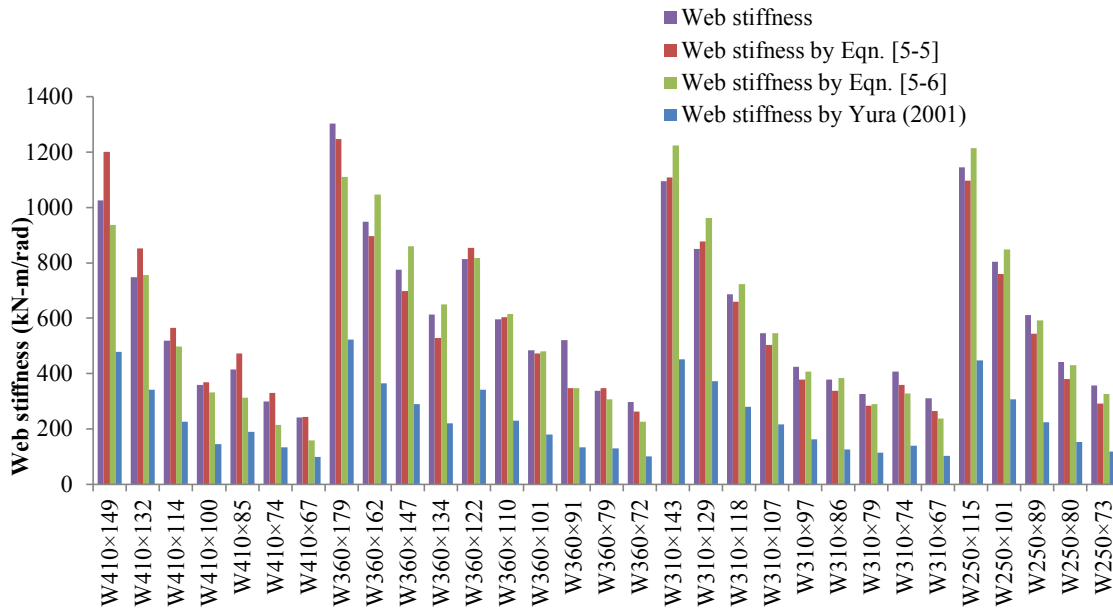


**Figure 5.3 Distortional stiffness ( $K_w$ ) comparison with numerical analysis results**

Considering the example of the modular pipe rack given in Figure 1.3, the beam (W310x79) has a span of 6 m between the columns (W310x129) and the total height of the columns is taken as 4 m. For instance, if a 30 kN-m fixed-end weak-axis moment would be produced at the beam ends, the effect on the joint by explicitly considering its flexibility can be computed using equations in Sections 5.1 and 5.2. A fixed-end moment of 30 kN-m will be produced, assuming elastic behaviour, if a concentrated load of the 40 kN is applied at the mid-span of the beam. The same load will give a rotation of 10.7 mrad at the supports if they are pinned. These results can be used to construct a beam line for the given beam and loading conditions. On analyzing the beam to bending between stiffened columns, due to the torsional rigidity of the columns a moment of 4.94 kN-m is produced at the beam ends (with a beam end rotation of 9.0 mrad). Without stiffeners, and adopting the procedures given in Sections 5.1 and 5.2 for the calculation of unstiffened rigidity of the column member, the end moment is decreased to 3.34 kN-m (end rotation of 9.5 mrad). As such, the fixed-end moment cannot be developed under either the stiffened or unstiffened column condition and the connection therefore need not be designed for it. Moreover, the nominal capacity of the unstiffened column, assuming a yield stress of 350 MPa, is  $M_y = 16.1$  kN-m, which is insufficient under the fixed-end assumption, but is several times the required capacity if the connection flexibility is explicitly taken into account. In this scenario, due to redistribution of

moment caused by the flexible support condition, the beam section should be re-checked for adequacy for weak-axis bending at mid-span.

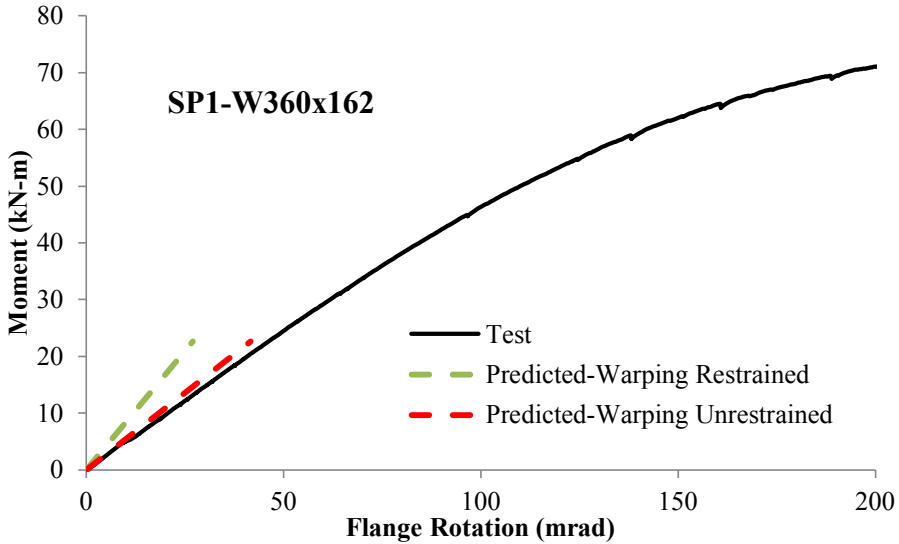


Figure 5.4. Test vs. predicted results SP1

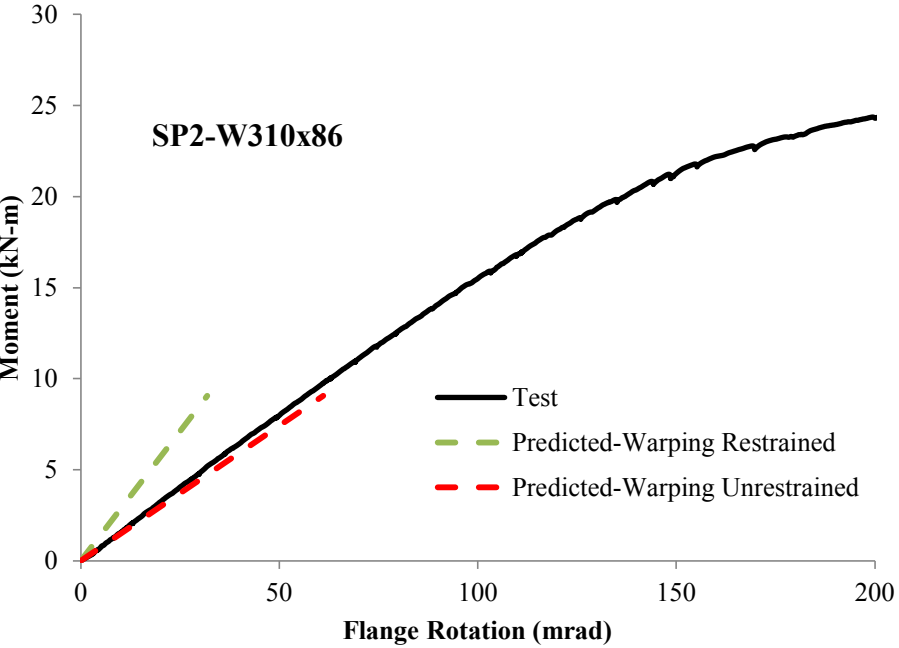
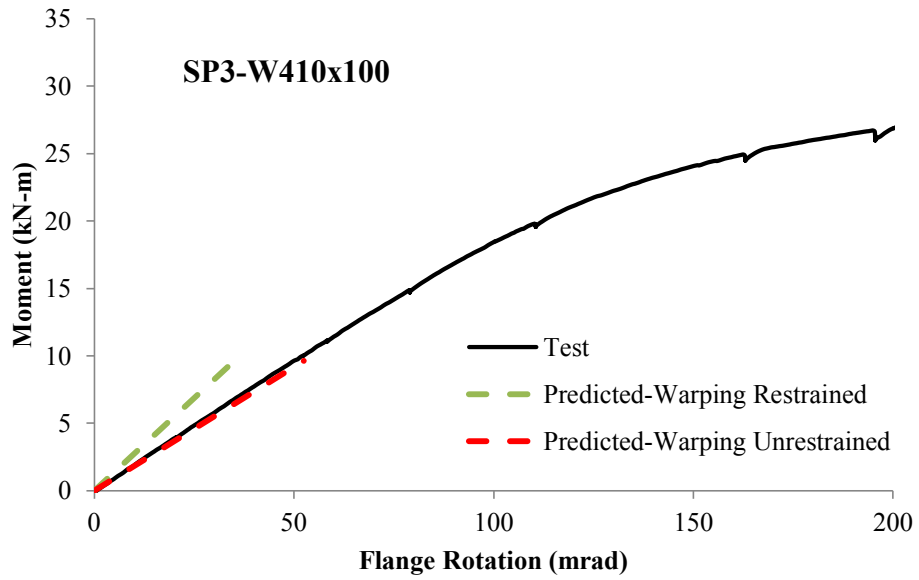
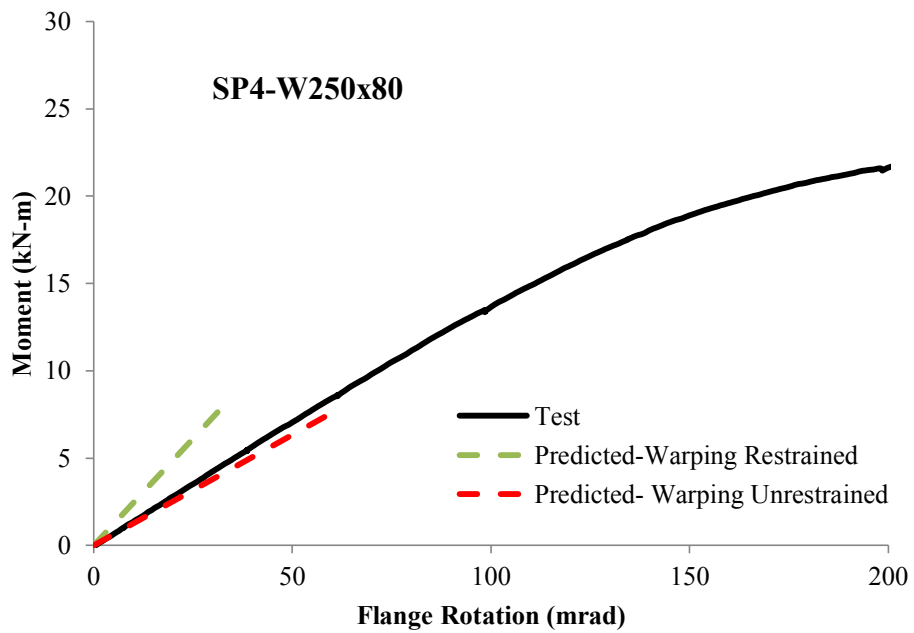


Figure 5.5. Test vs. predicted results SP2



**Figure 5.6. Test vs. predicted results SP3**



**Figure 5.7. Test vs. predicted results SP4**

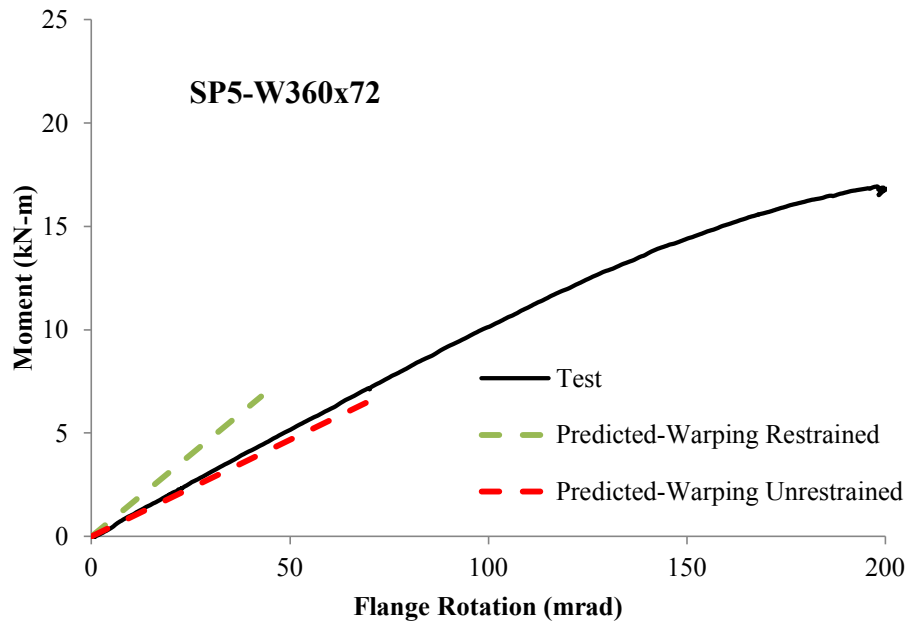


**Figure 5.8. Test vs. predicted results SP5**

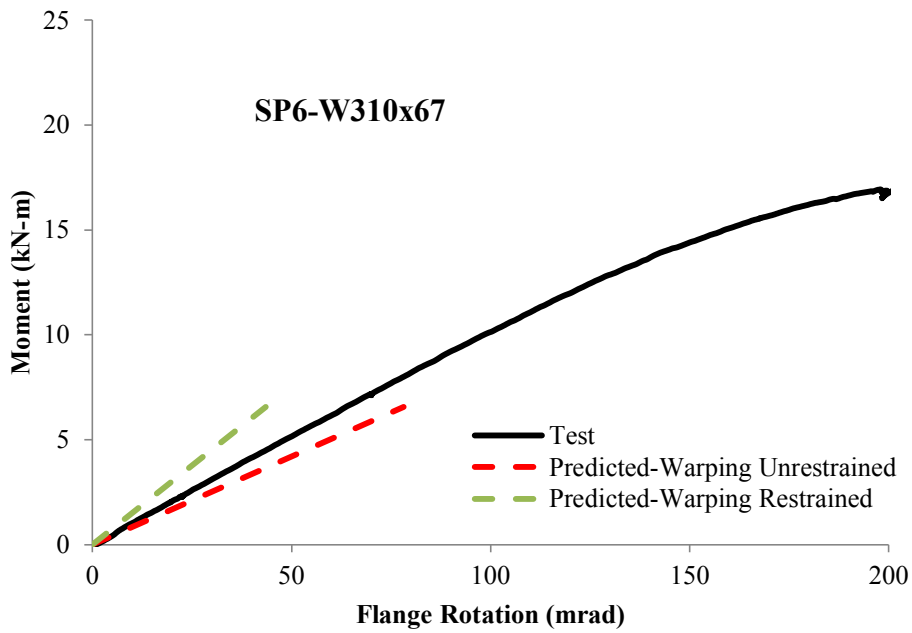


**Figure 5.9. Test vs. predicted results SP6**

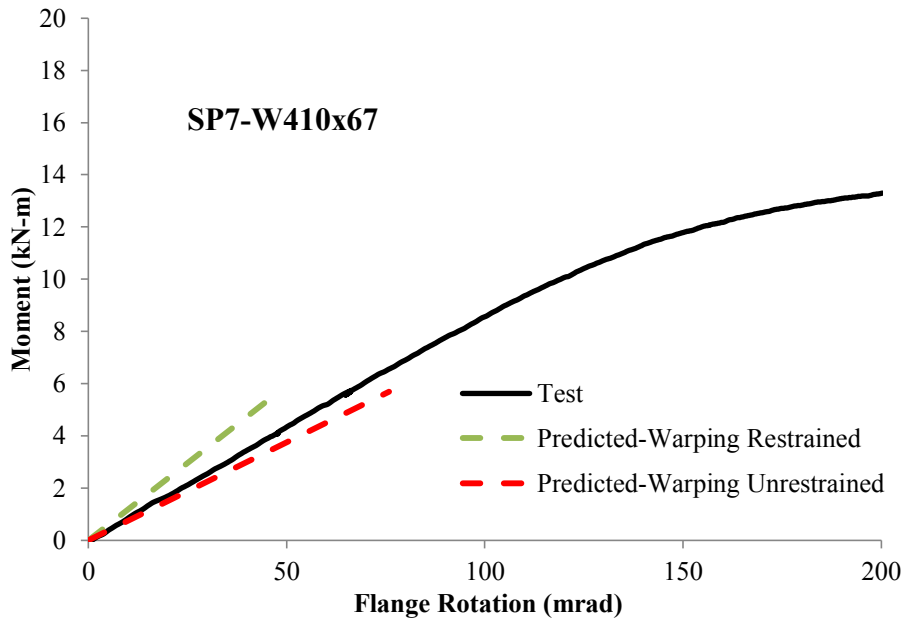


**Figure 5.10. Test vs. predicted results SP7**

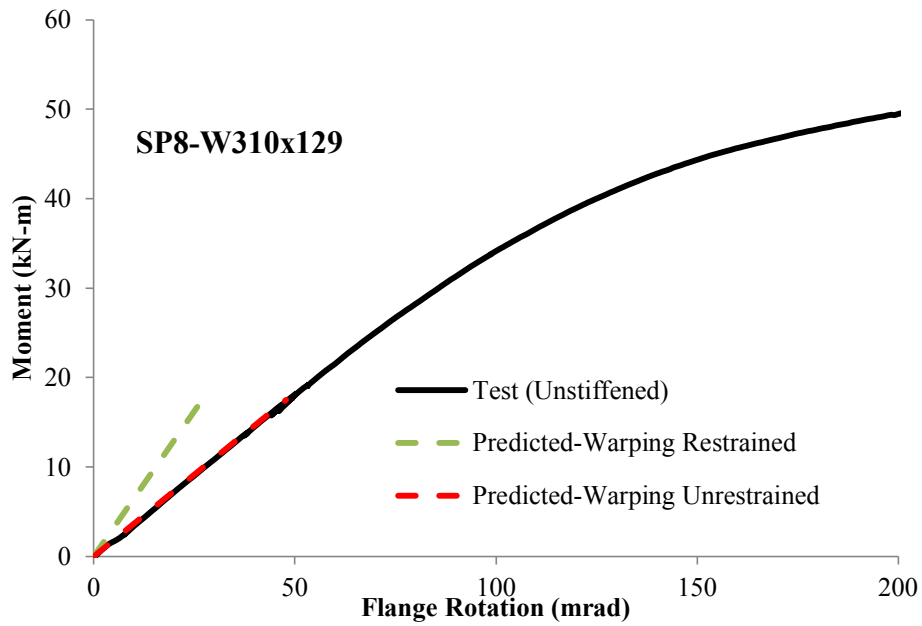


**Figure 5.11. Test vs. predicted results SP8**

### 5.3. Axial load effect

Often members are subjected to combinations of loadings. For example, the column in Figure 1.4 is subjected to axial load accompanied by weak axis moment. The weak axis moment for the beam, resulting in the twisting of one flange of the column, can be of concern if the column is already carrying axial load.

In addition to the axial load, out-of-plane movement caused by weak axis moment of the beam will put extra demand on the capacity of the column web at the connection. The region adjacent to the connection will be more stressed than the rest of the member and may control the design of the column. Another possibility of failure could be when higher axial loads are applied, and in this situation excessive out of plane movement could cause instability of the column.

Finite element models made for parametric study were used with few modifications. Material and mesh schemes were kept the same, with modifications introduced in the load and boundary conditions. The boundary condition at one end of the member was fixed by restraining all the nodes at that end of the member, whereas at the other end only the X and Y displacements were restrained keeping the Z direction unrestrained to apply the axial load at this end. To apply axial load on this end, all the points were kinematically tied to one reference point. The concentrated axial load applied at that reference point was transferred to all the nodes on the cross-section without any local deformation. In the first stage the axial load was applied, and moment was applied in the second stage with small steps while the axial load was kept constant. For the moment, pressure was applied at the flange, and details for this loading scheme have already been discussed in Chapter 3.

For the first FEA runs, high axial load was applied to study the stability behaviour due to out-of-plane movement of column. These models were run to be sure that the column will not undergo catastrophic failure due to this instability caused by the already-applied axial load. In Static-General analysis in Abaqus, load is applied in positive increments and if the deformations are large then the solver will decrease the load applied in an increment, but all increments will still be positive. Upon very large deformations or in the case of very small load increments, analysis terminates. In the static Riks model, it is left to the software to decide about the load intervals and if there is any instability the load proportionality factor will change the sign. Static Riks models take care of either buckling or non-linear behaviour. As the column buckles, the load proportionality factor drops and Abaqus decides on a very small incremental load. For high axial loads, static Riks models were run in addition to static models.

In the following discussions, for the magnitude of the axial load interaction a percentage has been used. For example, 100% axial load means the full cross-sectional compressive load carrying capacity ( $A_g F_y$ ) of the member is applied without any stability (buckling) concerns.

For the 4 m long 4L-300D-300B-8W-12F section, at 100% axial load the torsional moment reached its peak at 0.8 kN-m and the load proportionality factor then started decreasing for the linear static Riks step. For static analysis with an axial load of  $A_g F_y$ , it also terminated at 0.8 kN-m, proving that at a high axial load out-of-plane movement of the flange can cause instability in the model. Another way to put this is that all the capacity was utilized by the axial load, and weak axis moment could not be resisted. However, when the axial load was reduced to 90% the member yield strength, web yielding began at 3 kN-m and failure occurred at a torsional moment of 8 kN-m for both type of analysis. An initial yield moment of 3 kN-m combined with 90% axial load is significant compared to the yield moment of 8.5 kN-m for the case without any axial load on the member.

However, on increasing the length instability was observed at 90% of the axial load capacity at a lower weak-axis moment. For instance, 4L-300D-300B-8W-12F at 100% axial load failed at a moment of 0.18 kN-m and for 90% axial load a 4 kN-m moment caused the member to undergo complete failure. So, for further analysis, the axial load was kept well below the maximum axial load capacity to keep the member within the stable range of moment. All the models afterwards were run using the static load step.

To understand the interaction between the torsion and axial load properly, axial loads equal to 25%, 50%, and 75% of the full cross-section capacity were considered. The effect on the elastic moment with varying axial load is given Table 5.5. For 25% axial load, on average a 10% decrease in the moment was observed with the maximum being 18% and minimum being 6%. On increasing the load up to 50%, on average the decrease was 28% from the case with no axial load, with upper and lower limits being 44% and 20%. For 75% axial load, the upper bound was a 64% decrease and the lower bound was 41%, with an average decrease of 52% from the case with no axial load. In many cases with 50% and 100% axial load, yielding started in the flanges prior to the web. However, this was just the initiation of yield and the member kept on taking load to achieve yielding of web. In these cases where the flanges yielded first, “F” has been appended to values in the table and web yield values are given after that.

**Table 5.5. Axial load effect on parametric study models**

Model Designation	Moment Without Axial Load	Moment with 25% Axial Load	Moment with 50% Axial Load	Moment with 75% Axial Load
	kN-m	kN-m	kN-m	kN-m
4L-300D-300B-8W-12F	8	7	6	4
4L-300D-300B-8W-24F	15	14	11.5	8
4L-300D-300B-16W-12F	16	14.5	10F-12.5	5F-7
4L-300D-300B-16W-24F	27	24.5	20.5	12F-14
4L-300D-500B-8W-12F	11	9	7	4
4L-300D-500B-8W-24F	22	19	15.5	10.5
4L-300D-500B-16W-12F	20.5	18	14	9
4L-300D-500B-16W-24F	31.5	28.5	23	15
4L-500D-300B-8W-12F	8.5	7.5	6.5	4.5
4L-500D-300B-8W-24F	17.5	16	13.5	9.5
4L-500D-300B-16W-12F	16	14.5	12F-12.5	6F-7
4L-500D-300B-16W-24F	28	25.5	21	14.5
4L-500D-500B-8W-12F	11.5	10	7.5	4.5
4L-500D-500B-8W-24F	25.5	22.5	18.5	12.5
4L-500D-500B-16W-12F	21	18	14	9
4L-500D-500B-16W-24F	34.5	30.5	25	16.5
8L-300D-300B-8W-12F	8	7.5	6	3F-4.5
8L-300D-300B-8W-24F	16	15	12.5	8.5F-8.5
8L-300D-300B-16W-12F	17	11.5F-15	5.5F-12.5	3.5F-8.5
8L-300D-300B-16W-24F	28	25.5	19F-21.5	9.5F-14.5
8L-300D-500B-8W-12F	11	9	7.5	4
8L-300D-500B-8W-24F	22.5	20	12.5	10.5
8L-300D-500B-16W-12F	21	18	14	6.5F-9.5
8L-300D-500B-16W-24F	33	29.5	23.5	15.5
8L-500D-300B-8W-12F	8.5	8	6.5	3.5F-5
8L-500D-300B-8W-24F	17.5	16.5	14	9.5F-10
8L-500D-300B-16W-12F	16	13.5F-15	8.5F-12.5	4F-8.5
8L-500D-300B-16W-24F	28.5	26	20.5	10F-15.5
8L-500D-500B-8W-12F	11.5	9.5	7.5	4.5
8L-500D-500B-8W-24F	25	22	18	12.5
8L-500D-500B-16W-12F	21	18	14	7.5F-9
8L-500D-500B-16W-24F	35	31	25	16.5

For justification of the decrement in moment capacity due to the presence of axial load, the von Mises yield criterion was used. The von Mises criterion is common and considered a reliable

method to predict when a metallic material will undergo plasticity. It takes into account the various states of stresses—i.e., normal stresses and shear stress—and gives an equivalent uniaxial stress. When this equivalent stress increases to the uniaxial yield stress, the material is said to be yielded. Various configurations of the von Mises equation are possible. However, for interaction between stresses induced by axial force and torsional moment, Equation [5-7] will be utilized. Stresses imposed by axial load and moment, as depicted in Figure 5.12, are highlighted in Equation [5-7].

$$\sigma_v = \sqrt{\frac{(\sigma_{11} - \sigma_{22})^2 + (\sigma_{22} - \sigma_{33})^2 + (\sigma_{33} - \sigma_{11})^2 + 6(\sigma_{12}^2 + \sigma_{13}^2 + \sigma_{23}^2)}{2}} \quad [5-7]$$

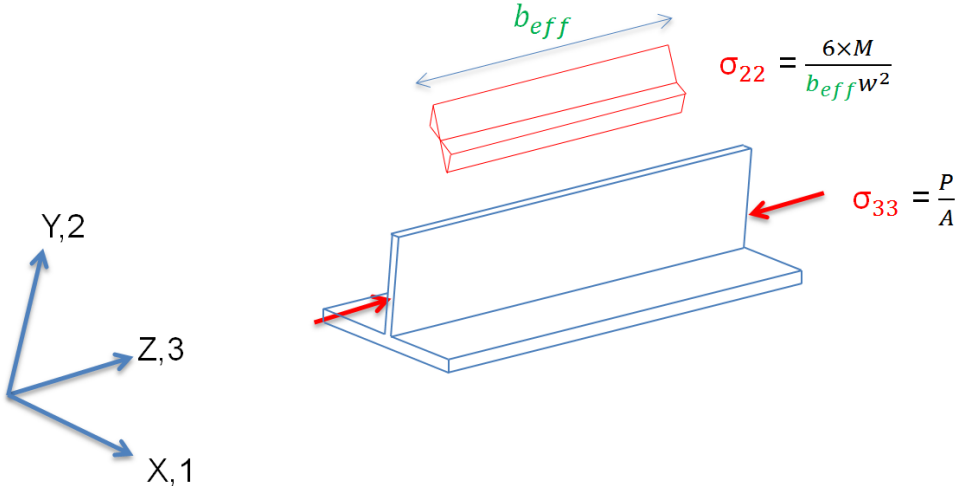


**Figure 5.12. Stresses due to axial load and bending effect**

Axial load if applied concentrically without any moment will cause the  $\sigma_{33}$  stress component, and other components will approach to zero. With weak axis moment, the major component will be  $\sigma_{22}$ , but due to plate-like behaviour other components will also have a contribution towards the yield stress but they should be comparatively much smaller than  $\sigma_{22}$ .

To represent the stress due to moment, a point (node) on the web in the numerical analysis model was selected where yielding was reached (utilizing PEEQ) before the other nodes. Stress

components at that point were extracted. This was done for the case without any axial load applied on the member.

Figure 5.13 shows various components of the stress plotted against increasing moment. Stress components ( $\sigma$ ) are shown by (S) in the graph. Dotted lines show stress components only due to moment without any axial load. Stress components S11-M, S22-M, S33-M, S12-M, S23-M and S13-M are stress components only due to the moment. The largest component out of all these stresses is S22-M, which is caused by the bending of the web. S33-A50% and S33-A75% are the components of the stress corresponding to 50% and 75% of the yield stress, respectively, and will be produced if an axial load is applied on the member. As the moment is increased, stress components for the moment change, whereas for axial load there is only one component and it is constant as load was applied and kept constant during the moment phase of the loading. Combining the stress components from the numerical analysis due to moment only with the axial load stress components manually, the von Mises stress has been computed by Equation [5-7]. Change in the von Mises stress has been plotted by solid lines on the graph for no axial load, 50% axial load, and 75% axial load. Von Mises stress has been obtained for the axial load cases by adding the stress component S33-A to S33-M and evaluating Equation [5-7]. A horizontal dashed line drawn at the von Mises yield stress (350 MPa) for the moment only combination intersects the von Mises combinations of the 50% and 75% axial load cases at the moment values of 20.5 kN-m and 14 kN-m. These values justify the gradual decrease in the moment depicted in Table 5.5 due to the axial load.

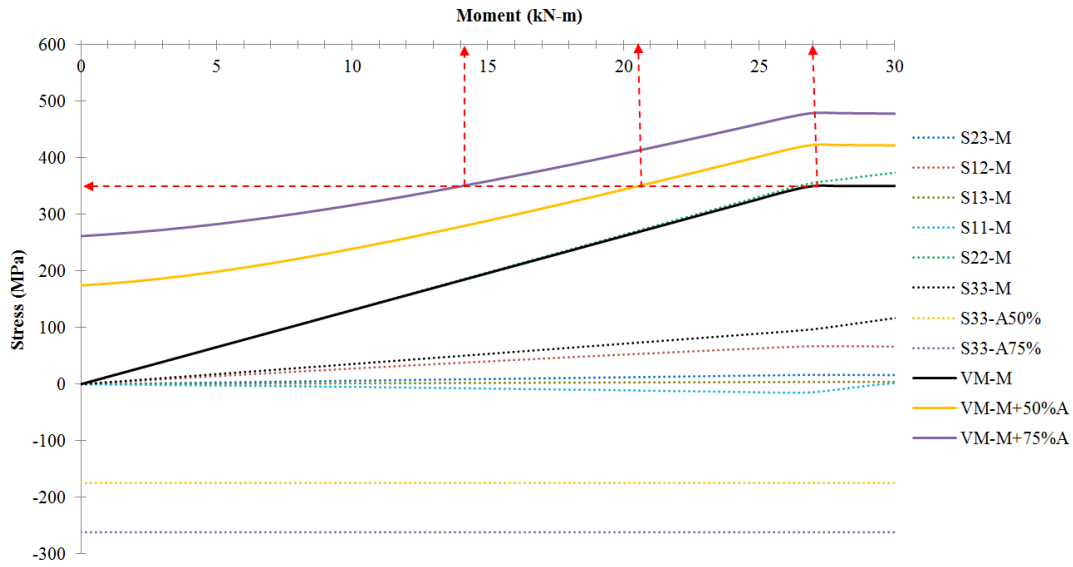


**Figure 5.13. Illustration of interaction of stresses according to von Mises equation**

#### 5.4. Combined axial load effect prediction

After the axial load stress verification exercise in the previous section, the next step would be to create a simple interaction relationship between the axial load and moment. For this purpose, bilinear interactions have been used and the interaction value has been taken as 0.8 based on the results of 96 numerical analysis models. The average value obtained was 0.8, with a standard deviation of 0.07. As PEEQ is not the true failure point and there is a lot of reserve capacity, fixing 0.8 as the limit will give a safe evaluation of strength. Figure 5.14 shows the plot of Equation [5-6].

$$\left(\frac{P}{P_y}\right)^2 + \left(\frac{M}{M_y}\right)^2 = 0.8 \quad [5-8]$$

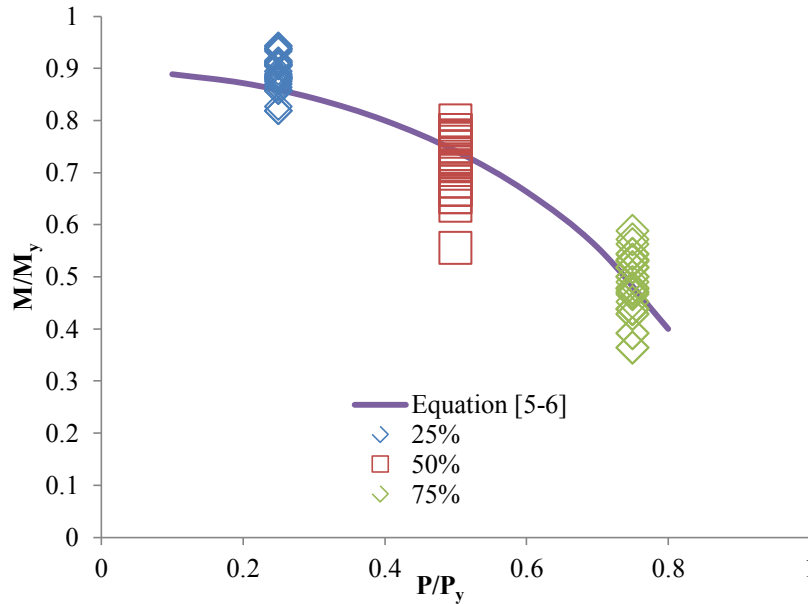


**Figure 5.14. Interaction comparison**

The above empirical formulation has shortcomings. First, this equation does not represent the actual behaviour. For example, at zero axial load the capacity predicted is 90% of the full yield capacity, whereas it should be 100%. Second, it under-predicts the torsional capacity when combined with the axial load. A direct solution was computed using the von Mises equation and major stress components shown in Figure 5.12. In this method, only two major components of the stress have been considered, one due to bending of the web and the other due to axial load. It has been assumed that the effective width computed according to Equation [5-4] does not change when axial load is applied. As the axial load is applied, the decrease in the available capacity for web bending is computed by the interaction described by the von Mises equation. This modified stress is then utilized in the bending equation. This solution was found to be more compatible with the effective length method for determining moment capacity. Equation [5-9] accounts for the interaction of the axial load with torsional moment.  $b_{eff}$  can be computed by using Equation [5-4]. This equation under-predicts the torsional capacity by the average amounts shown in Figure 5.15 for 25%, 50%, and 75% of the axial yield capacity.

$$M = \left| \frac{\frac{P}{A} - \sqrt{4F_y^2 - 3\left(\frac{P}{A}\right)^2}}{2} \right| \times \frac{b_{eff} \times w^2}{6} \quad [5-9]$$

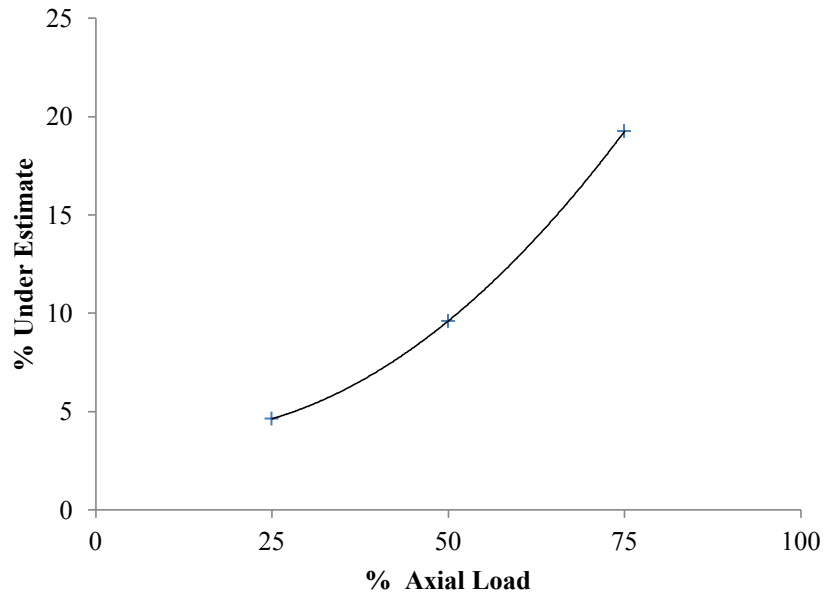


**Figure 5.15. Error in the predicted capacity with axial load**

The other major aspect is the stiffness prediction of the member. As all the computations are based on the elastic loading stage, addition of axial load in the elastic stage will not change the initial stiffness of the member. Figure 5.16 shows the moment–rotation response of a member with varying axial loads. Initial stiffness in the elastic range remains constant for all the cases with axial loads. Therefore, the same stiffness formulations discussed in Section 5.2 can be utilized for members with axial load.

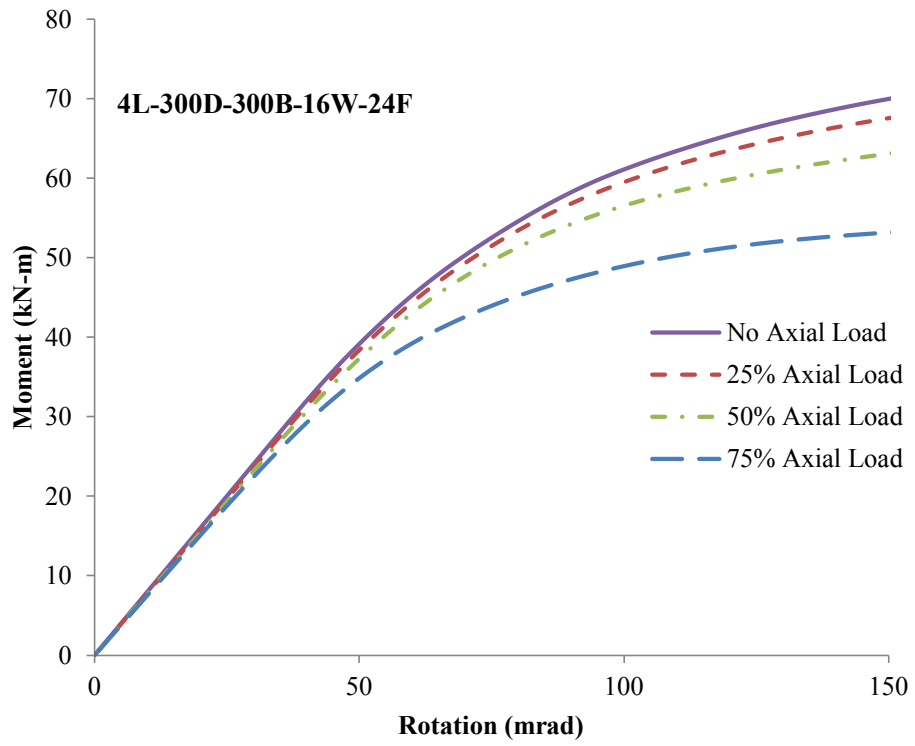


**Figure 5.16. Moment rotation response under different axial loads**

## **6. Summary and Recommendations**

### **6.1. Summary**

Local cross-sectional distortion due to torsional loading applied on unstiffened wide flange sections through one flange may occur in many types of structures such pipe racks and guardrail supports. However, no design method existed previously for determining the capacity of the member, without the use of stiffeners, that has been substantiated by full-scale laboratory tests. Stiffeners added to the cross-section are a common solution even for a small applied torques, but this can add significant unnecessary costs. Behaviour of unstiffened wide flange members was unexplored in the literature and design standards do not address this problem directly. As such, new studies have been conducted to provide the basis to calculate the behaviour of the unstiffened member for design. Numerical analysis studies combined with full-scale laboratory tests have been performed.

In addition to the need for evaluating the strength of a member subjected to torsional loading, its rotational stiffness may also need to be evaluated. Studies were conducted by Milner (1979) and Yura (2001), who proposed a parameter that can account for the local deformations of the web. For the moment capacity, solutions by Dowswell (2003) and Kristensen (2010) provided input to this research. Dowswell (2003) proposed an effective length of web for the calculation of its elastic capacity. While the theory for the behaviour of elastic stiffened cross-sectional torsion is well recognized, no universal guideline exists for unstiffened members.

Comprehensive numerical analysis studies were performed. Initial numerical analysis focused on the study of the whole cross-sectional torsion, or torsion with stiffeners, and its comparison with theory. These numerical analysis models gave good agreement with the theory and were modified for unstiffened modelling of the member under torsional loading. Application of the torsional loading on the member by different methods resulted in same response. In addition to cross-sectional dimensions, numerical modelling parametric studies also included the effect of boundary conditions, mesh and element types. Length of the member, section depth, flange width, web thickness and flange thickness were taken as the geometric variables and numerical models were run with a broad array of combinations. Out of this parametric study, the web thickness, flange thickness and flange width were found to be key variables contributing towards the capacity of the unstiffened member. For the more practical application of the results, standard W-sections from the CISC Handbook of Steel Construction, with flange thicknesses ranging from 12 mm to 24 mm, were selected and their capacities and stiffnesses were obtained from the numerical models. The

study focussed on this range of W-sections for the solution for unstiffened torsion. These numerical parametric studies showed that the ratio of the flange stiffness to the web stiffness had an influence over the maximum elastic moment capacity.

For the verification of the numerical analysis results, a full-scale testing program was completed. The stiffness ratio of the flange to web was considered for the formation of a test matrix, which consisted of eight unstiffened W-sections and one stiffened section. The results from the tests were in accordance with the numerical analysis results.

For the prediction of moment capacity and stiffness, systematic methods have been discussed. For the moment capacity, a proposed effective width gave results in a close range compared to the results obtained by tests. The local distortional effect has been characterized by refining the parameter responsible for the web distortions. Behaviour of the member under combined loading consisting of unstiffened torsion and axial load has also been studied. The axial load effect has been evaluated using numerical analysis and has been introduced into the equation for moment capacity.

## **6.2. Recommendations for further research**

Even though studies have been conducted to probe into the behaviour of the unstiffened members, there still remain certain directions to be further investigated. For example, behaviour of the member under combined torsion and axial loading has only been studied numerically. Full-scale physical tests are still required for verification of the proposed methods. These tests will further the knowledge of the unstiffened response, eliminating any stability concerns arising from the axial loads.

Another aspect to be explored is the combined effect of the torsional moment with strong axis moment on an unstiffened member. This strong axis moment can be a result of axial load beam or the transfer from the strong axis moment from the adjoining beam.

## References

Ahmad, M., Driver, R.G., Callele, L., and Dowswell, B. (2015) "Behaviour of Unstiffened Wide-flange Members Subjected to Torsional Moment Through One Flange." *Proc., Annual General Conference, Canadian Society for Civil Engineering*, Paper GEN-153, May 27-30, Regina, SK, Canada.

AISC (2010). "*Specification for Structural Steel Buildings.*" *ANSI/AISC 360-10, June 22*, American Institute of Steel Construction, Inc., Chicago, IL.

ASTM Standard A370-14. (2014). "Standard Test Methods and Definitions for Mechanical Testing of Steel Products." *ASTM International*, West Conshohocken, PA.

ASTM Standard A6/A6M-14. (2014). "Standard Specification for General Requirements for Rolled Structural Steel Bars, Plates, Shapes, and Sheet Piling." *ASTM International*, West Conshohocken, PA.

CISC. (2010). "Handbook of Steel Construction." 10th Edition, Fourth Revised Printing 2012. *Canadian Institute of Steel Construction*, Markham, ON.

Dowswell, B. (2003). "Connection Design for Steel Structures," Course Notes for the Seminar Sponsored by the *American Society of Civil Engineers*.

Heins, C.P., and Seaburg, P.A. (1964). "Torsion Analysis of Rolled Steel Sections." *Steel Design File No. 13-A-1, Bethlehem Steel Corporation*, Bethlehem, PA.

Kristensen S. (2010). "Single Sided Structural Beam to Column Joint of H or I –Profiles with Bolted Endplate Exposed to In-plane and Out-of-plane Bending." *Master's Thesis*, University of Stavanger. Stavanger, Norway.

Milner, H.R. (1977). "The Design of Simply Supported Beams Braced Against Twisting on the Tension Flange." *Civil Engineering Transactions*, Institute of Engineers, Australia, CE 19 / 1, pp. 84-91.

Milner, H.R. (1977). "Test on Equal Flanged Beams Braced Against Twisting on the Tension Flange." *Civil Engineering Transactions*, Institute of Engineers, Australia, CE 19 / 1, pp. 92-100.

Milner, H.R. and Rao, S.N. (1977). "The Twisting of Universal Beam Members by a Torsion Moment Applied to One Flange," *Proc., Sixth Australasian Conference on the Mechanics of Structures and Materials*, University of Canterbury, Christchurch, New Zealand, pp. 293-298.

Milner, H.R. and Rao, S.N. (1978). "Strength and Stiffness of Moment Resisting Beam -Purlin Connections," *Civil Engineering Transactions*, Institute of Engineers, Australia, CE 20(1), pp. 37-42.

Salem, P., and Driver, R.G. (2014). "Behaviour Of Unstiffened Extended Shear Tabs Under Shear Loading." *Proc., 4th International Structural Specialty Conference*, Canadian Society for Civil Engineering, Halifax, N.S.

Seaburg, P.A., and Carter, C.J. (2003). "Torsional Analysis of Structural Steel Members, Steel Design Guide No. 9." *American Institute of Steel Construction*, Chicago, IL.

Winter, G., Lasing, W., and McCalley, R.B. (1949). "Performance of Laterally Loaded Channel Beams." *Research Engineering Structural Supplement*, London, 49p.

Yura, J.A. (2001). "Fundamentals of Beam Bracing." *Engineering Journal, American Institute of Steel Construction*, First Quarter, pp. 11-26.

**Appendix A**  
**Test Specimen Drawings**

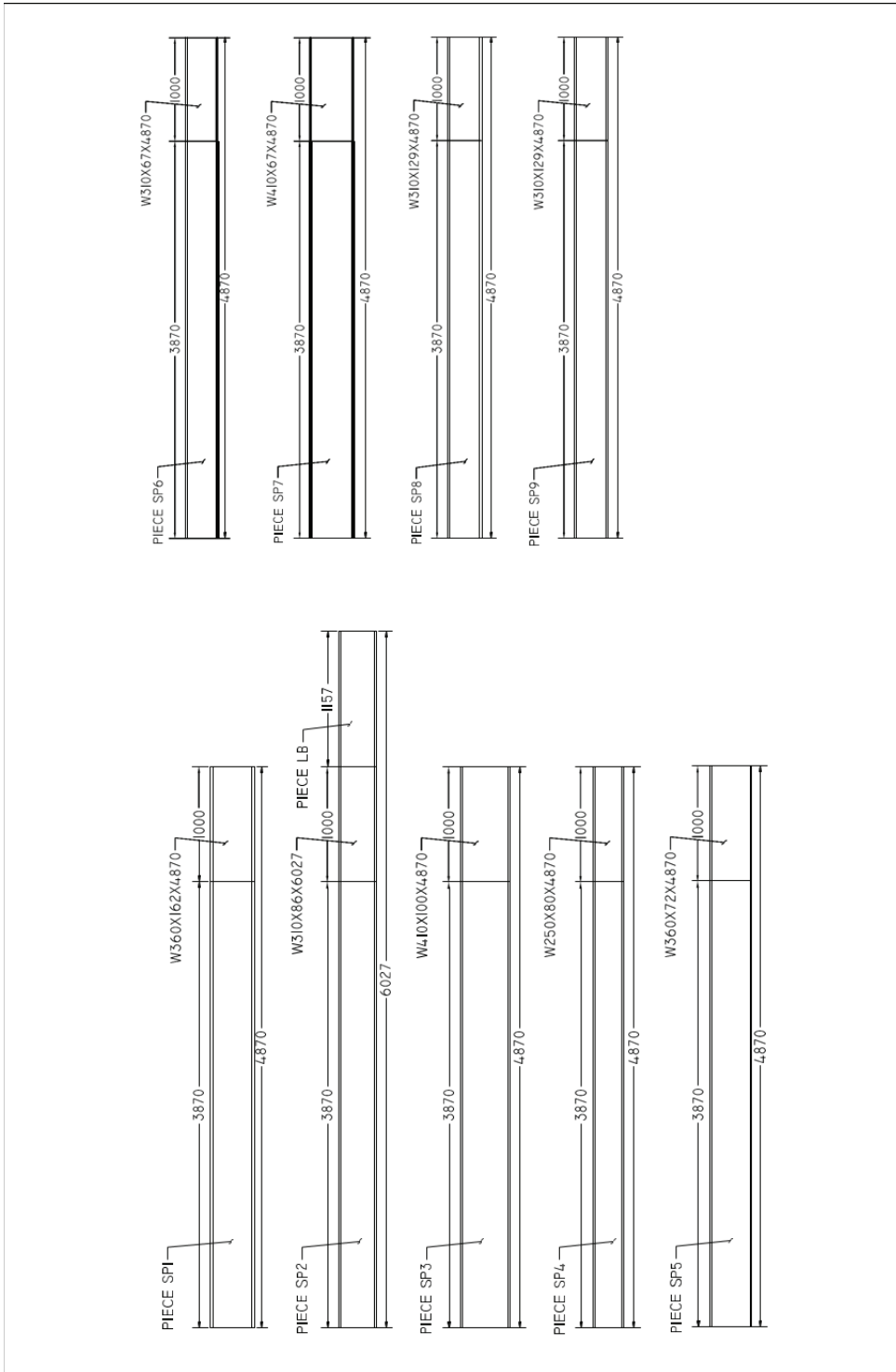


Figure A.1. Drawing material cut-outs

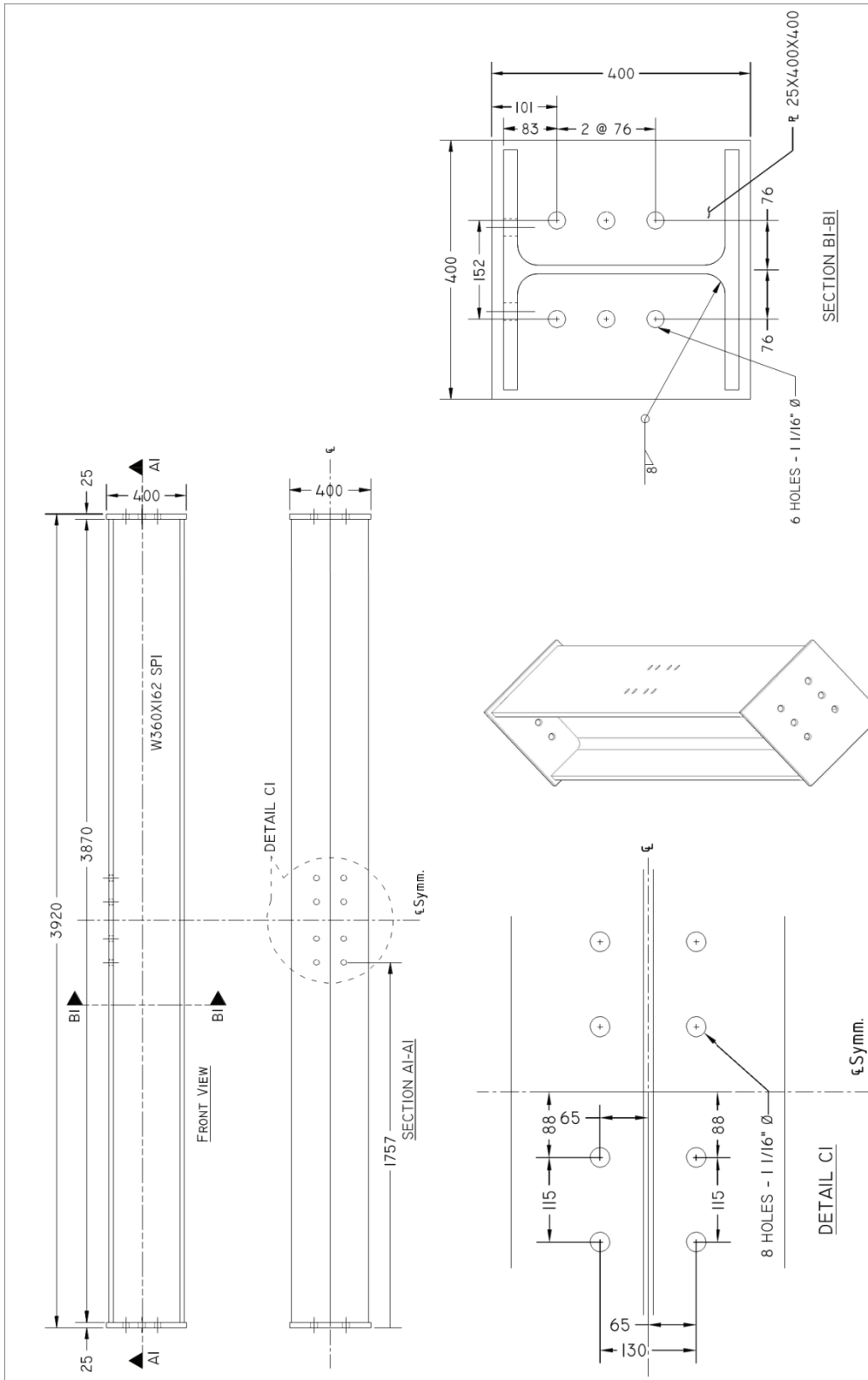


Figure A.2. Drawing SPI

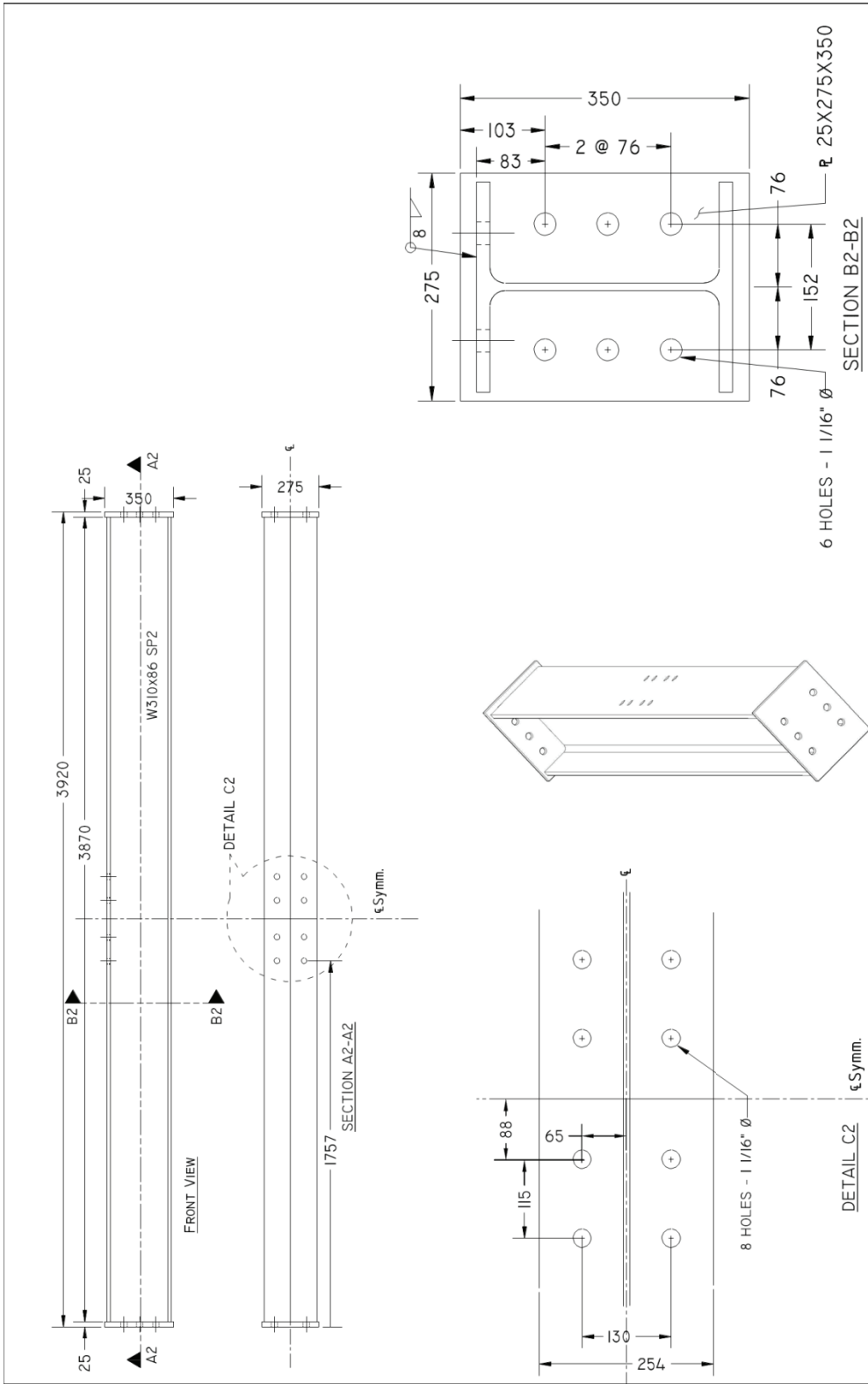


Figure A.3. Drawing SP2

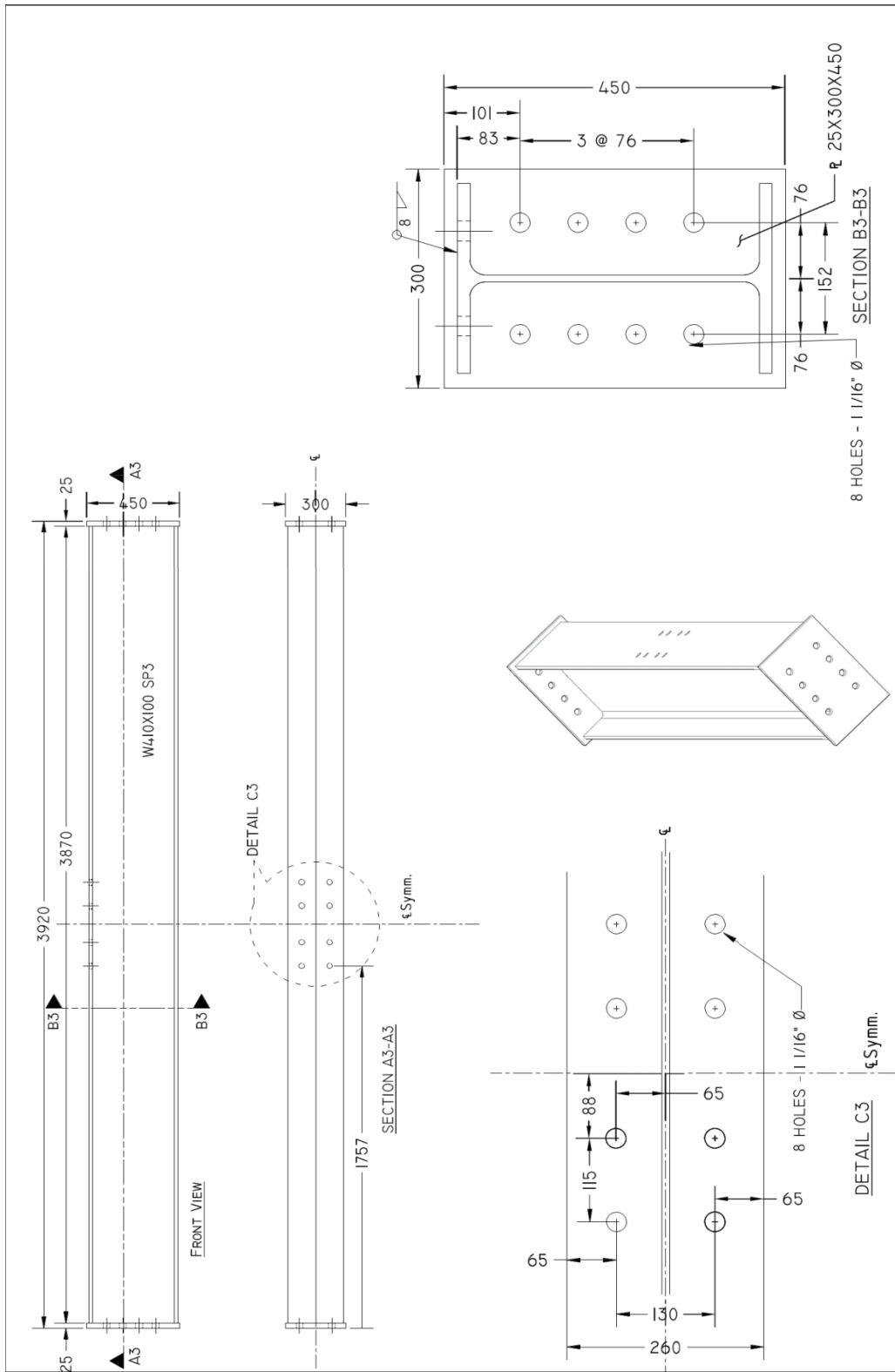


Figure A.4. Drawing SP3

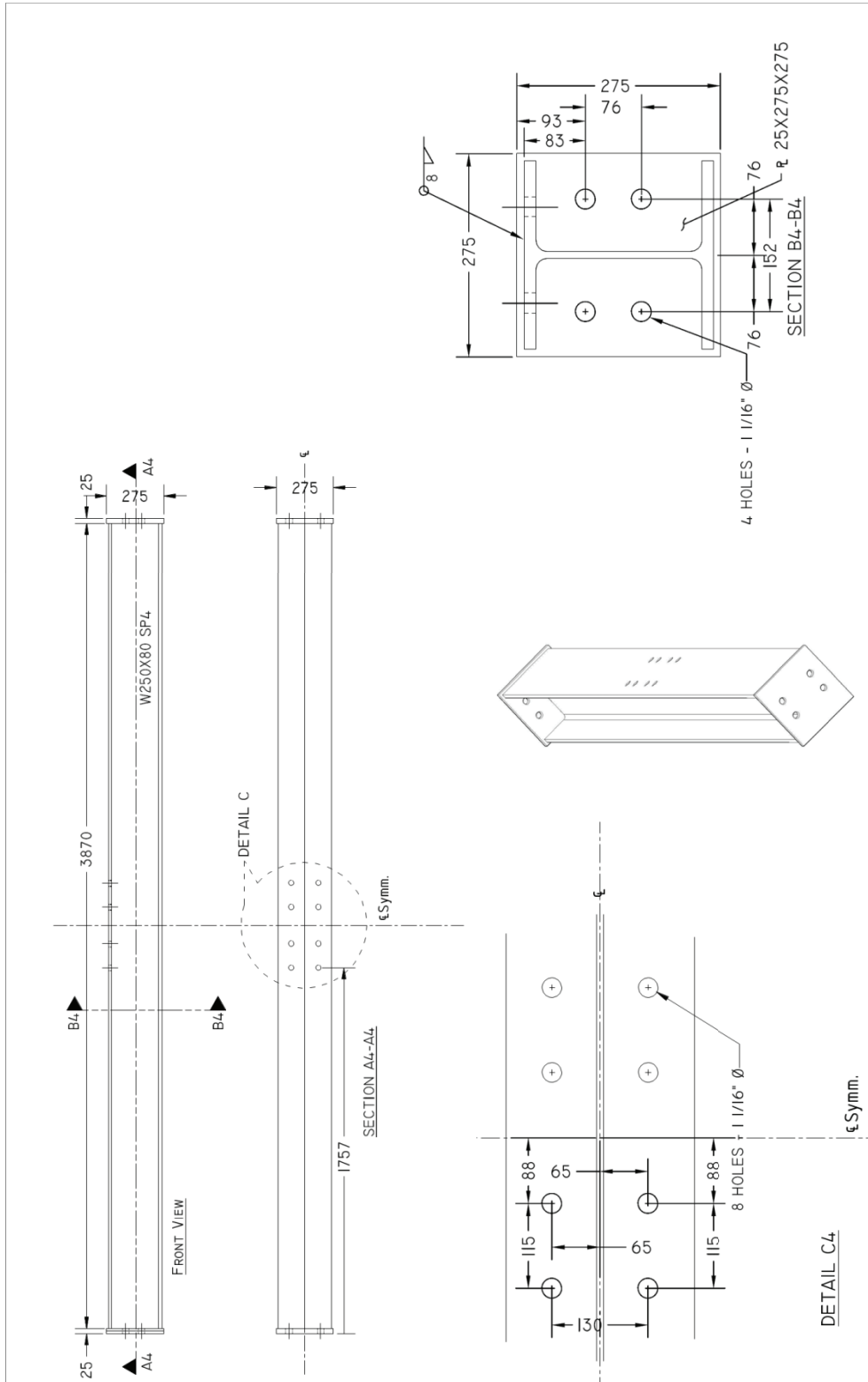


Figure A.5. Drawing SP4

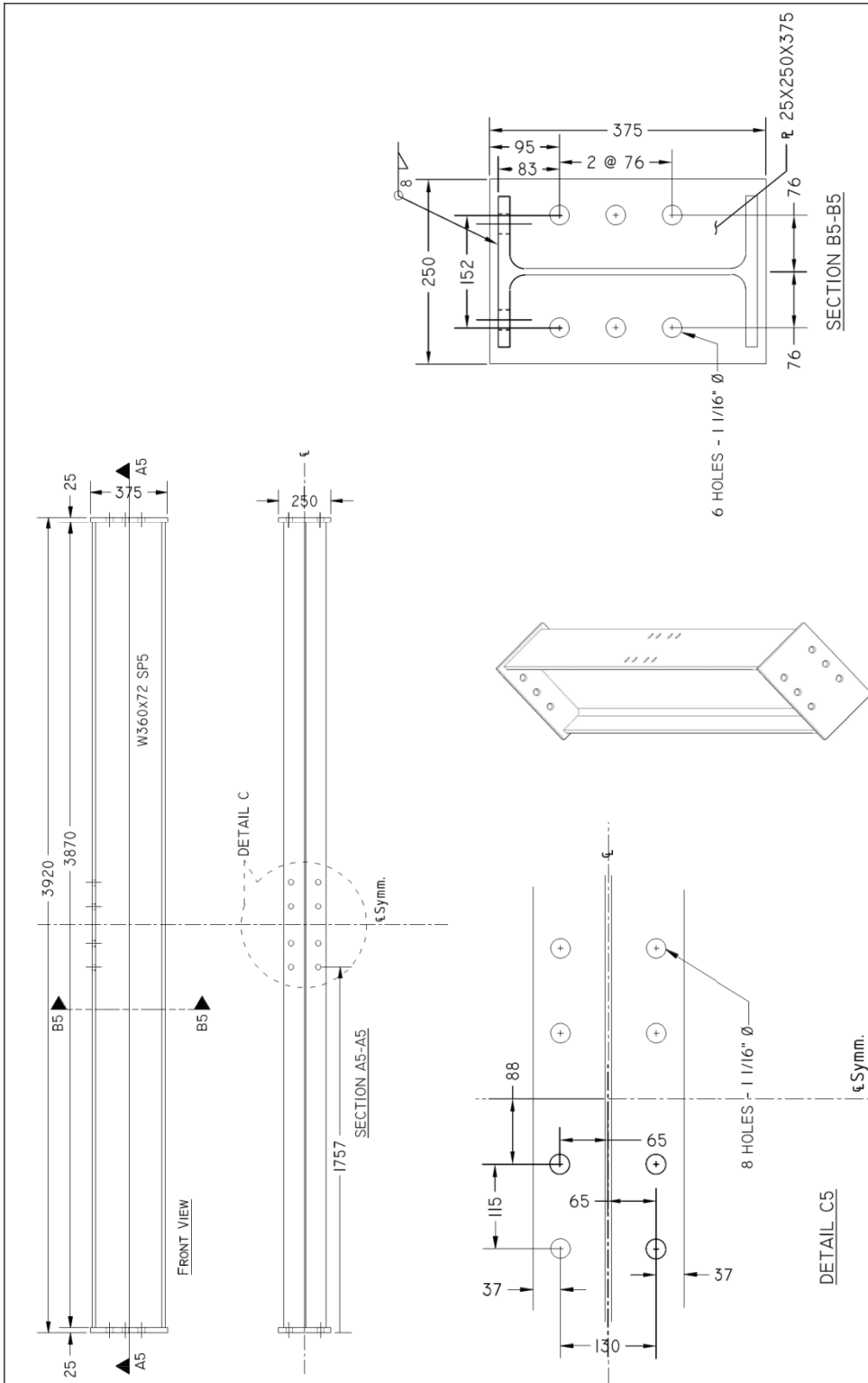


Figure A.6. Drawing SP5

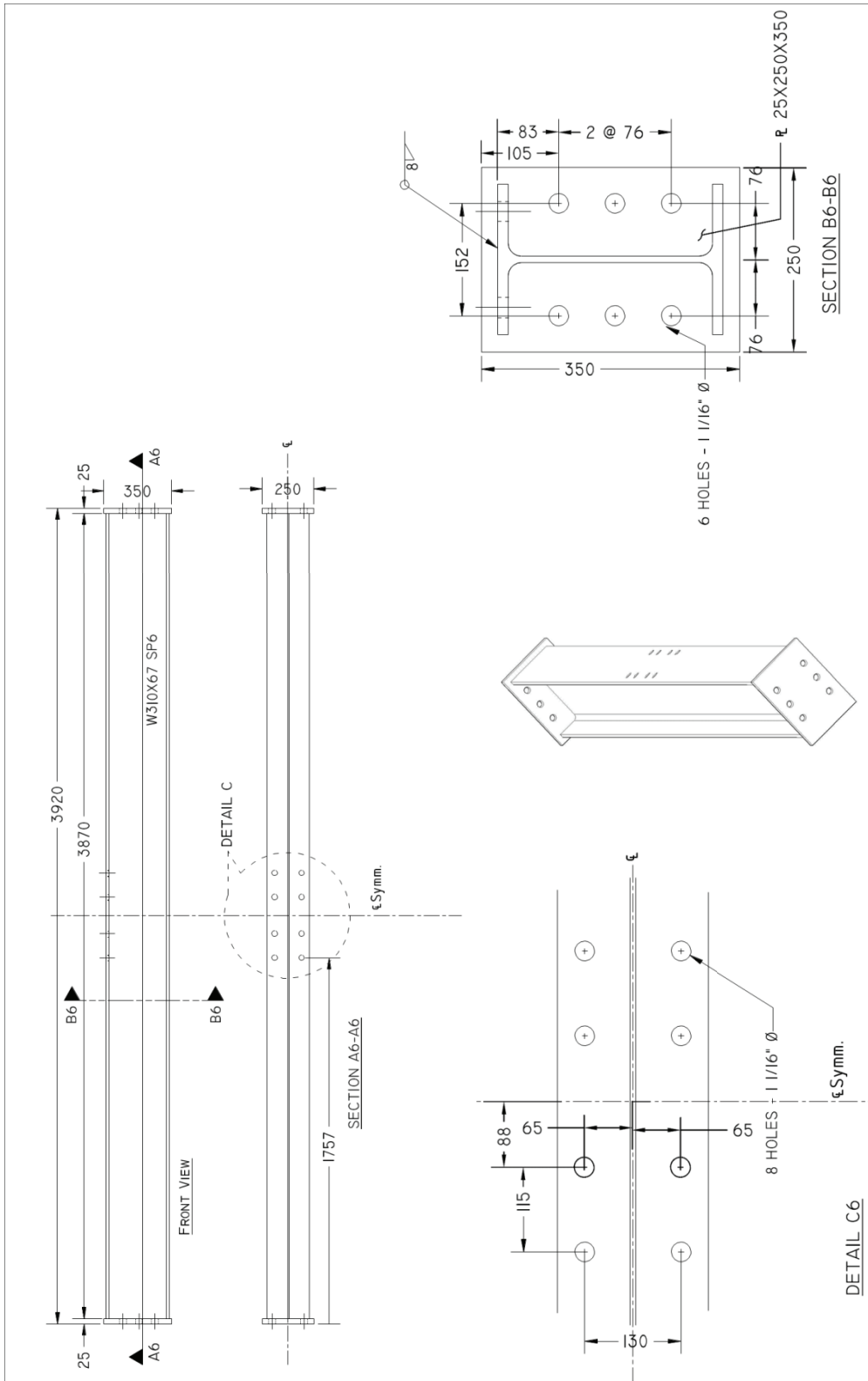


Figure A.7. Drawing SP6

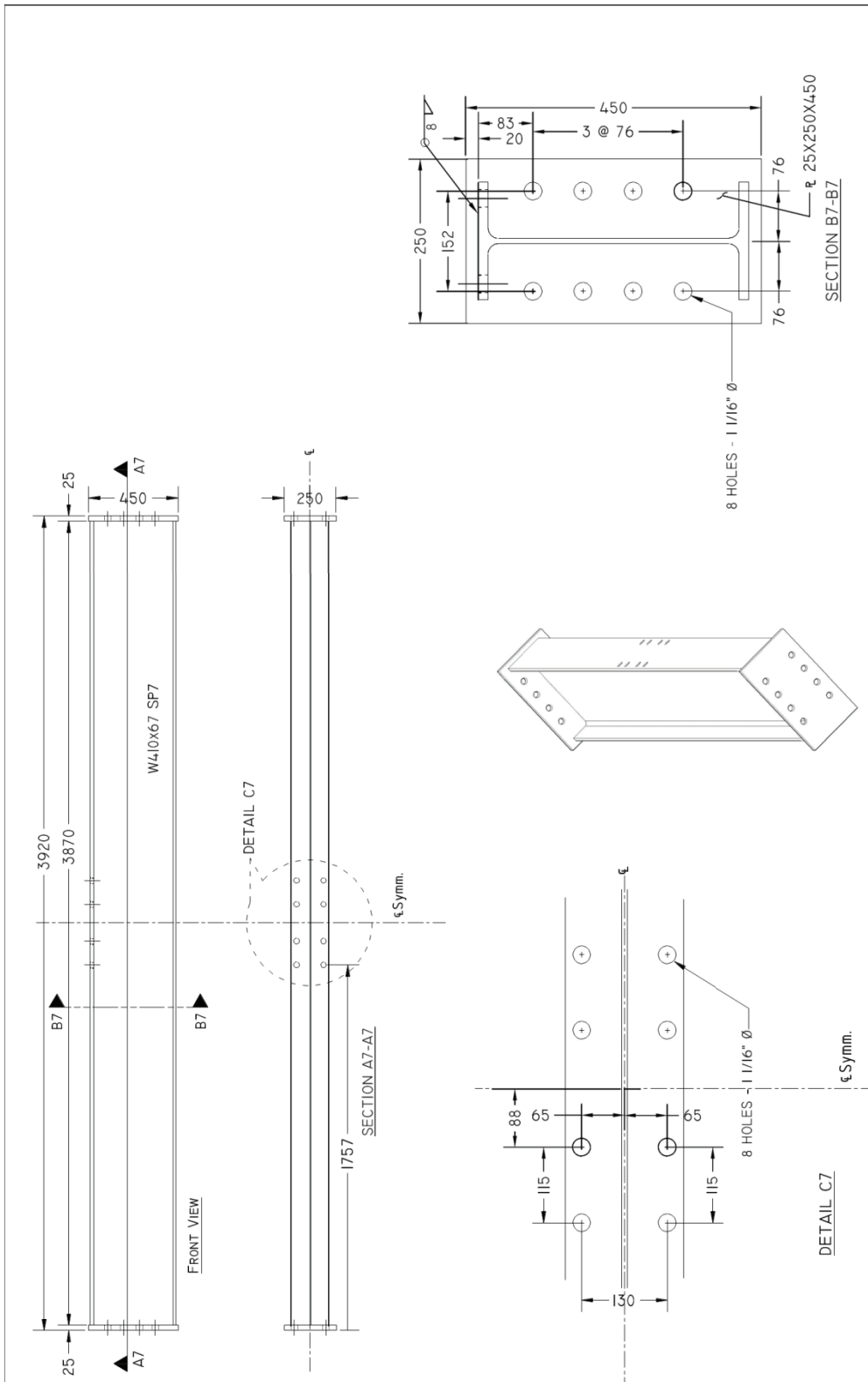


Figure A.8. Drawing SP7

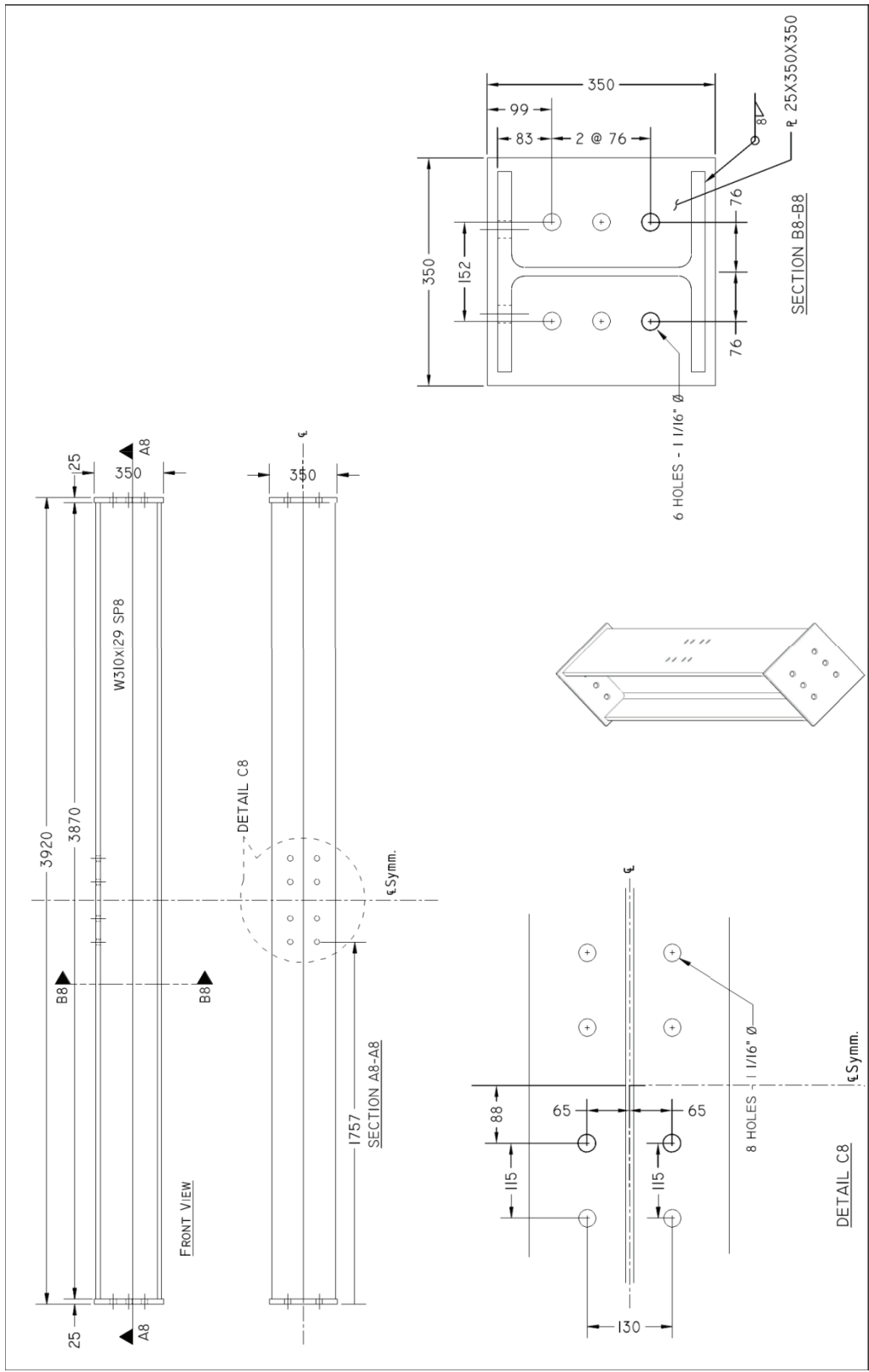


Figure A.9. Drawing SP8

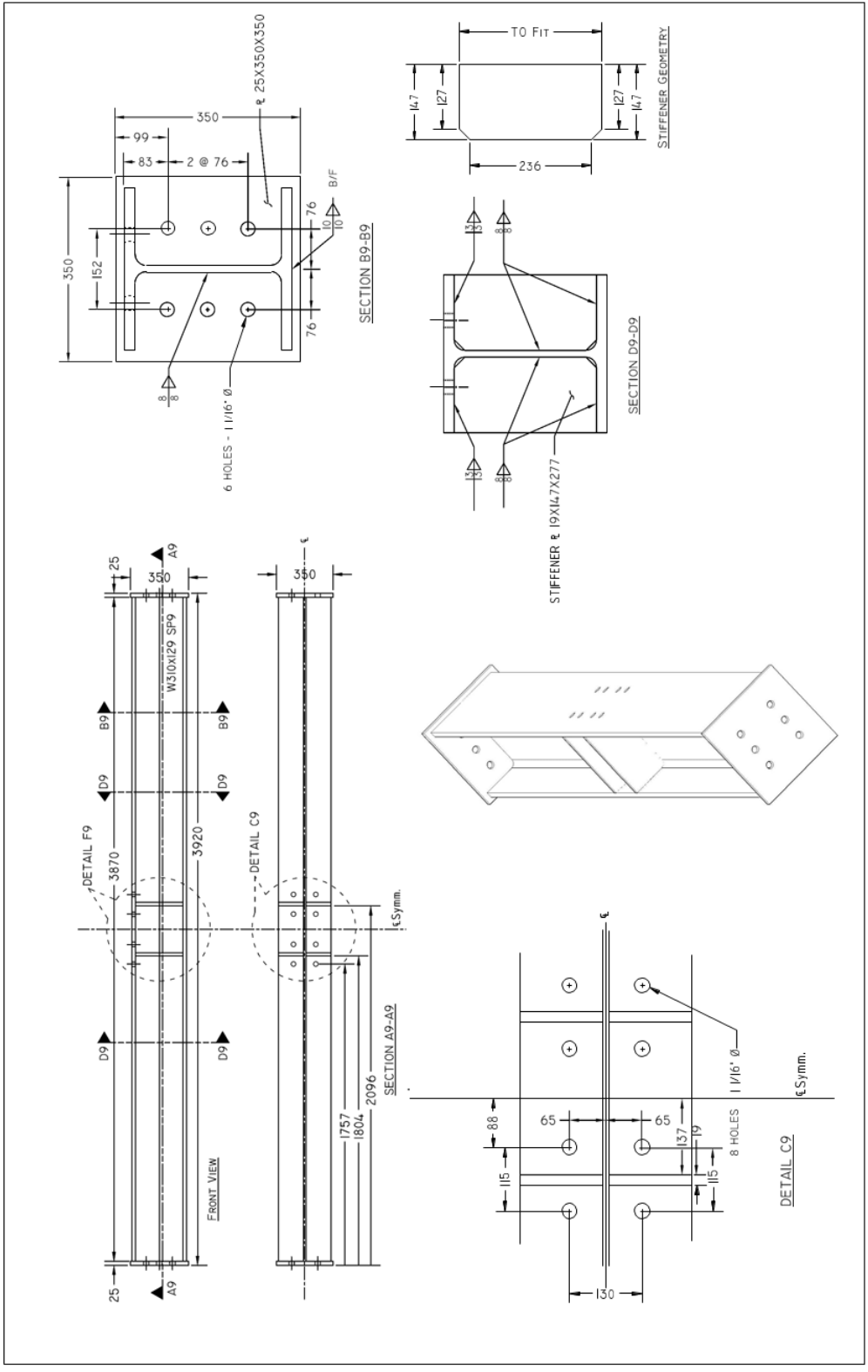


Figure A.10. Drawing SP9

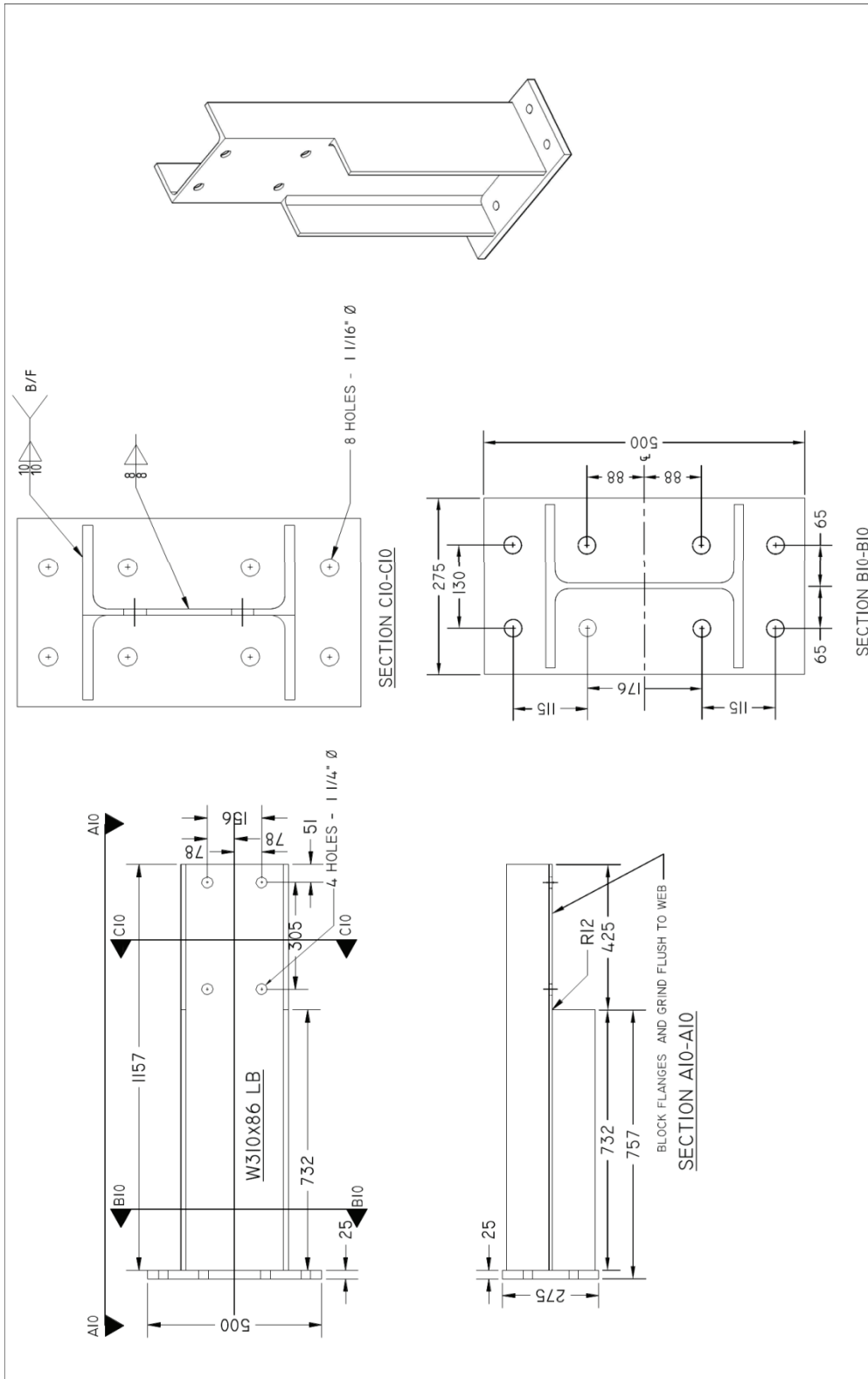
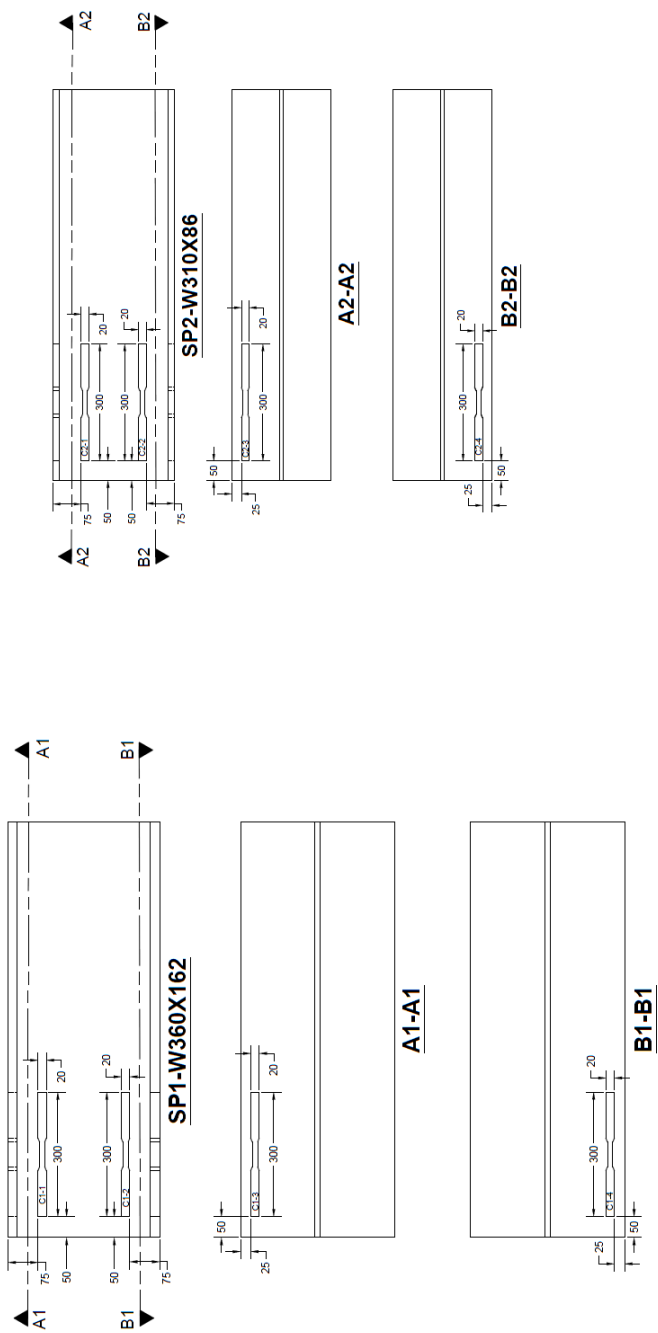


Figure A.11. Drawing load transfer beam

**Appendix B**  
**Coupon Cut-Out Drawings, Measured Dimensions and Ancillary Test**  
**Results**



**Figure B.1. Coupon drawing SP1 and SP2**

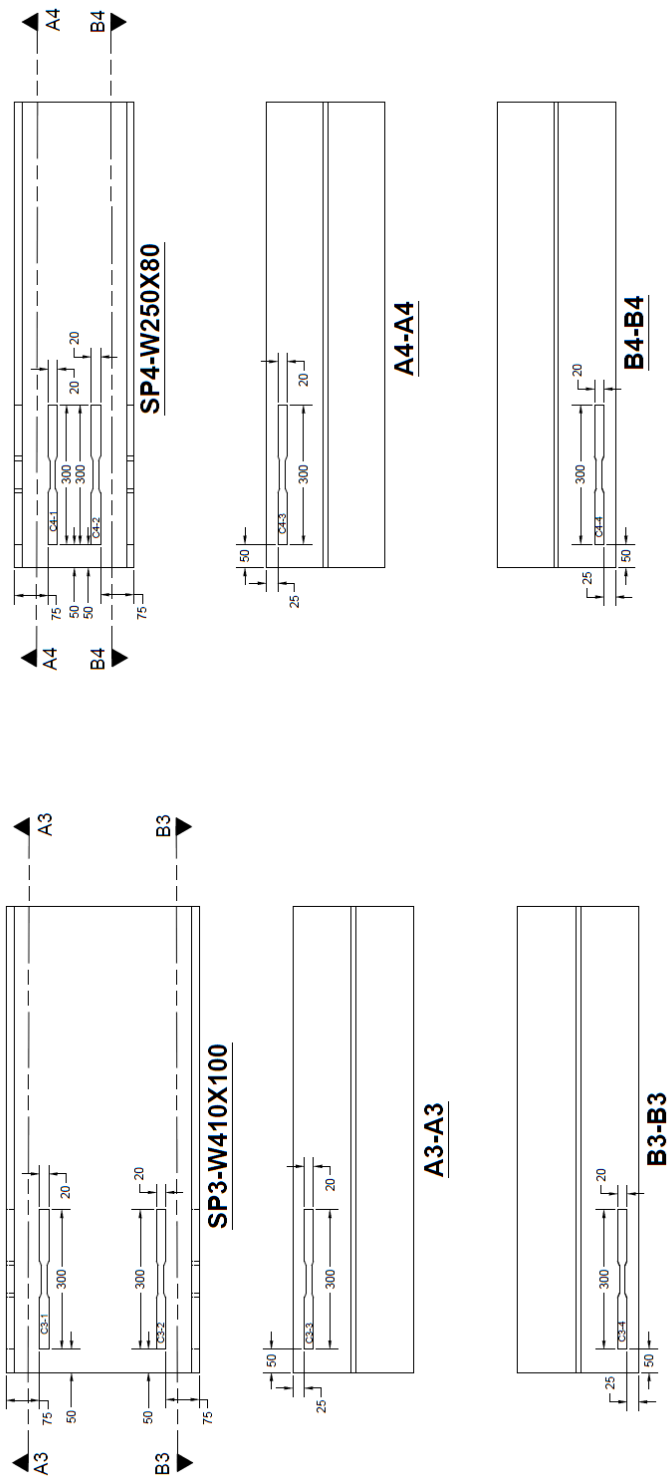


Figure B.2. Coupon drawing SP3 and SP4

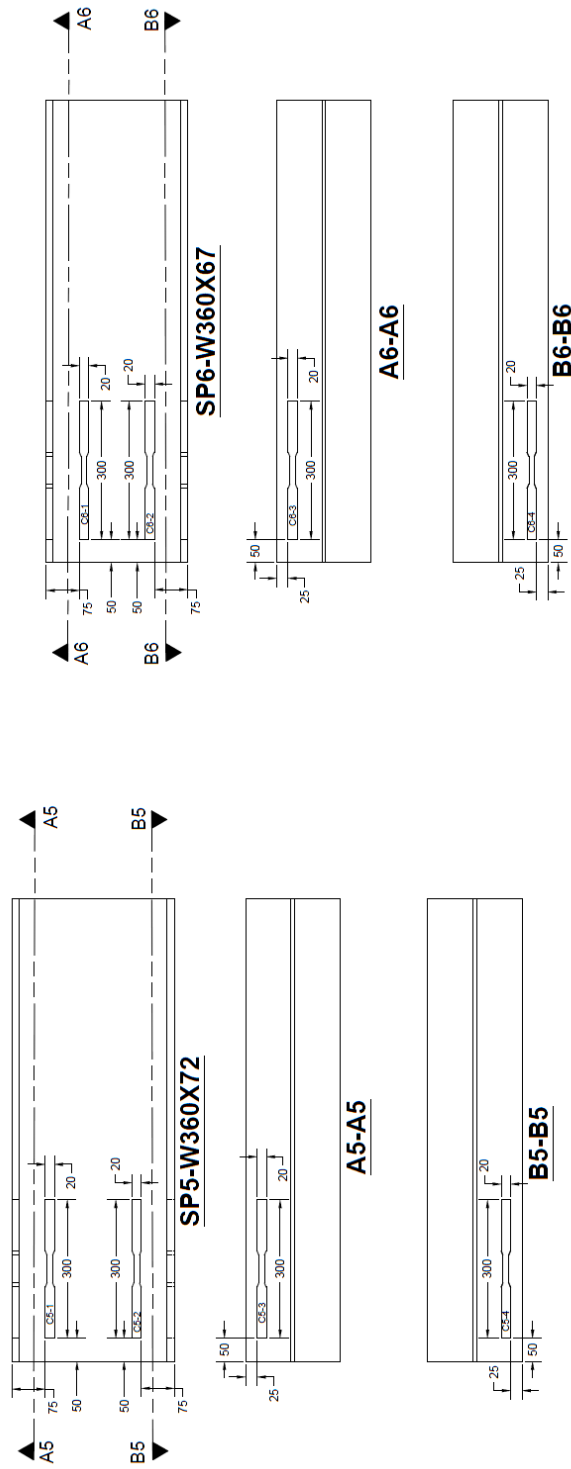


Figure B.3. Coupon drawing SP5 and SP6

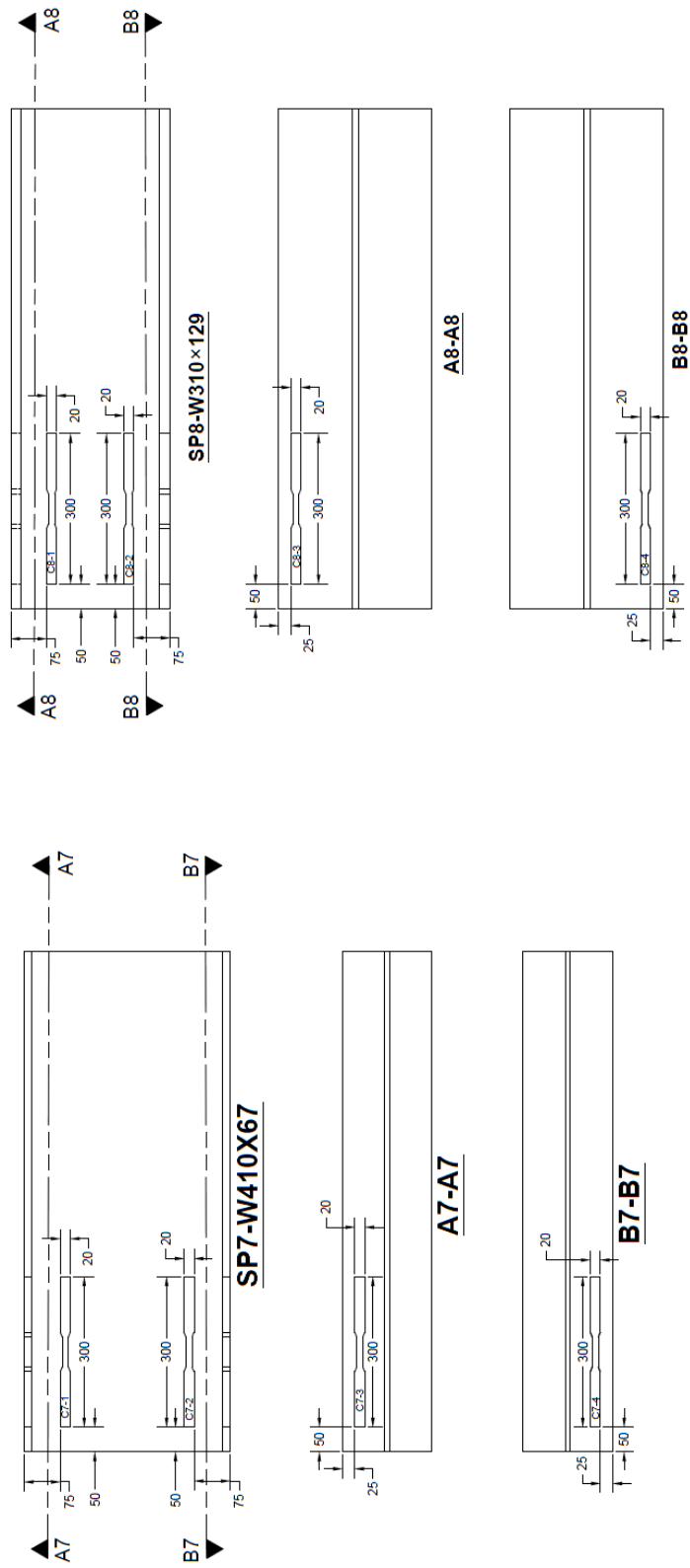
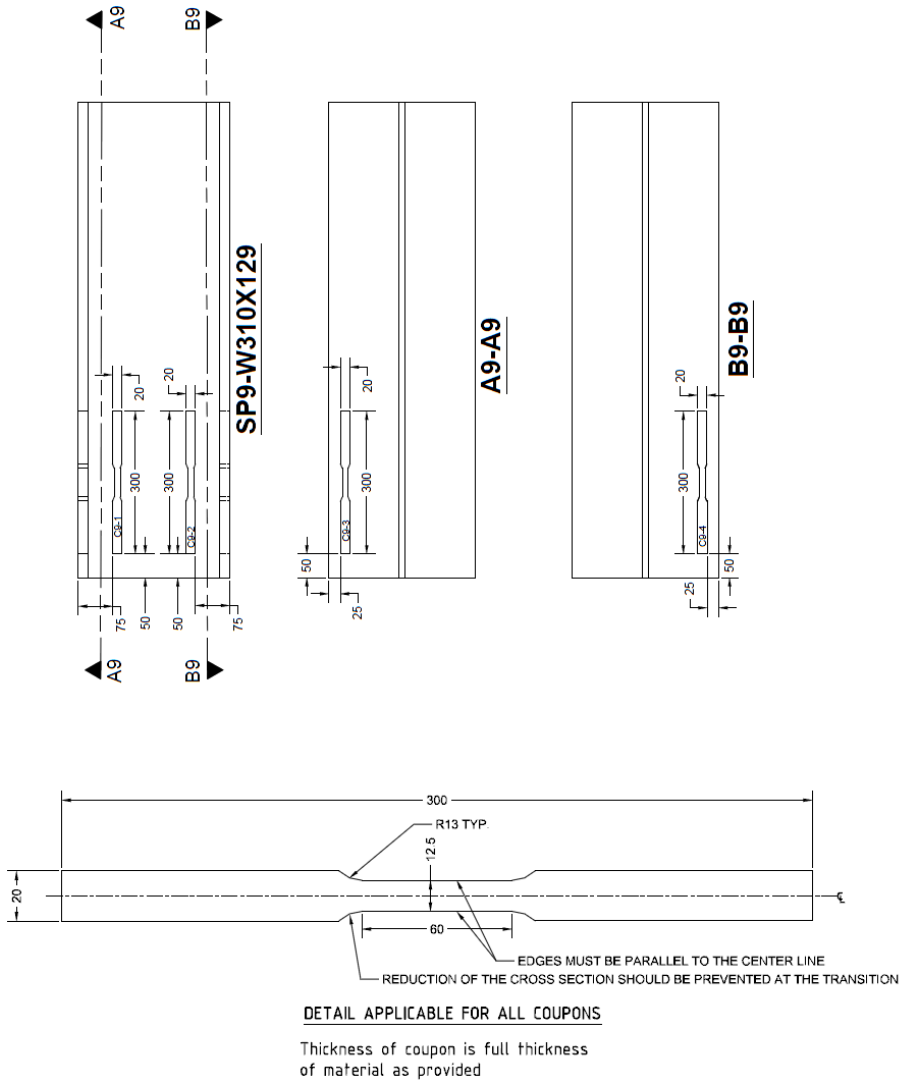


Figure B.4. Coupon drawing SP7 and SP8



**Figure B.5. Coupon drawing SP9 and detailed coupon**

**Table B.1. Coupon measured dimensions**

<b>Designation</b>	<b>Thickness (mm)</b>	<b>Width (mm)</b>	<b>Area (mm<sup>2</sup>)</b>
C1-1	13.85	12.90	178.67
C1-2	13.85	12.80	177.28
C1-3	19.80	12.45	246.51
C1-4	20.90	12.50	261.25
C2-1	9.60	12.80	122.88
C2-2	9.53	13.00	123.89
C2-3	15.70	12.50	196.25
C2-4	16.00	12.40	198.40
C3-1	10.90	12.75	138.98
C3-2	10.90	12.45	135.71
C3-3	16.20	12.60	204.12
C3-4	16.88	12.75	215.22
C4-1	10.10	12.50	126.25
C4-2	10.25	12.60	129.15
C4-3	14.95	12.50	186.88
C4-4	15.60	12.40	193.44
C5-1	8.60	12.60	108.36
C5-2	8.75	12.50	109.38
C5-3	14.00	12.50	175.00
C5-4	14.25	12.50	178.13
C6-1	8.55	12.50	106.88
C6-2	8.52	12.55	106.93
C6-3	14.60	12.50	182.50
C6-4	14.80	12.40	183.52
C7-1	8.50	12.70	107.95
C7-2	8.70	12.75	110.93
C7-3	14.30	12.80	183.04
C7-4	14.25	12.55	178.84
C8-1	13.85	12.80	177.28
C8-2	14.10	12.90	181.89
C8-3	18.40	12.80	235.52
C8-4	19.25	12.80	246.40
C9-1	14.05	12.80	179.84
C9-2	13.95	12.90	179.96
C9-3	19.60	13.00	254.80
C9-4	19.56	12.80	250.37

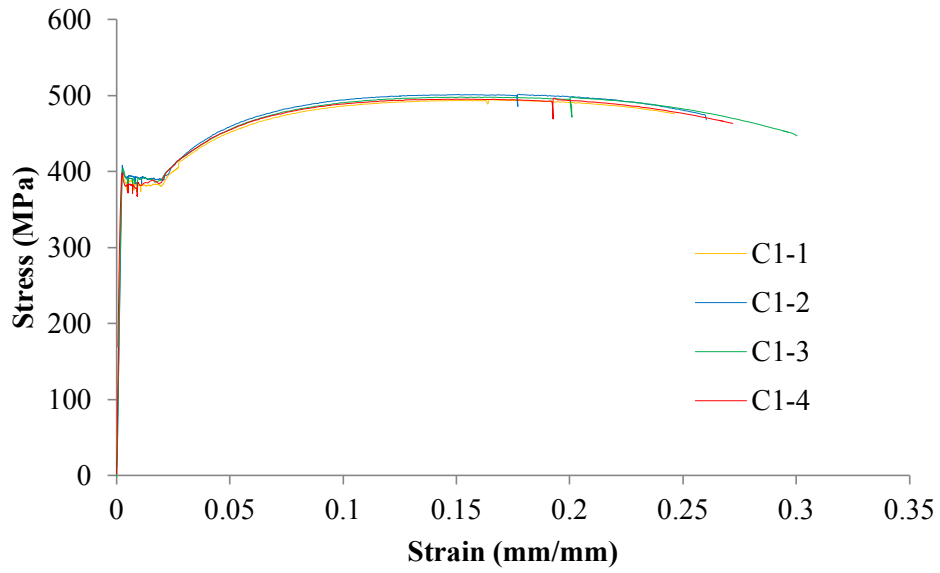


**Figure B.6. Stress-strain curves for SP1 coupons**

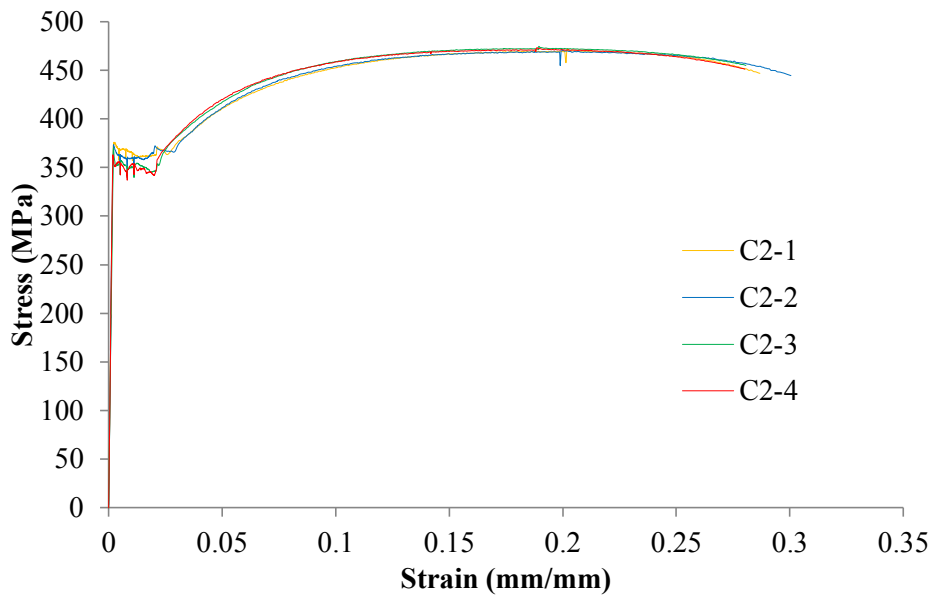


**Figure B.7. Stress-strain curves for SP2 coupons**

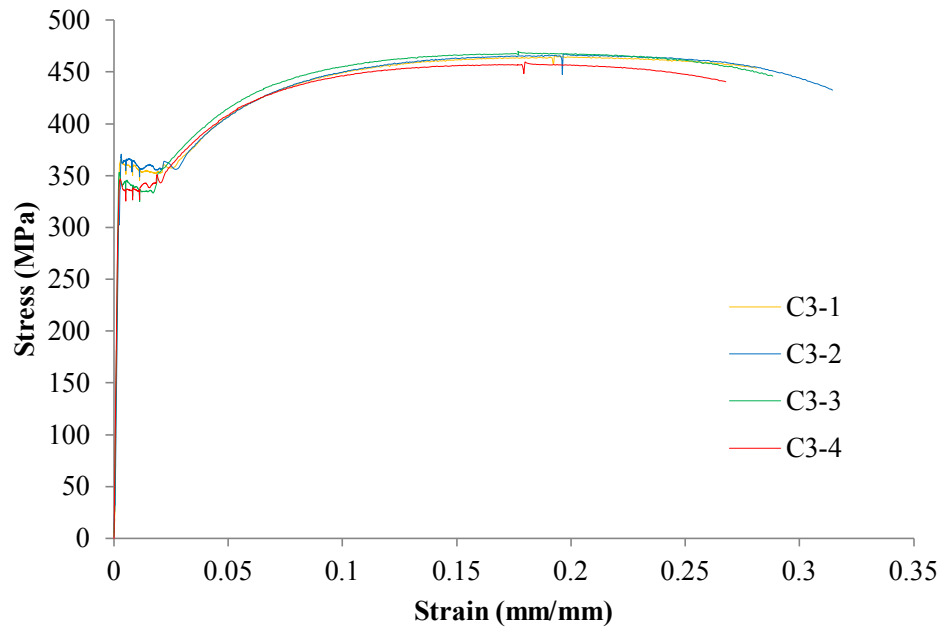


**Figure B.8. Stress-strain curves for SP3 coupons**

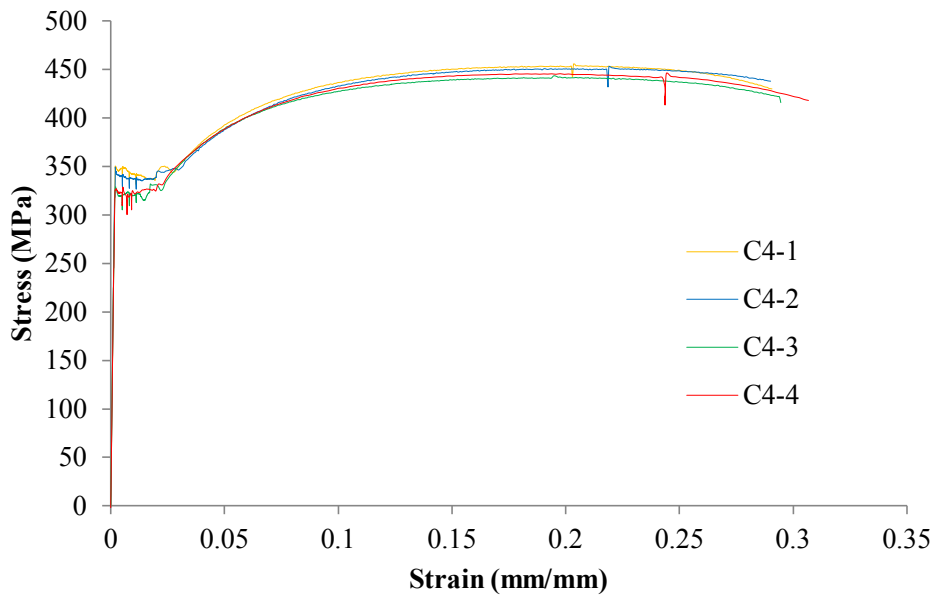


**Figure B.9. Stress-strain curves for SP4 coupons**

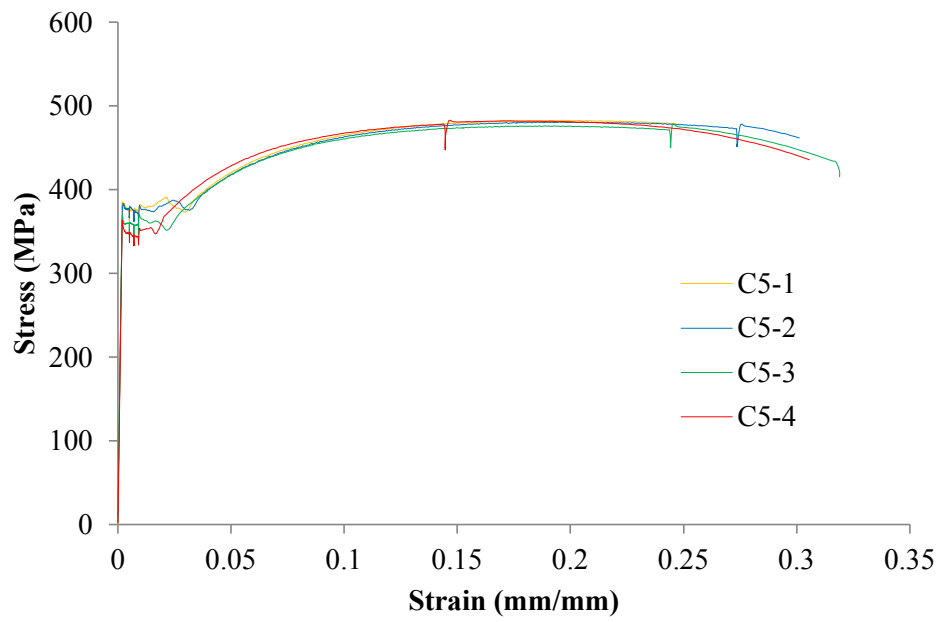


**Figure B.10. Stress-strain curves for SP5 coupons**

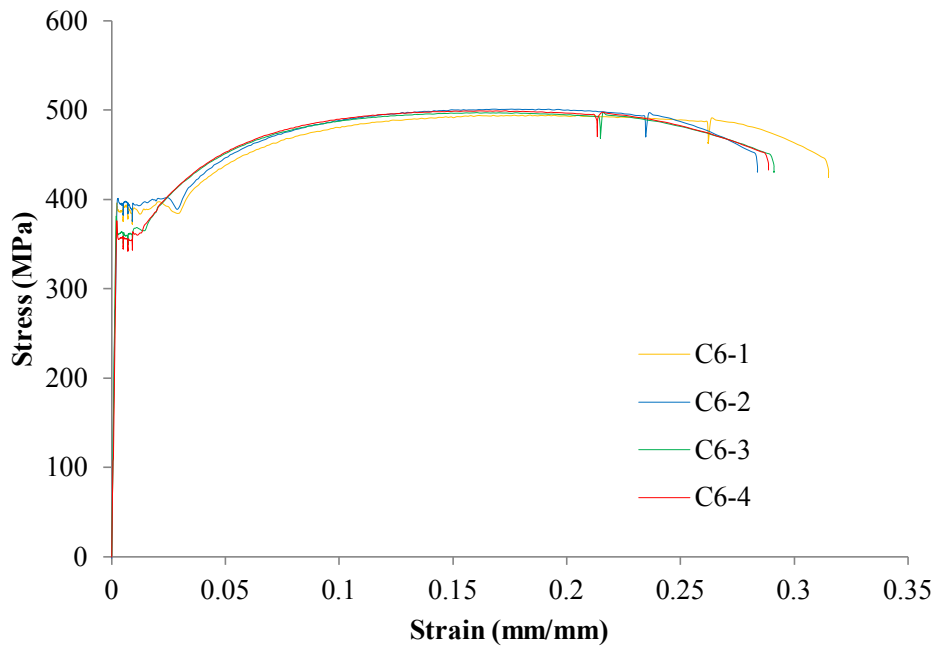


**Figure B.11. Stress-strain curves for SP6 coupons**

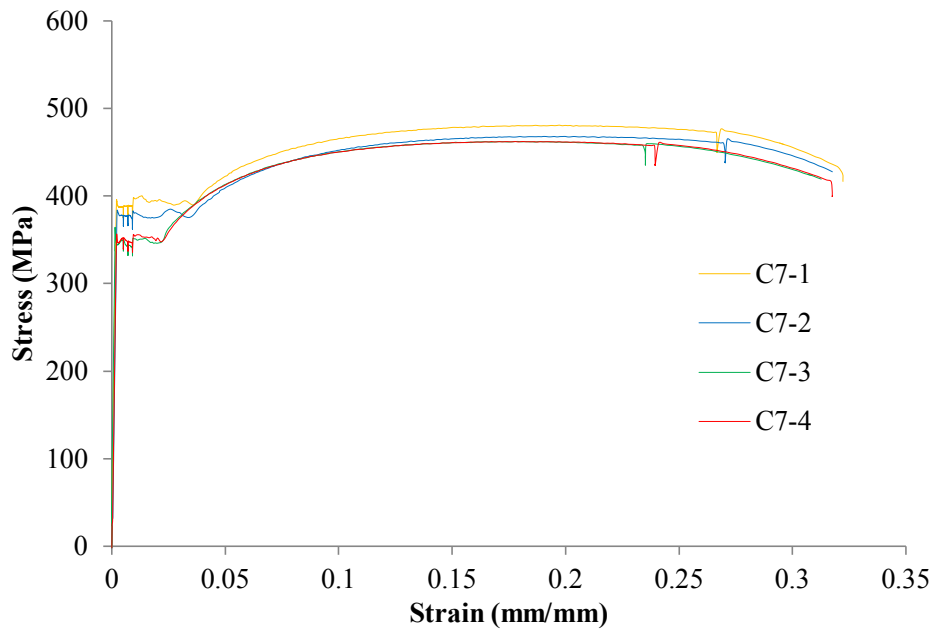


Figure B.12. Stress-strain curves for SP7 coupons

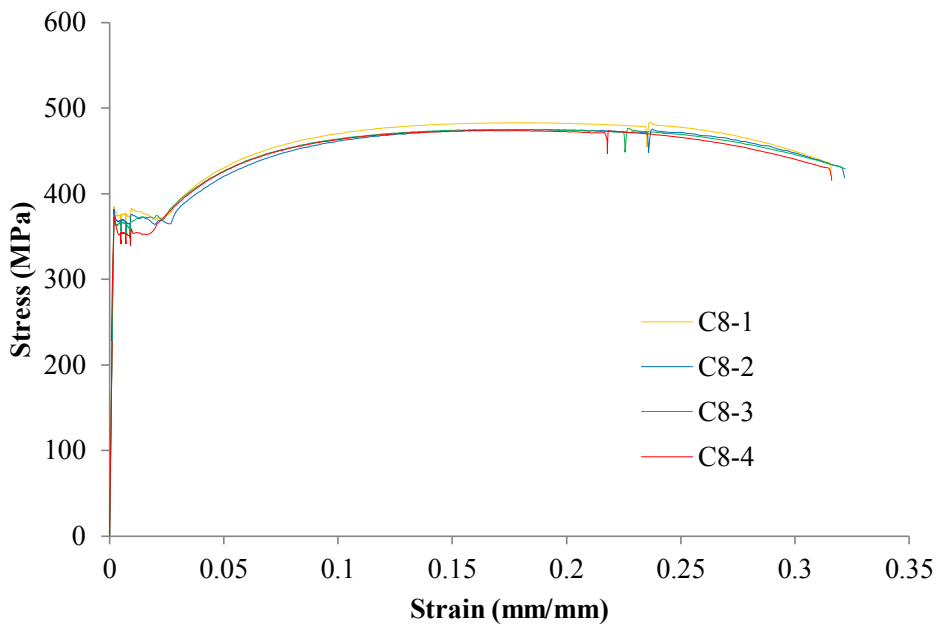
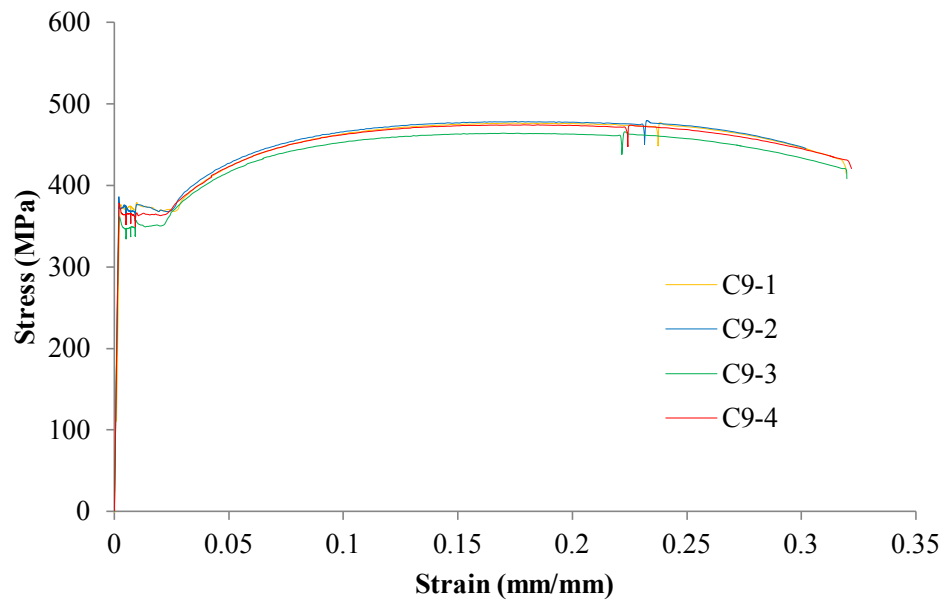


Figure B.13. Stress-strain curves for SP8 coupons



**Figure B.14. Stress-strain curves for SP9 coupons**